Master's Thesis
September 2008 - August 2009
09/05

Pharmacokinetic modeling in breast cancer MRI

Author:
Geert Litjens

Supervisors:
ir. M. Heisen
dr. ir. J. Buurman

Eindhoven University of Technology
Biomedical Engineering
Biomedical Imaging and Modeling

Philips Healthcare
Clinical Informatics
Advanced Development

Thesis Committee:
ir. M. Heisen
dr. ir. J. Buurman
dr. ir. N.A.W. van Riel
prof. dr. K. Nicolay
prof. dr. ir. B.M. Ter Haar Romeny

September 10, 2009

Abstract

Breast cancer is a disease which impacts the lives of thousands of people. In the entire world over half a million people die due to breast cancer every year, mostly women. However, when breast cancer is detected in the early stages of disease five-year-survival rate approaches 100%. So, it is very important to detect breast cancer as early as possible. That is why in most of modern Western society screening programs for breast cancer have been developed. Most of these screening programs focus on x-ray mammography. However, women who have an increased risk to get breast cancer these screening programs are not adequate. These women usually develop breast cancer at a younger age and x-ray mammography for those women has a low sensitivity. For these cases, and inconclusive findings in x-ray mammography in other women, dynamic contrast enhance (DCE) MRI is used. In DCE MRI a contrast agent is used which takes advantage of the fact that tumor vasculature is leaky and sloppy, thus the contrast agent tends to accumulate in the tumor, leading to increased signal intensity in T_1-weighted images. Due to the fact that we have a time range of images it is possible to look at kinetic behavior. However, as kinetic curves have a large inter and intra patient variability and variability depending on the imaging site the analysis of these curves is not straightforward. Pharmacokinetic modeling could be an answer to those problems as it can be used to obtain lesion-specific physiological parameters.

To use pharmacokinetic modeling however we need high temporal resolution data, which is not readily available. The University of Chicago Medical Center obtained several high temporal resolution data sets for the initial part of the kinetic enhancement curve in addition to the regular low temporal clinical scans. These data sets were the basis for this research. When analyzing such data several factors play an important role. The first of these being the extraction of the signal-vs.-time curves from the data sets. In this report we used a small graphical user interface to extract the data. The low and high temporal resolution images were obtained in different orientations, which was a problem we also needed to solve.

The second step after extraction of the signal-vs.-time-curves was the conversion of the signal intensity to contrast agent concentration. In literature there were several methods that were used to accomplish this, but all were based on the use of a gradient recalled echo signal model. We first investigated the assumption that we can neglect T_{2^*} effects, which we concluded was allowed. To estimate concentration the tissue T_1 at time 0 has to been known. As we had no additional T_1 measurements, we used a reference tissue approach to estimate T_1. We investigated if the simplifications often used in this method were allowed and we concluded that it was better to use the full model. The last part of the conversion to concentration is the estimation of uncertainty in the concentration curves, which in itself contains several uncertainties. We derived an algebraic expression for these uncertainties using a Taylor expansion of concentration uncertainty. On average the uncertainty levels are around 10% of the concentration.

The third step was choosing a pharmacokinetic model, we inspected a total of four models, the standard and extended Tofts models, the shutter speed model and the Brix model. We first assessed the ability of each model to find correct minima using a forward-backward simulation approach. We then simulated data that has the same temporal and uncertainty characteristics as real clinical data and used the same forward-backward approach to estimate model performance. We concluded that for data with those specific characteristics only the standard Tofts model performed adequately. After that we started investigating the data requirements for all models and we could see that for all models except the standard Tofts model data requirements on especially temporal resolution are high. Lastly we did an investigation in the errors introduced by assuming that the underlying physiological processes are more simplistic, which is what we do when we use the standard Tofts model.

The fourth step was finding the arterial input function, which is used as an input for the pharmacokinetic model. In literature there are several methods, we discussed three: the use of a standardized input function (population averaged or mathematical), the use of a single reference tissue approach and the use of a multiple refernce tissue approach. We found that errors caused by using a population averaged input function can be quite large as deviations from the true local input functions are seen directly in the pharmacokinetic parameters. The single reference tissue

approach is another way to estimate the input function. We found that when we know the exact pharmacokinetic parameters of the reference tissue the errors are considerably lower than in the use of a standardized AIF. When pharmacokinetic parameters of the reference tissue are wrong however we can still induce large errors in parameter estimates. The third option was the use of a multiple reference tissue approach, which gave the best results. If multiple reference tissue are available within the data set this option should be used.

The last step is to put together the pieces from the previous steps and use that to analyze the clinical data. We were able to use 14 patient data sets. Although a small number, we were able to see that there seems to be a relation between malignancy and K_{trans} values. Benign tissues seemed to have lower K_{trans} values when compared to malignant tissues. Another question was if we were able to cluster different cancer types according to pharmacokinetic parameters, but we have too little data to support that claim.

Samenvatting

Borstkanker is een ziekte die impact heeft op duizenden mensen wereldwijd. Over de hele wereld sterven jaarlijks een half miljoen mensen door borstkanker, vooral vrouwen. Maar als borstkanker in de vroege stadia van de ziekte ontdekt wordt dan nadert de five-year-survival-rate 100%. Het is dus heel belangrijk om borstkanker op tijd te detecteren. Dat is de reden dat in veel Westerse landen screening programma's voor borstkanker bestaan. De meeste van die programma's focussen zich op x-ray mammografie. Echter, voor vrouwen die een hoger risico hebben om borstkanker te krijgen zijn deze programma's niet toereikend. Die vrouwen ontwikkelen vaak op jongere leeftijd borstkanker en op die leeftijd heeft x-ray mammografie een lagere sensitiviteit door dicht borstweefsel. For deze gevallen, en voor gevallen waarin mammografie geen definitieve bevinding had, wordt dynamic contrast enhanced (DCE) MRI gebruikt. In DCE MRI wordt een contrastmiddel toegediend dat gebruik maakt van het feit dat de bloedvaten in tumoren lek en slordig zijn, waardoor het contrastmiddel zich ophoopt in de tumor. Dit leidt tot een stijging van de signaal intensiteit in T_1 gewogen beelden. Door het feit dat we een tijdsspanne van plaatjes hebben is het mogelijk om naar kinetisch gedrag te kijken. Echter, kinetische curves hebben een grote inter en intra patiënt variabiliteit en ook nog variabiliteit die bepaald wordt door de verschillende plaatsen waar MRI gedaan wordt waardoor het analyseren van die curves niet triviaal is. Pharmacokinetisch modelleren zou een antwoord kunnen zijn op deze problemen omdat het laesie specifieke fysiologische parameters kan afleiden.

Om pharmacokinetisch te kunnen modelleren hebben we echter wel data nodig met een hoge temporele resolutie, die niet algemeen beschikbaar is. De University of Chicago Medical Center had door onderzoek diverse hoog temporele resolutie datasets van het initiële gedeelte van de kinetische curve verkregen, in aanvulling op de reguliere laag temporele resolutie scans. Deze datasets waren de basis voor dit onderzoek. Als men dat soort data analyseert spelen een aantal factoren een belangrijke rol. De eerste van deze is het extraheren van de signaal-tijd curves uit de datasets. In dit verslag hebben we een kleine gebruikersinterface gemaakt voor dit doel. De lage en hoge temporele resolutie data was in verschillende oriëntaties genomen, wat ook een probleem was wat opgelost moest worden.

De tweede stap na het extraheren van de signaal-tijd curves was het converteren van de signaalintensiteit naar contrastmiddelconcentratie. In de literatuur waren er een aantal methoden die dit voor elkaar konden krijgen, allemaal gebaseerd op het gebruik van een gradient recalled echo signaalmodel. We hebben eerst onderzocht of de aanname dat T_{2^*} effecten verwaarloosd kunnen worden waar is, waaruit we concludeerden dat dat zo was. Om de concentratie uit te kunnen rekenen was het nodig om de weefsel T_1 op tijdstip 0 te weten. Aangezien we geen extra T_1 metingen ter beschikking hadden was het nodig om een andere methode te gebruiken, wij hebben gekozen voor de referentie weefsel method. We hebben onderzocht of versimpelingen van die methode acceptabel waren en wij hebben geconcludeerd dat deze versimpelingen niet noodzakelijk zijn en extra fouten introduceren. Het laatste stuk van conversie naar concentratie is de afschatting van de onzekerheid in de concentratie curves, omdat deze is opgebouwd uit verschillende andere onzekerheden. We hebben een algebraïsche uitdrukking voor deze onzekerheden afgeleid door middel van een Taylor expansie. Gemiddeld lagen de onzekerheidsniveaus op ongeveer 10% van de concentratie.

De derde stap was het kiezen van een pharmacokinetisch model. We hebben in total vier modellen bekeken, de standard en extended Tofts modellen, het shutter speed model en het Brix model. We hebben eerst onderzoek gedaan naar de mogelijkheid van elk model om het correcte minima te vinden door middel van een forward-backward simulatie. Daarna hebben we data gesimuleerd met dezelfde temporele en onzekerheidskarakteristieken als de klinsche data, waarna we dezelfde forward-backward simulaties hebben gedaan om de modelprestatie af te schatten. We concludeerden dat voor dit type data alleen het standard Tofts model voldoende functioneerde. Daarna hebben we onderzocht wat de eisen aan de data zijn om ingewikkeldere modellen te mogen gebruiken. Hieruit kwam naar voren dat voor alle modellen behalve het standaard Tofts model de eisen op de data, vooral de temporele resolutie, hoog zijn. Als laatste hebben we onderzocht of de fouten die we introduceren door het versimpeld voorstellen van de fysiologische werkelijkheid

groot waren. Dit is namelijk wat je doet als je het standard Tofts model gebruikt.

De vierde stap was het vinden van een arteriële invoer functie, die de invoer vormt van het pharmacokinetisch model. In de literatuur zijn er verschillende methoden, wij hebben er drie besproken: het gebruik van een gestandaardiseerde invoer functie, het gebruik van een enkel referentie weefsel en het gebruik van meerdere referentieweefsels. We vonden dat de fouten die geïntroduceerd werden door het gebruik van een gestandaardiseerde invoer functie vrij groot kunnen zijn omdat de deviatie van zo'n invoer functie van de ware locale invoer functie vrij groot kan zijn en dat zie je direct terug in je pharmacokinetische parameters. Het gebruik van een enkel referentieweefsel geeft veel kleinere fouten, aangenomen dat je de pharmacokinetische parameters van het referentieweefsel weet. Als je deze niet weet is het nog steeds mogelijk om grote fouten te introduceren. De derde methode was het gebruik van meerdere referentieweefsels, deze methode gaf de beste resultaten. Als er meerdere referentieweefsel beschikbaar zijn is dit de methode om te kiezen.

De laatste stap die we gedaan hebben in dit verslag is het bij elkaar pakken van wat we geleerd hebben in de vorige stappen en dat gebruiken om de klinische data te analyseren. We hebben uiteindelijk 14 datasets kunnen analyseren, hoewel dat maar een klein aantal is hebben we toch kunnen zien dat er een relatie lijkt te bestaan tussen K_{trans} en de mate van maligniteit. Benigne weefsel lijken een lagere K_{trans} waarde te hebben dan maligne weefsel. Een tweede vraag was of het mogelijk is om verschillende kankertypes te clusteren aan de hand van hun parameters maar we hebben te weinig data om hier een goede uitspraak over te doen.

Contents

Chapter 1

Introduction

1.1 Cancer and its toll on society

Cancer is one of the leading causes of death in the world, approximately 7.9 million people die of cancer every year, which is 13% of all deaths[55]. Lung cancer accounts for most cancer deaths, with breast cancer taking fifth place (second considering only women) with around 548000 deaths each year[55]. In the Netherlands, cancer accounted for approximately 40000 deaths in 2007, which is one third of all deaths. Among women, breast cancer is by far the most prominent cancer and has the second highest death count, with 12000 patients and 3200 deaths each year, surpassed only by lung cancer, posing one of the most serious health problems for women[21]. Breast cancer incidence has risen substantially in the last two decades. The increase can be partly explained by the fact that the population, especially of Western countries, show a steady increase in average age. As the risk of cancer increases with age, the incidence of cancer increases. Other reasons could be changing environmental or cultural aspects. However, for breast cancer especially, the introduction of screening programs and increased public awareness due to self-examination campaigns also plays an enormous role in the increase of the incidence rate, but also in the decline of the death rate of breast cancer[1].

In part this decrease could be attributed to increased knowledge and better treatment of cancer. However, in women that do not participate in screening programs the death rate has not declined, pointing to a large contribution of early detection in the decrease. Indeed, if the tumor is still confined to the breast at the time of detection and has not spread to auxiliary lymph nodes, five year survival rate approaches 100%[33]. This shows that screening programs are of tremendous importance, the better and more effective the screening program, the better the outlook for the patients.

1.2 Breast anatomy and tumor pathology

Before delving into screening of the breast, it is useful to know something about breast anatomy and tumor pathology, especially what parts of the breast are most prone to cancerous growths.

In figure 1.1 a schematic overview of the breast is given. The areas most prone to cancer are the ducts and the lobules, numbers [6] and [3] respectively, with ductal cancer being by far the most prominent one as can be seen in table 1.1. The pre-cancer stage is ductal carcinoma in situ (DCIS) or lobular carcinoma in situe (LCIS), which is what we would like to detect, because at this stage the five year survival rate is almost 100%. However, most DCIS and LCIS are very difficult to detect, due to the fact that in these stages the cancer often is relatively small and still confined to the duct or lobule it originally developed in. Some DCIS and LCIS never even develop to a real cancer. For each imaging modality there are several features which are a measure for the risk of malignancy. These features are standardized and a short explanation can be found in

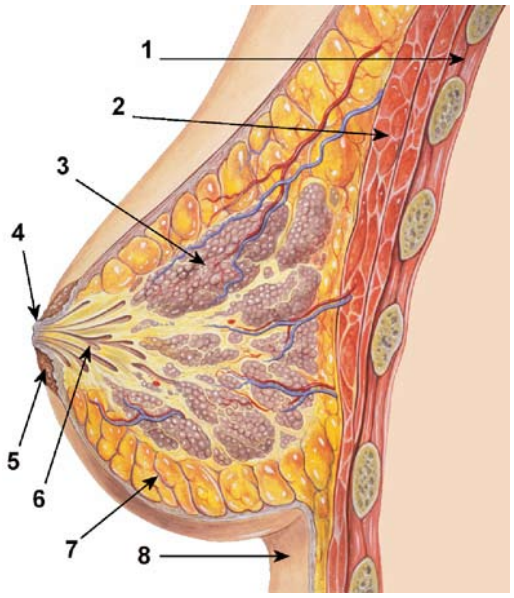

(a) Breast Anatomy (Image by Patrick Lynch, Yale University Center for Advanced Instructional Media)

Number	Description
1	Chest Wall
2	Pectoralis Muscles
3	Lobules
4	Nipple Surface
5	Areola
6	Lactiferous duct
7	Fatty Tissue
8	Skin

(b) Breast Anatomy (Labels)

Figure 1.1: Breast Anatomy

Histologic type	Incidence [%]
Invasive Ductal Carcinoma	50-80
Invasive Lobular Carcinoma	5-15
Medullary Carcinoma	1-7
Mucinous Carcinoma	2-2.2
Comedo Carcinoma	1.4
Paget's Disease	1.1
Papillary Carcinoma	0.9
Tubular Carcinoma	0.7-2.0

Table 1.1: Breast Cancer Types according to incidence[49]

section 1.4.2. The detection of cancer using different imaging modalities is explained in section 1.3.

1.3 Screening

1.3.1 X-Ray based screening

The general population screening program for breast cancer is normally based on X-Ray mammography, using low-dosage radiation to generate an image of the breast. In case of breast cancer, there usually are light speckles in the images, which can indicate micro-calcifications.

Micro-calcifications are usually formed in areas with a higher than usual cellular activity. The pattern in which the micro-calcification are spread and the density and shape of the micro-calcifications might be cause for concern. If the radiologist thinks that there might be a tumor present, the patient usually is referred for a breast biopsy or additional imaging for further diagnosis.

The screening programs in the Netherlands are specifically designed for women of middle-

age and older. In the Netherlands the breast cancer screening program consists of a biannual mammography for all women between 50 and 75. The reason for this is that women become far more likely to develop breast cancer after menopause due to changes in the hormonal activity in their body. For younger women, on average, the risk of developing cancer does not outweigh the risk of the radiation dosage in the biannual screening. Also it is shown in several large studies that there is no positive effect on the five year survival rate of younger women [36]. This has roughly two reasons, the first being that there are very few women who develop cancer at such a young age, thus this has, statistically, very little effect. Secondly, for younger women mammography might not be the ideal screening methodology because younger women have more dense breast tissue, making the 'reading' of the mammogram much more difficult, increasing the risk of a tumor being overseen or even completely invisible on the mammogram, even after retrospective analysis.

Unluckily, women that develop breast cancer at a young age usually have some sort of genetic predisposition or are more prone to cancer because of other reasons, such as environmental factors. These women are usually categorized as the high risk population.

Cancer in these patients is usually a lot more aggressive. For these types of tumors it is even more important to detect them as early as possible because they could reach a metastatic state rather quickly, also making the regular biannual screening not frequent enough. It is thus essential to find a way to screen women with a high risk of developing cancer, trying to circumvent the problems that arise with X-Ray mammography. A candidate for this would be screening with MRI.

1.3.2 MRI based screening: advantages and disadvantages compared to X-Ray mammography

As mentioned before, sensitivity of X-Ray based screening declines when used in younger women because of the difference in composition of the breast tissue. In these situations it might be useful to choose another imaging modality. In several studies it has been shown that MRI has a higher sensitivity than mammography [20], published sensitivity levels range between 89-100% over all ages compared to 85% in women over 50 and 62%-76% for women between 40 and 50 in mammography [53]. This also indicates that MRI is a good candidate for re-evaluation of inconclusive findings in mammography or ultrasound.

Regarding the specificity of MRI, it is often believed that this is rather low [20]. This is not the case, as has been proven by several recent studies. The specificity of MRI is at the same level as the specificity of mammography [20] (82% - 96%).

Then why is MRI not the first choice for breast cancer screening? This has several reasons. Firstly, MRI produces a stack of images, which is an advantage in that it allows more precision in locating the tumor, but is also a disadvantage because it requires much more time for the radiologist to analyse the images. As there are already too few radiologist who have enough expertise to analyse MRI images, this causes a bottleneck. Secondly, MRI is a very expensive modality and scan time is precious, a complete MRI scan for breast cancer takes around half an hour. These disadvantages are not so easily overcome and make mammography a better first line screening modality. It is of course apparent that when in doubt or in screening high-risk women, MRI should be the modality of choice.

1.4 Use of MRI in breast cancer imaging

1.4.1 MRI: the use of contrast agent

When a cancer starts growing it starts needing more and more oxygen and nutrients to facilitate its own growth. When the supply of oxygen is inadequate the cancer cells become hypoxic, leading to the release of angiogenic factors (VEGF, Vessel Endothelial Growth Factor, is the best known) to encourage blood vessel growth toward the tumor. These vessels are created rapidly and the structure and the quality of these vessels is rather chaotic and sloppy, most likely because of

the imbalance between several growth and inhibiting factors, leaving no time to create a decent extracellular matrix and basal membrane, as opposed to regularized vascular sprouting in normal body growth and healing. This leads to large holes in the endothelial lining of the vessels. Needless to say that these vessels are incredibly permeable and leaky. However, this is to our advantage as it is this specific tumor property that is used in MRI imaging.

In regular MRI, three types of images are usually made: proton density, T_1-weighted and T_2-weighted. For more information regarding the basics of MRI imaging, the reader is referred to an online book by Hornak[13]. In DCE (dynamic contrast enhanced) breast MRI, T1-weighted images are usually used because of the use of a contrast agent, in which Gd-DTPA (gadolinium diethylenetriamine pentaacetic acid) is the most well known agent.

Gd-DTPA is used because it has a low molecular weight, enabling it to leave the blood stream and enter the extracellular space. This means that in regions with high permeability or in regions that have a large vessel density Gd-DTPA accumulates in a higher concentration than in other tissues. If there is a high concentration of Gd-DTPA in a certain region this can be seen as positive contrast in an T1-weighted MR image. In clinical practice images are acquired before injection of contrast agent and after injection of contrast agent, then these images are subtracted and the resultant image shows only enhancing regions. And example of such images is shown in figure 1.2.

It is common practice to take multiple images separated by approximately 1-2 minutes[28], the diagnostics can then not only be based on morphological features, but also on the enhancement-vs.-time-curves. The features diagnosis is based on will be discussed more thoroughly in the next subsection.

1.4.2 Morphology and kinetics in MRI time series

Lesion classification in breast MR is done using two different attributes of an enhancing region (morphology and kinetics). These attributes are assessed according to the BIRADS-standard (Breast Imaging-Reporting And Data System), which is mostly based on morphology. There are three base categories in which findings are divided: focus/foci, masslike and non-masslike enhancement. Foci are findings which are smaller than 5 millimeter and not otherwise characterizable. Masses are 3D lesions that occupy a space in the breast and non-masslike enhancements are enhancement patterns that are more cloudlike and do not correspond to a specific space. Masses are further differentiated by shape (round, oval), margins (smooth, irregular), enhancement (regular, irregular) and distribution.

After morphologic assessment, the enhancement-vs-time-curve is inspected. Malignant tumors mostly have very specific enhancement pattern. In clinical practice, the curves are usually categorized by three time points, using the Three-Time-Point method[19], seen in figure 1.3. Rapid enhancement and wash-out are correlated with malignancy, while slow to moderate initial enhancement together with a enhancement plateau or a steady/flattenend late enhancement are correlated with benign findings. This very basic approach has become normal practice because of timing limitations in older MRI scanners. It used to be impossible to acquire images with high spatial and temporal resolution. However, with modern equipment it is possible to increase temporal resolution and keep high enough spatial resolution while keeping scan time equal, although in clinical practice most of these benefits are still directed to increasing spatial resolution, reducing noise or acquiring extra images. This opens up several possibilities, both in reduction of problems with breast MRI and adding more diagnostic potential to the time curves.

1.4.3 Problems in MR imaging of breast cancer

When trying to interpret the time curves, several problems can be encountered, most of them originating from the fact that tissue properties in MR images have a ambiguous relationship with signal intensity. That means that signal intensity is not constant between MRI scanners or scanning protocols. This could pose a problem if a patient switches hospitals or if a hospital adopts a new scanning protocol or purchases a new scanner.

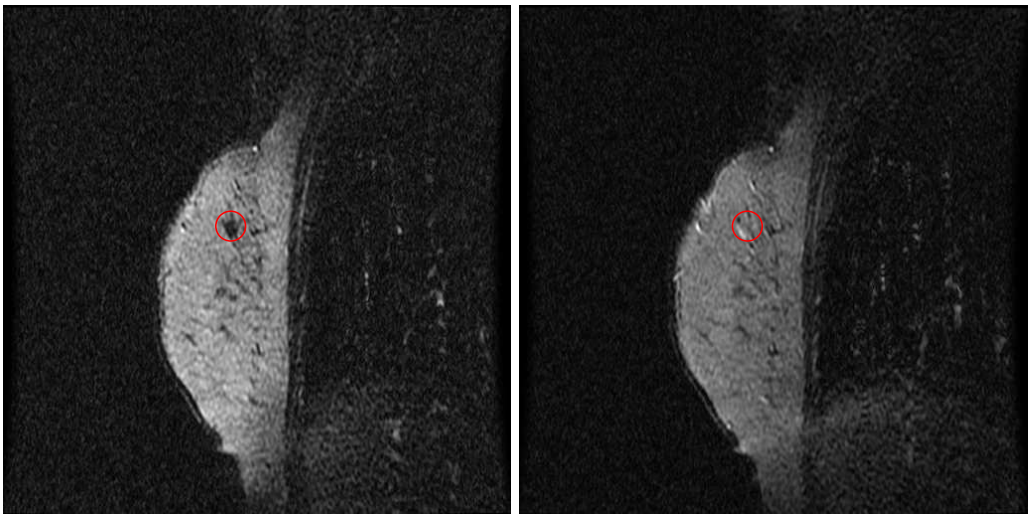

(a) Pre-contrast (b) Post-contrast

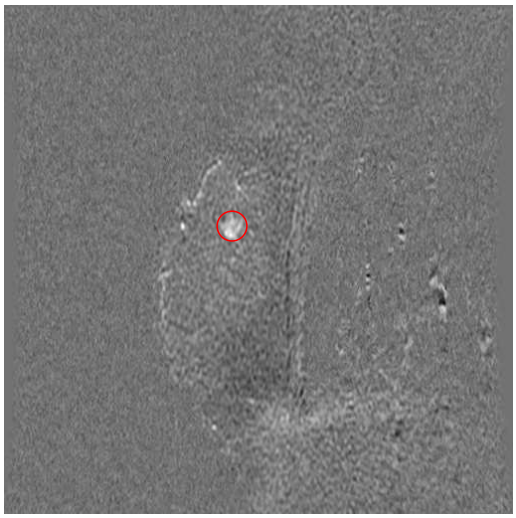

(c) Subtracted image

Figure 1.2: Regular breast MR images, the tumor is encircled

Another problem that occurs is the fact that there is a very significant inter-patient variability. This means that due to the specific physiology and anatomy of a patient, the same type of tumor in patients might give different curves. For example, patient with high blood pressure or patients who drink a lot of cafeïne will have faster enhancing curves in general.

Not only is there large inter-patient variability, there is a great deal of intra-patient variability too. When a patient has two measurements on two separate days there will never be a 100% match between the curves from measurement one and measurement two. There is even a risk that the different curve may lead to a different diagnosis. These differences are not arbitrary and could even occur because of something as simple as drinking more coffee on day one compared to day two.

To solve above-mentioned problems, researchers have tried to incorporate pharmacokinetic modeling in the interpretation of the MR time series[52]. The advantage of pharmacokinetic modeling is that it attempts to use the signal intensity time curves to calculate the underlying physiological parameters of the tumor, which should be consistent between measurements, scanners and protocols. The parameters might even open up extra diagnostic potential in those curves.

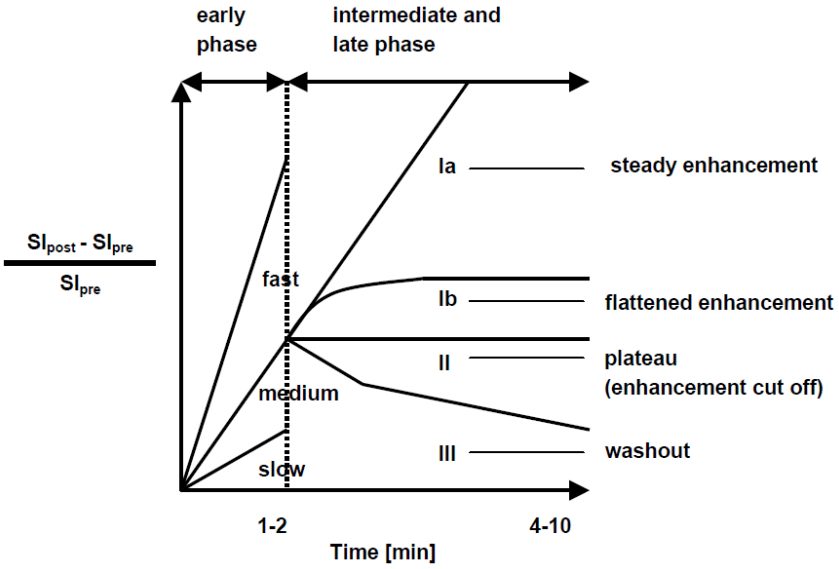

Figure 1.3: Classification based on three time point method

However, there is still much discussion about the way this should be implemented, for example what models to use and what assumptions to make. Some approaches might not even be implementable in clinical practice because of increase in scan time or the added extra measurements that are needed in the patient. This thesis hopes to shine a light on what methods are available, what their limitations are and what types of clinical data are required for useful analysis.

1.5 Research goals

As has been outlined in the previous sections, breast cancer is a big health problem in modern society. However, when detected early enough five year survival rate approaches 100%. It is thus of great importance that good screening programs are implemented, which are usually done using X-Ray mammography. In high risk cases, for example women with a genetic predisposition, it is usually better to use MRI. MRI should also be the modality of choice when other findings are inconclusive because of the higher sensitivity. There are several problems when using MRI signal intensity time curves, for example the inter- and intra-patient variability. A lot of the problems can be solved using pharmacokinetic modeling. There is still a much research going on in how to implement these models and this thesis hopes to answer some of these questions.

The University of Chicago Medical Center has provided us with several patient data sets that have a high-temporal resolution sagittal image sequence in addition to the standard diagnostic scans. These will be used as input for our studies on the pharmacokinetic models, but we will also try to give suggestions on how to improve the high-temporal imaging sequence to better complement the models in general. In chapter 2 we will look into what data we have and how they were acquired. Throughout the thesis we will try to suggest improvements in the acquisition.

In chapter 3 we will discuss the conversion of the signal vs. time curves to concentration vs. time curves using the gradient echo signal model. This is required because the input of the pharmacokinetic models requires a concentration curve. During this chapter we will see that pre-contrast tissue T1 plays a big part in the correct translation of signal intensity to concentration and we will look into several ways to find T1 to finally come to a protocol on conversion from signal intensity to concentration.

In chapter 4 we will introduce pharmacokinetic modeling, we will go into the basics, different types of models and differences in assumptions one can make. We will discuss the standard and

extended Tofts models, the Brix model and the shutter speed model. In this chapter we will use simulations to determine the errors we make when using those models on clinical data and find data requirements in temporal resolution and noise level for each model. We hope this will result in a solid advice on what models to use in what setting.

Chapter 5 will cover the basics of obtaining the arterial input function (AIF), the input of our models. There are several ways to obtain this, using literature AIFs or obtaining one from the data itself. For this step we also try to find a protocol for clinical data. In chapter 6 we will put the pharmacokinetic models to practical use and fit them to our acquired concentration curves. Furthermore, we will look into the clusters of parameters for specific cancer types and for benign/malignant classification. Chapter 7 will be reserved for discussion on the results and the conclusion that can be drawn from this research.

Chapter 2

Overview and processing of patient data

In this chapter we will review the data we have obtained from the University of Chicago Medical Center. We will look into the acquisition of these data sets and will detail the preprocessing steps necessary to analyse the data. Lastly, the difficulties we encountered will be mentioned for which we try to find solutions in the coming chapters.

2.1 Acquisition

The data we have obtained from the University of Chicago Medical Center has been acquired some time ago using a General Electric 1.5 Signa MRI scanner. In addition to the regular clinical scans we have one sagittal data set per patient of three to five slices at and around the tumor location, this data set has a high temporal resolution between 3.4 and 7 seconds during the first 90 seconds during and after contrast administration.

The regular clinical scans consist of a pre-contrast coronal scan of the entire chest area, four or five post-contrast coronal scans of the entire chest area, usually also a T1 and T2-weighted pre-contrast bilateral axial scan and several localization scans. Furthermore we have obtained the reports of these patients, including the final diagnosis of the finding. The pre and post contrast coronal scans and the extra high temporal resolution scans are used in the data analysis. (Figure 2.1)

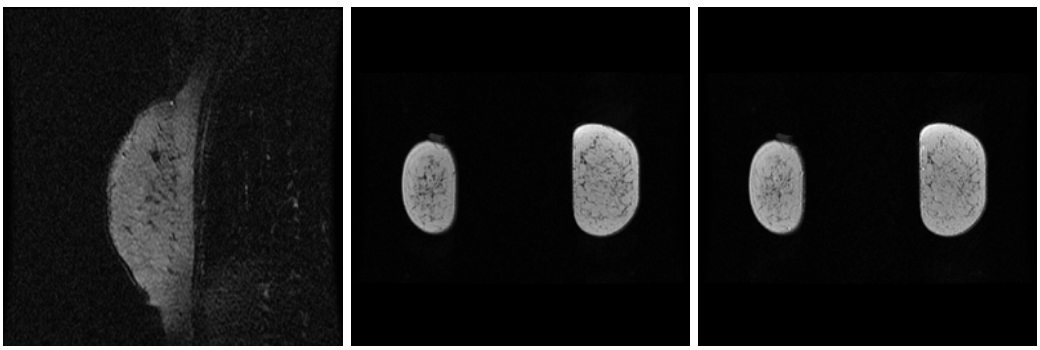

(a) Sagittal data (High Temporal Resolution) (b) Coronal (Pre-Contrast Agent) (c) Coronal (Post-Contrast Agent)

Figure 2.1: Example data set

This data was acquired using a heavily T_1 weighted acquisition. The MRI sequence is an

implementation of gradient recalled echo MRI on the GE Signa scanner, called SPGR (Spoiled Gradient Recalled). SPGR is an imaging sequence based on basic gradient echo, but incorporates removal of the transverse magnetization with a random phase shift in the RF pulses, prohibiting the transversal magnetization to reach steady state. This maximizes T1 contrast and allows for low TR and flip angle values, leading to rapid imaging. Typical TR and TE values during acquisition were on average 8 and 4 ms with flip angles 30 - 40 degrees. All images were acquired in a single scanning session. A dedicated bilateral breast coil was used during imaging. A more detailed overview of the patient data used in this thesis can be found in Appendix A. During the high temporal resolution scan the patient was injected with a bolus of 20 cc Gd-DTPA (Omniscan) and scanned for five to seven minutes thereafter, in which the low temporal resolution images are made.

The patients who were scanned for this research had varying types of cancer with a high number of patients having either IDC or DCIS. Patient ages varied from 36 to 85 years and all were female. Patient data was fully anonimized prior to use in this research. No other significant details about the patients were known to us.

To acquire images at high temporal resolution some sacrifices have to be made. In our data sets the spatial resolution of the high and low temporal resolution images differ slightly, the slice thickness is usually different as are the flip angle and repetition and echo times. In addition, in some cases the acquisition matrix size and the number of averages are different. This leads to a wide range of differences in signal intensities and noise levels.

Before we can look at the effects these differences have, the first problem we need to solve is that we do not have our data sets in the same plane. To convert a data set to another plane we need the absolute coordinates and voxel resolutions of the data sets from the DICOM (Digital Imaging and Communications in Medicine, a standardized file format[32]) tags. Then we can calculate the absolute coordinates for each voxel in our sagittal data and find the corresponding location in the coronal data. We use bicubic interpolation to find in between voxel values. This way we can construct the sagittal slices from coronal data. The results are shown in figure 2.2

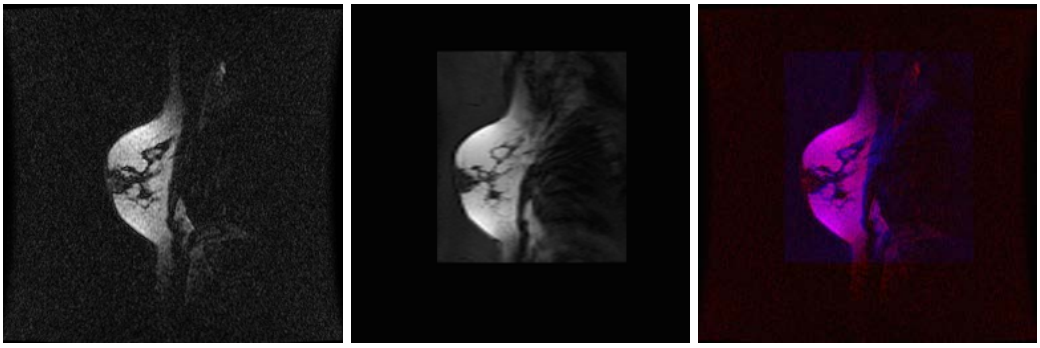

(a) Sagittal data

(b) Converted coronal at the same location

(c) Color map, purple indicates corresponding pixels, red and blue correspond to higher intensity in either the original or the converted image

Figure 2.2: Transformation from coronal to sagittal

After visual inspection of the images and comparing the edges of the breast we concluded that no extra image registration was necessary to correct for motion artifacts as differences were small.

The differences in noise level can also pose a problem, the level of noise in the high temporal resolution images is a lot higher than in the low temporal resolution images. This could reduce the quality of the pharmacokinetic model fit, especially in lesions or tissues with low enhancement. We can reduce the amount of noise in the high temporal resolution data using noise reduction algorithms.

2.2 Noise reduction

To understand the origin of the noise let us have a look at a condensed version of how images are acquired in MRI. In MRI images are acquired by filling k-space with the Fourier transform of the acquired free induction decay (FID). We can express each frequency component as a complex number. We can then express the noise (which is mostly caused by thermal noise in the patient) as complex Gaussian white noise. Usually k-space images are then transformed to the spatial domain using the inverse Fourier transform, after which a magnitude image is created by taking the absolute value of each complex number. This means that for the signal we can write

$$S_{\mathrm{Mag}} = \sqrt{(S_{\mathrm{Re}} + n_{\mathrm{Re}})^2 + (S_{\mathrm{Im}} + n_{\mathrm{Im}})^2} \tag{2.1}$$

This means that in magnitude images the noise has a Rician distribution. In a paper by Sijbers et al.[47] the implications of this on the estimation of signal amplitude from complex data or magnitude data has been investigated. A Rician distribution means that the noise bias is signal dependent. However, in regions with a signal-to-noise ratio (SNR) higher than 5 the bias tends to zero (Rician distribution can then be approximated with a Gaussian) and there is no significant difference in the estimation of signal amplitude between complex data and magnitude data. In our image data tumor regions usually have an SNR of roughly 10 (high temporal resolution) to 30 (low temporal resolution), so we can assume the bias is around 0 in those regions. The noise variance might still pose a problem in the lower SNR regions.

There are several filters to reduce the noise in MRI images. In a review study by Buades et al.[5] several different filters (Perona and Malik geometry driven diffusion for example) were compared and the Non Local Means filter was the best performing method.

$$\begin{aligned}
&\mathrm{NLM}(I(p)) = \sum_{\forall q \in I} w(p,q) I(q) \\
&w(p,q) = \frac{1}{Z(p)} e^{-\frac{d(p,q)}{h^2}} \\
&Z(p) = \sum_{\forall q} e^{-\frac{d(p,q)}{h^2}} \\
&d(p,q) = G\|I(N_p) - I(N_q)\| \\
&\text{where } 0 \leq w(p,q) \leq 1 \text{ and } \sum_{\forall q \in I} w(p,q) = 1
\end{aligned} \tag{2.2}$$

The ideal parameters h and the neighborhood size (which we will call R_{Sim}) for this filter in noisy MRI images were determined in a later study by Manjón[27]. The filter is based on the formulae in 2.2. The step-by-step overview of the filter is:

1. Start at a pixel p, determine its neighborhood which is a square with dimensions $2R_{\mathrm{Sim}}$ centered around p
2. For another pixel q, determine its neighborhood. Calculate a distance measure using a Gaussian weighted Euclidean distance between the two neighborhoods.
3. Repeat this process for every pixel, then calculate $Z(p)$
4. Determine w(p,q) for every pixel and multiply with the pixels intensity.
5. Summation of all weighted pixel values will give the filtered value for pixel p
6. Repeat for every pixel

As the method is very computationally intensive it is usually more practical to define a 'search'-window around a pixel instead of using the entire image for analysis. The larger the search window, the better the result, meaning the lower the intensity of the remaining noise.

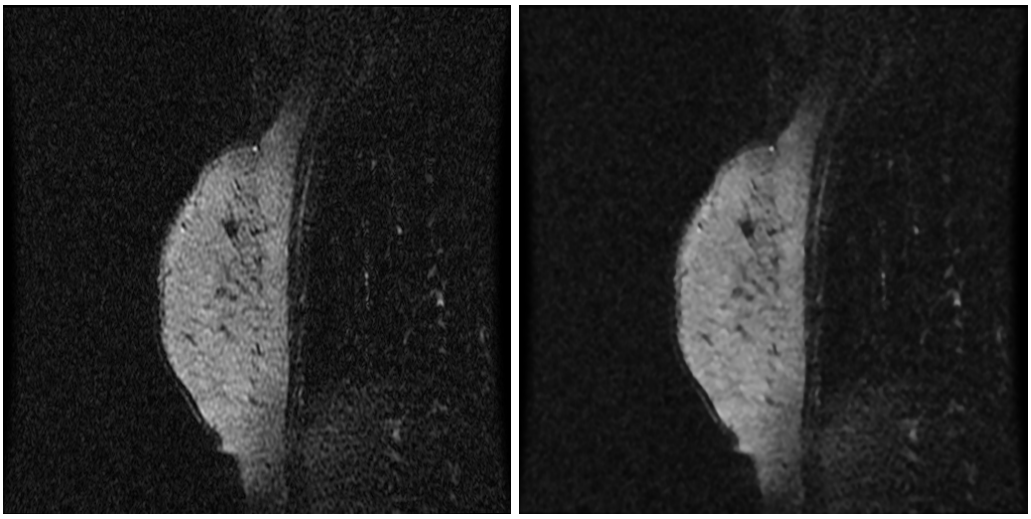

(a) Original

(b) Search Window size 10x10

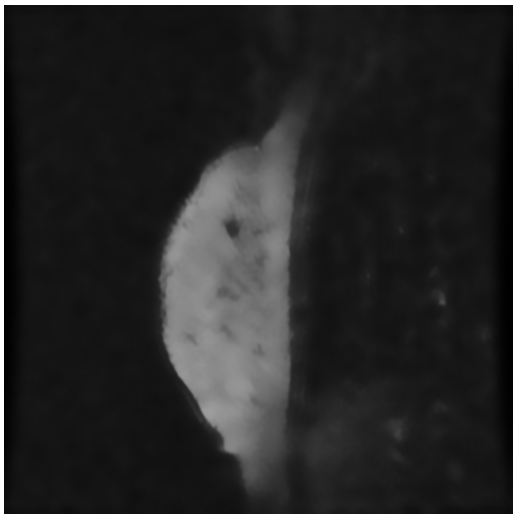

(c) Search Window size 40x40

Figure 2.3: Noise reduction using Non-Local Means

The results are shown for two different window sizes in figure 2.3. The strength of the noise can be measured as its standard deviation, we can estimate that from the background (where signal amplitude should be zero) using $\sigma = \sqrt{\frac{\mu}{2}}$ (Nowak)[35]. Using non-local means we can achieve a noise reduction of 29% and 42% respectively, depending on the size of the search window. However, the algorithm is rather slow and we always loose some image detail in the process, thus it might be better to skip noise reduction in cases where enhancement is sufficient. In chapter 3 we will look into the robustness of the pharmacokinetic models to noise, after which we can decide to use or not use noise reduction.

2.3 Extraction of signal-vs.-time curves

To extract the signal-vs.-time curves from the tumor or other tissue we first visually inspected the reports generated by the radiologists. They encircled their findings in a key image in the report,

which we then used to find the tumor in the original data set. An example of the images in a report and a signal time curve from a report are shown in figure 2.4. After we know the tumor location we need to find the time axis of the curve, which we can extract out of the DICOM files using the field acquisition time and trigger time.

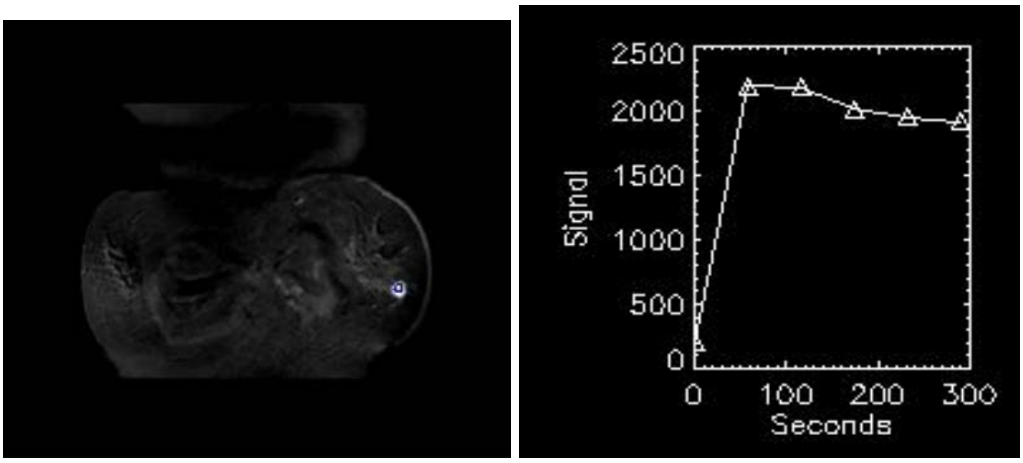

(a) Key image, tumor is clearly visible, ROI marked with a blue circle

(b) Signal-vs.-time curve, the signal intensity (y-axis) is the total of the pixels in ROI

Figure 2.4: Example images from patient report

We programmed a small user interface in Wolfram Mathematica to extract the curves, a picture of the interface is shown in figure 2.5. The extraction of the curve occurs by extracting the pixels from a region of interest (ROI), which is drawn by the user. We also created a switch to only select the 20% most enhancing pixels within the ROI. The most enhancing pixels are determined by comparing the highest intensity value of a pixel with lowest intensity value of the same pixel. Radiologist do the same creating their reports, although they use visual inspection to determine the region of most enhancement, which we know through personal communication. In figure 2.6 we show an example of the signal intensity vs. time curve, both using the entire ROI and only using the most enhancing pixels which are 9-connected. In the rest of this thesis we will only use the regular ROI method to reduce the risk of selecting only pixels which have a large plasma fraction (and thus a high concentration of contrast agent), which may lead to a wrong characterization of the tissue.

As can be seen in figure 2.6 and was mentioned in the beginning of this chapter, we have a problem in that the signal intensities in the lower and the higher temporal resolution data sets cannot be connected, mainly due to differences in the acquisition of these images. To correct this we want to convert this signal intensity to concentration using a signal model.

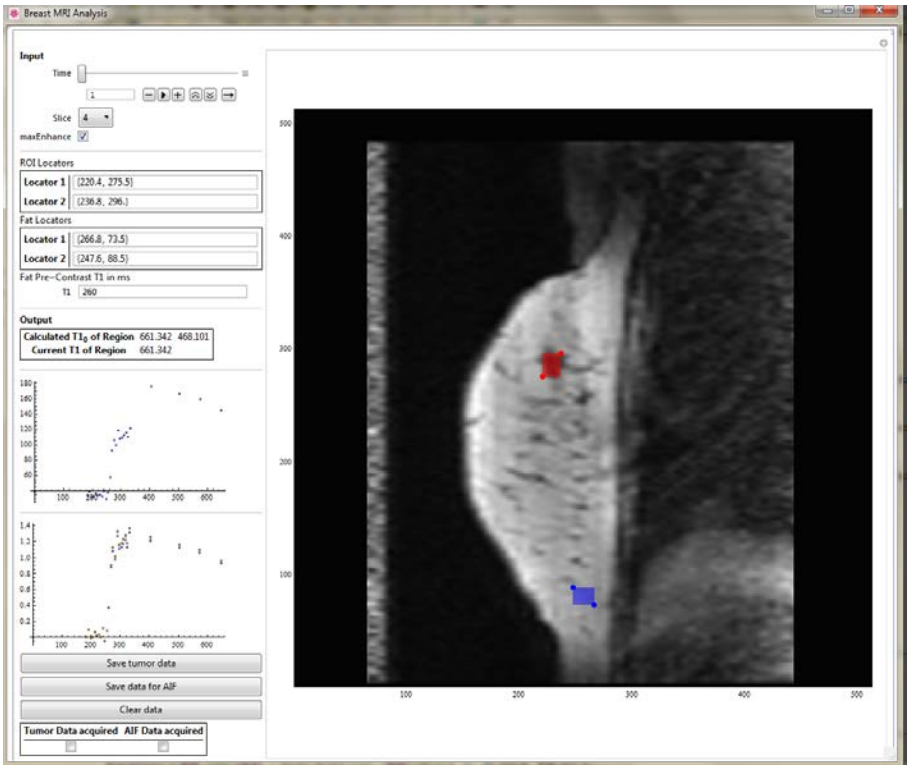

Figure 2.5: Interface of the data analysis tool

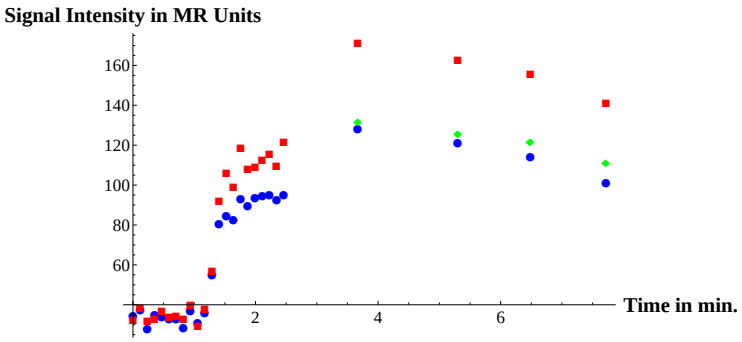

Figure 2.6: Blue dots are the pixels in the normal ROI in the tumor, red squares are the pixels in the highest enhancement ROI in the tumor, yellow diamonds are the pixels in the radiologist ROI, assuming ROI size is 9 pixels (note that here we do not have a high temporal part). Low temporal parts of the curves start at approximately 400 seconds.

Chapter 3

Conversion of signal intensity to concentration

As mentioned in the previous chapter, it is required to convert our signal-vs.-time curve to a concentration-vs.-time curve in order to use our pharmacokinetic models. If we would choose to fit directly to relative signal enhancement curves we would induce a large T1 dependent bias, giving worthless pharmacokinetic parameters. In this chapter we studied the use of a signal model for the assessment of the concentration of contrast agent. Firstly, we will discuss the shortcomings of the model when compared to reality. Secondly, we looked into the various simplifications of the model and the effects thereof. Then the estimation of $T_1[0]$ used for model input is covered and after that the conversion of clinical data to concentration is studied.

3.1 Signal Model for Gradient Echo Imaging

In clinical practice most T1-weighted images in which scanning time is an important factor are acquired using a gradient echo based image sequence. For these types of images the signal intensity of a voxel can be approximated using the following solution of the Bloch equations for a FLASH sequence:

$$S = k\rho \frac{\mathrm{Sin}[\theta]\left(1 - e^{-\frac{\mathrm{TR}}{T_1}}\right)}{1 - \mathrm{Cos}[\theta] e^{-\frac{\mathrm{TR}}{T_1}}} e^{-\frac{\mathrm{TE}}{T_{2^*}}} \tag{3.1}$$

k	()	Scanner gain
ρ	()	Proton Density
θ	(Degree)	Flip Angle
TR	(s)	Repetition time
TE	(s)	Echo time
T_1	(s)	Longitudinal relaxation time of the voxel
T_{2^*}	(s)	Transverse relaxation time including field inhomogeneities of the voxel

Of course this model is a simplification of the real situation, as perfect spoiling and flip angle homogeneity are examples of assumption we make during the use of this model. In addition, slice profiles are never perfectly rectangular. We do however, in contrast to regular gradient recalled echo, have a RF (radio frequency) spoiled gradient recalled echo (SPGR) sequence, which makes the assumption of perfect spoiling a reasonable one. With extra measurements during the acquisition of the patient data it would also be possible to remove flip angle inhomogeneity, although this is not trivial, but that data was not available during this project. However, this model is widely used in scientific research and has been shown to give accurate predictions of signal intensity.[3;45;60;29]

If we take a closer look at equation 3.1 we see several unknown variables. We do know the flip angle (θ in the formulae, FA in the text), repetition time (TR) and echo times (TE), however we do not know T_1, T_{2^*}, k and ρ. Before we solve this problem, let us first introduce concentration to the equation so we have a complete overview. We will use the following substitutions were $R_1 = \frac{1}{T_1}$ and $R_{2^*} = \frac{1}{T_{2^*}}$:

$$R_1[0] = R_1[0] + r_1 C[t] \tag{3.2}$$

$$R_{2^*}[t] = R_{2^*}[0] + r_2 C[t] \tag{3.3}$$

$$S = k\rho \frac{\sin[\theta]\left(1 - e^{-\mathrm{TR}(R_1[0]+r_1C[t])}\right)}{1 - \cos[\theta] e^{\mathrm{TR}(R_1[0]+r_1C[t])}} e^{-\mathrm{TE}(R_2^*[0]+r_2C[t])} \tag{3.4}$$

$R_1[0]$	(s^{-1})	Longitudinal relaxation rate at a contrast agent concentration of zero
$R_{2^*}[0]$	(s^{-1})	Transverse relaxation rate including field inhomogeneities at a contrast agent concentration of zero
r_1	$((mMol/L)^{-1}s^{-1})$	Relaxivity of the contrast agent on R_1
r_2	$((mMol/L)^{-1}s^{-1})$	Relaxivity of the contrast agent on R_{2^*}
$C[t]$	$(mMol/L)$	Concentration at time t
$R_1[t]$	(s^{-1})	Longitudinal relaxation rate at a contrast agent concentration $C[t]$ at time t
$R_{2^*}[t]$	(s^{-1})	Transverse relaxation rate at a contrast agent concentration $C[t]$ at time t

The concentration formulae are based on the effect of a contrast agent on the relaxation rate in a homogenous solution of a liquid, which is approximately linear. The r_1 and r_2 are relaxivity constants which depend on the magnetic field strength but not on tissue type, if we assume that the contrast agent always has access to all tissue water. For low concentrations this is true, but for higher concentrations this might be invalid. We will investigate this in chapter 4. For now, we will assume the linear relation to be true and then the relaxivity constants are 3.9 $\pm$ .2 and 5.5 $(mM^{-1}s^{-1})$ for r_1 (for r_1 we obtained the information from the University of Chicago Medical Center) and r_2 respectively[23;45] for Gd-DTPA (Omniscan) at 1.5 Tesla.

3.1.1 Eliminating unknown variables

The concentration is the variable we would like to know, so that means that we have to find a way to calculate or eliminate the other variables. Let us start with looking for a way to remove or estimate k and ρ.

If we look within a series of images which are acquired using the same imaging sequence and parameters we can state that the scanner gain and proton density at a spatial location are the same between images, so we can remove them from the equation by using:

$$\frac{S[t]}{S[0]} = e^{-\mathrm{TE}r_2C[t]} \frac{(1 - \cos[\theta]e^{-\mathrm{TR}R_1[0]})}{1 - e^{-\mathrm{TR}R_1[0]}} \frac{(1 - e^{-\mathrm{TR}(R_1[0]+r_1C[t])})}{(1 - \cos[\theta]e^{-\mathrm{TR}(R_1[0]+r_1C[t])})} \tag{3.5}$$

As you can see this also removes $R_2^*[0]$ from the equation, although the relaxation effect of the contrast agent on the relative signal intensity are still present. However, what we want to know is not the relative signal intensity, which is what we have, but the value of the concentration at a time t. To calculate the concentration we would need to rewrite equation 3.5, which is not possible in the current form. We are able to solve it numerically, but this requires a slightly more cumbersome calculation.

There is a way to solve equation 3.5 analytically for the concentration if we simplify the R_{2^*}-term. This means that we will simply neglect R_{2^*} effects. If we could state that the exponential term is approximately 1, we could find an analytic solution. We will do a short investigation in the error we introduce would we neglect R_{2^*}-effects.

Assuming that we have a TE of 4.2 ms, a TR of 8.9 ms and a flip angle of 30°(which is comparable to what we have in the clinical data) and relaxivities are r1 = 3.9 $((mMol/L)^{-1}s^{-1})$ and r2=5.5 $((mMol/L)^{-1}s^{-1})$ we can investigate the error between the simplified model and the normal model. We define the error as the deviation of the simple model from the normal model:

$$\text{Error} = \frac{C[t]^{\text{Full}} - C[t]^{\text{Simple}}}{C[t]^{\text{Full}}} \tag{3.6}$$

This gives an error in percentages when we calculate the concentration at a time t using both models. Assuming a $T_1[0]$-range of 200 - 1400 ms, which is the range of tissue $T_1[0]$ we find in the breast[44] we look at the errors when the concentration approaches 1 mM/L. This is a value that is hardly ever reached in tissue, even in tumors, using the injection protocol that was used in our patients, which is similar to those in literature[42;58]. For these conditions we found that the error is lower than 5%. This is why we decided to neglect this term, as it is relatively small. In addition, it simplifies the calculation of some derivations for uncertainty analysis in section 3.2. The final equation then becomes:

$$\frac{S[t]}{S[0]} = \frac{(1-\cos[\theta]e^{-\text{TR}R_1[0]})}{1-e^{-\text{TR}R_1[0]}} \frac{(1-e^{-\text{TR}(R_1[0]+r_1C[t])})}{(1-\cos[\theta]e^{-\text{TR}(R_1[0]+r_1C[t])})} \tag{3.7}$$

And for $C[t]$:

$$C[t] = \frac{\ln\left[\frac{-1+e^{-R_1[0]\text{TR}}\cos[\theta]+\frac{S[t]}{S[0]}\cos[\theta]-e^{-R_1[0]\text{TR}}\frac{S[t]}{S[0]}\cos[\theta]}{-e^{R_1[0]\text{TR}}-\frac{S[t]}{S[0]}+e^{R_1[0]\text{TR}}\frac{S[t]}{S[0]}+\cos[\theta]}\right]}{r_1\text{TR}} \tag{3.8}$$

There still is one variable left that is unknown and that is $R_1[0]$. The estimation of $R_1[0]$ is an important part in the determination of the concentration of the contrast agent, wrong estimates can lead to large deviations, as already mentioned in the introduction.

3.1.2 Estimation of $R_1[0]$

Normally, extra imaging time is needed to estimate T_1 in tissues. Two typical examples for the measurement of T1 are the use of saturation recovery sequences and multiple flip angle measurements. The problem using these kind of acquisitions in a clinical setting is that they need to be acquired in addition to regular clinical scans, leading to an increase in scanning time and thus in patient discomfort and expenses. Our goal was to find a way to extract T1 information from the regular clinical scans and the high temporal resolution scan without using extra information.

Firstly, we looked at the two pre-contrast images we have from the regular clinical scan and the high temporal resolution scan. These images were obtained using the same imaging sequence but with different parameters TR, TE and θ. The proton density of a voxel at the same spatial location in those two images will be the same and let us for the moment assume that the scanner gain is the same between these two images. Still assuming that R_{2^*} effects are negligible we can obtain the following expression for the relative signal intensity:

$$\frac{S_1}{S_2} = \frac{\sin[\theta_1]}{\sin[\theta_2]} \frac{(1-e^{-R_1\text{TR}_1})(1-\cos[\theta_2]e^{-R_1\text{TR}_2})}{(1-e^{-R_1\text{TR}_2})(1-\cos[\theta_1]e^{-R_1\text{TR}_1})} \tag{3.9}$$

The problem with this equation is that there is only good separation between R_1 values if the flip angles and/or the repetition time are significantly different. To give an example that is typical for our data in case of the same flip angles, let us assume a TRs of 7.7 and 8.9 ms and a flip angle of 30 for both. If we then determine the ratio of signal intensity of a tissue with a R_1 of 1/200 ms^{-1} we get a value of 0.893 and with a tissue with a R_1 of 1/500 ms^{-1} we get 0.878, which are very close to each other. This seems to indicate that determination of R_1 using this method is very sensitive to small fluctuations. This means that a wrong estimation, for example due to noise, of either S_1 or S_2 can lead to large errors in R_1. To test this hypothesis we did a small experiment.

Let us assume we have a signal to noise ratio of 10 in the high temporal resolution data, and assuming no noise in the low temporal resolution data we can estimate the error we make in determining R_1 this way. If we would assume a ratio of .893 and have a error of half a noise standard deviation we would get .848 or .937. This means that instead of the value it should be, $R_1 = 1/200$ ms^{-1}, we would obtain $R_1 = 1/46.4$ or $1/483.3$ ms^{-1}, which are large deviations from the true value. A large ROI could reduce the error (the mean of white Gaussian noise is 0, so the larger the number of voxels in the ROI, the higher the chance that we would obtain a mean of 0), but those can not always be drawn. Because much of our clinical data has differences in TR and flip angle in these ranges this method is not ideal for our purposes. In addition, the assumption that the scanner gain parameter is constant between two sequences which differ in parameters is possibly false.

Another approach could be the use of a reference tissue within the same image, as has been done in a study by Medved et al[29]. This is based on the assumptions that the R_1 of the reference tissue is stable among patients compared to tumor R1. In our case we decided to use fat, as in our non-fat suppressed images this is the most abundant tissue and its R_1 value is relatively stable among a large population (typical values range between 260-300 ms[46;4;6] compared to tumor T1 (500 - 1200 ms[51]). Secondly, we assume that the proton density difference between the tumor and the fatty tissue is small compared to the difference in R_1. This assumption has been made by several other researchers[29;11], however none provided conclusive evidence. What we do know however that in for example the brain the difference in proton density almost never surpasses 20%[31;50], whereas R_1 values can vary up to 7 times. For the breast this assumption might be even closer to the truth as the breast has a more homogenous tissue distribution. Nonetheless, before application of this method in a real clinical setting this assumption should be validated by proton density weighted imaging of several breast lesions. If this assumption does not hold but proton density is a rather stable parameter amongst tumors one might use a simple correction factor with which to multiply the resulting R_1. If the spread in proton density for tumors is large the situation becomes more complicated. However, a high proton density is related to an increased water content in the tissue (for example in highly vascular tumors) and this is also often related to a smaller R_1 value. It might then be possible to create some sort of lookup table between the estimated R_1 and the proton density, thus still allowing a simple correction factor. However, as mentioned, further research is needed to validate these claims.

Mathematically this method can be expressed by formula 3.10

$$S_{\text{rel}} = \frac{(1 - e^{-R_{1t}\text{TR}})(1 - e^{-R_{1r}\text{TR}}\cos[\theta])}{(1 - e^{-R_{1r}\text{TR}})(1 - e^{-R_{1t}\text{TR}}\cos[\theta])} \text{ where } S_{\text{rel}} = \frac{S_{\text{Tumor}}}{S_{\text{Reference}}} \tag{3.10}$$

Subscripts r and t represent reference tissue and tumor respectively. We can rewrite this for R_{1t}:

$$R_{1t} = \frac{\ln[\frac{-e^{R_{1r}\text{TR}} + \cos[\alpha] - S_{\text{rel}}\cos[\alpha] + e^{R_{1r}\text{TR}}S_{\text{rel}}\cos[\alpha]}{-e^{R_{1r}\text{TR}} - S_{\text{rel}} + e^{R_{1r}\text{TR}}S_{\text{rel}} + \cos[\alpha]}]}{\text{TR}} \tag{3.11}$$

Now let's look at the effects of small uncertainties in the estimation of S_{rel} in the same way we did with the previous example (were only TR differed). Let's assume that the T_1 of fat is 280 ms, TR=8.9 ms and the flip angle is 30 degrees. If the tumor has an R1 of 1/200 or 1/500 we would get an S_{rel} of 1.31 or .608 respectively, which are already a lot more separated then the previous example. If there would be an error of one half noise standard deviation these values would lead to estimated $R_1 s$ of 1/212.8 or 1/186.6, which means the errors in R_1 are significantly smaller.

If we then look at the effect of a wrong assumption of the reference tissue R_1, assuming that the real fat value would be 300 and we use 260 we would get an error of approximately 14% which gets smaller as tumor R_1 gets smaller. For example for tumors with $R_1 s$ of 1/200, 1/500, 1/700 and 1/1000 ms^{-1} we would get estimates of 1/171, 1/438, 1/615 and 1/882 ms^{-1} which are errors of 14.4%, 12.4%, 12.0% and 11.7% compared to the real value. Although this error is still quite large, it is still a lot better than assuming a constant value for R_1 or using the method we previously mentioned.

To circumvent the error caused by wrong assumption on reference tissue R_1 we proposed a method using a reference phantom, which could be scanned together with the patient. In this phantom we have several tubes with different R_1 values. We can further reduce the errors by using several reference tubes for the estimation of R_1 of the tumor and then taking the mean of the estimated $R_1 s$. This method performs just as well as regular clinical R1 estimation methods and an abstract has been submitted to the RSNA 2009 conference and has also been accepted. A copy of this abstract can be found in appendix B. Further research needs to be done in assessment of the proton density differences between the phantom (in which the proton densities are the same between tubes) and tumor tissue, because they are probably not the same.

Lastly, the estimation of R_1 can suffer from large errors due to the B_1 inhomogeneity, inhomogeneities in the radio-frequent pulses used to flip the magnetization in the transverse plain, which especially are a problem at higher magnetic field strengths. However, even in 1.5T scanners flip angle values have a standard deviation of 10% in a human brain using a head coil[9]. Simply put, this means that the effective flip angle differs depending on spatial location, being closer to the specified angle in the center of the transmitter coil. There are roughly two ways to solve this, the first being the use of a flip angle map to correct for the inhomogeneities, however, as every type of tissue has a different effect on the flip angle, this is not trivial. Secondly, you can also use adapted pulse sequences to remove the B_1 inhomogeneity[2]. However, as we do not have these kinds of options available, we cannot correct for this error. In General Electric scanners, the scanner software usually makes sure that the flip angle in the center of our slice is approximately equal to the specified flip angle[9]. The inhomogeneity is then usually distributed radially from this point (in uniform phantoms). That means that in order to minimize the effect of spatial differences in flip angle we should select the regions of interest in the tumor and the reference tissue as close as possible to the center of the slice and close to each other.

Imperfections in the slice profile (as the slice profile is never perfectly rectangular) can also lead to errors, sadly, we cannot correct for this as we have no knowledge about what for example the shape of the slice selection pulse is.

Simplification of the R_1 formula

In several papers simplifications of formula 3.11 are used to calculate R_1 without evidence that this is allowed. Let us first go through the simplification steps starting with equation 3.10:

$$\begin{aligned} S_{\text{rel}} &= \frac{(1-e^{-R_{1t}\text{TR}})(1-e^{-R_{1r}\text{TR}}\cos[\theta])}{(1-e^{-R_{1r}\text{TR}})(1-e^{-R_{1t}\text{TR}}\cos[\theta])} \\ &\quad \text{if } R_1\text{TR} \ll 1 \Rightarrow e^{R_1\text{TR}} = 1 - R_1\text{TR} \\ S_{\text{rel}} &= \frac{1-(1-R_{1t}\text{TR})(1-(1-R_{1r}\text{TR})\cos[\theta])}{1-(1-R_{1r}\text{TR})(1-(1-R_{1t}\text{TR})\cos[\theta])} \\ &\quad \text{if } R_1\text{TR} \ll 1 \Rightarrow \cos[\theta]R_1\text{TR} \ll 1 \\ S_{\text{rel}} &= \frac{R_{1t}}{R_{1r}} \Rightarrow R_{1t} = R_{1r}S_{\text{rel}} \end{aligned} \tag{3.12}$$

The advantage of these assumptions are that the equation is no longer dependent on the repetition time or the flip angle. Although the simplification induces errors due to the neglecting of the repetition time and the flip angle, these might be smaller than assumption of an incorrect flip angle due to the flip angle inhomogeneities. Lets look into that aspect in a little more detail. Firstly, lets have a look how the error in R_1 estimation behaves when we assume that the non-simplified model is the true model. We first calculate some relative signal intensities corresponding to a $R_1 s$ of 1/200,1/600,1/1000 and 1/1400 ms^{-1} with a flip angle of 30 degrees and a TR of 8.9 to get a feel for the range of the relative signal intensities. We then made contour plots of the error in percentages of the estimation of R_1 using the simplified model with varying flip angles and TRs. The formula of the error is similar in nature to the one we used earlier (equation 3.6), replacing the concentration with $R_1[0]$ and assuming equation 3.11 as the full model and final equation of 3.12 as the simplified model.

The results are shown in figure 3.1, where we can see that especially for the small $R_1[0]s$ we can have large errors, even approaching 15% in $R_1[0]$ for a flip angle of 30°and a TR of 8.9. This hints that the simplification should not be used. The next step is that we want to research if the

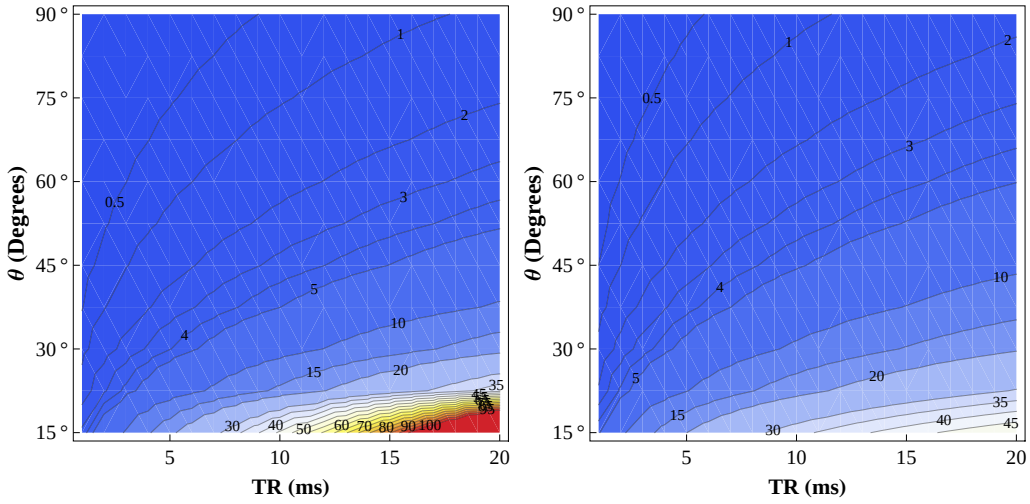

(a) $S_{\text{rel}} = 1.394$ corresponds to R1=1/200 ms^{-1} (b) $S_{\text{rel}} = 0.469$ corresponds to R1=1/600 ms^{-1}

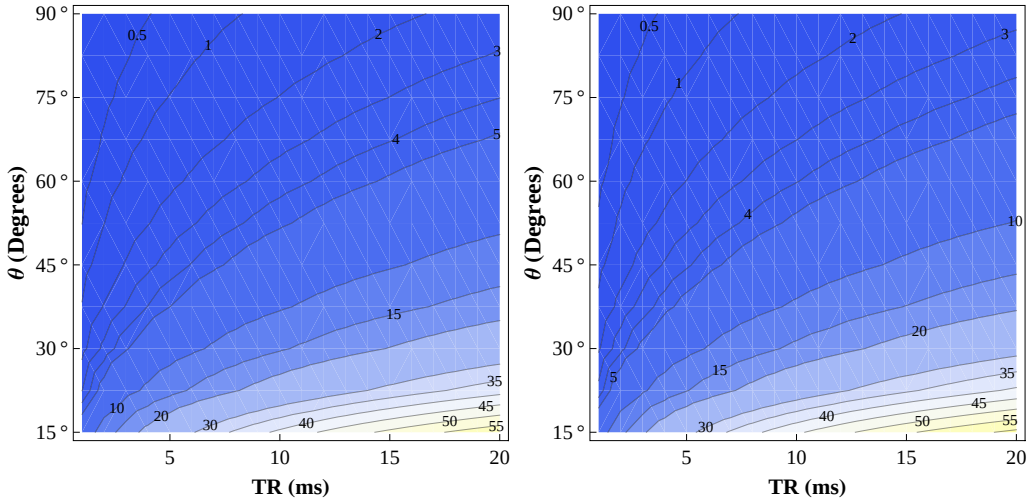

(c) $S_{\text{rel}} = 0.282$ corresponds to R1=1/1000 ms^{-1} (d) $S_{\text{rel}} = 0.201$ corresponds to R1=1/1400 ms^{-1}

Figure 3.1: Contour plots of the error in $R_1[0]$ when using the simplified model to estimate $R_1[0]$, comparing it to the full model. Flip angle and TR were changed to investigate the errors caused by simplifying. The contour lines separate the regions of errors and the labels represent the value at that line.

simplification has a smaller error than the complete model when we have an error in the flip angle. We assume that the flip angle that we enter in the models is 10% lower than the one specified during imaging, which is equal to the standard deviation of the flip angle in the brain in the article by Tofts[9]. We can assume it is lower because GE scanners make sure the specified flip angle is in the center of the slice, making the effective flip angle lower anywhere else in the image. We now simulate four situations: the error in $R_1[0]$ when $R_1[0]$ should be 1/200 ms^{-1} estimation using the complete model when there is a flip angle error of 10%, the error in $R_1[0]$ when $R_1[0]$ should be 1/200 ms^{-1} estimation using the simplified model when there is a flip angle error of 10% and both of them again when $R_1[0]$ should be $1/1400ms^{-1}$. The results of these calculations are shown in figure 3.2. Looking at these figures we see that the simple model never has a lower error than the

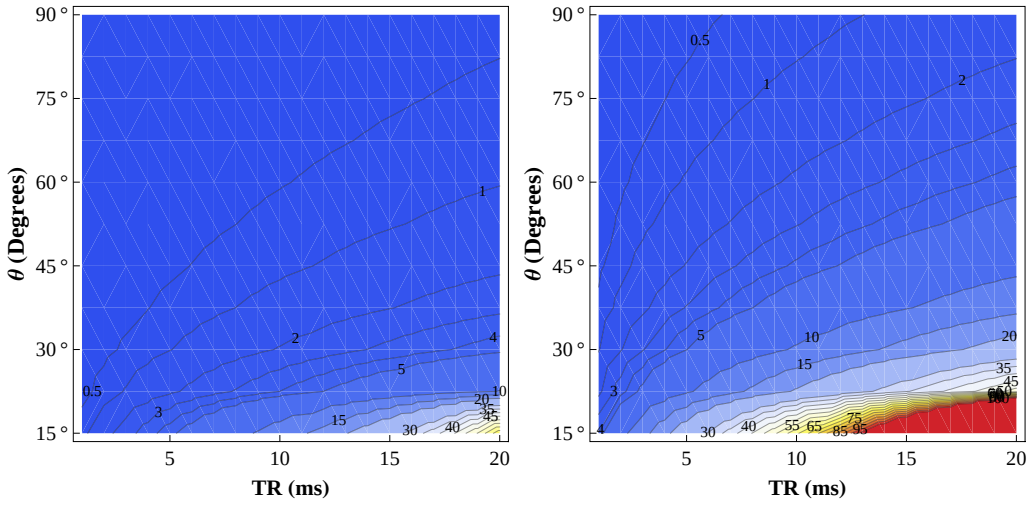

(a) Errors made by the complete model in estimation of R1=1/200

(b) Errors made by the simple model in estimation of R1=1/200

(c) Errors made by the complete model in estimation of R1=1/1400

(d) Errors made by the simple model in estimation of R1=1/1400

Figure 3.2: Contour plots of the error in $R_1[0]$ when estimating $R_1[0]$ when there is a flip angle error of 10% at different TR and flip angle

complete model, even at high values for the flip angle and low values of TR. To be absolutely sure that there is no point at which the simplified model performs better than the complete model we did another test using a flip angle error of 65%, of which the results are shown in figure 3.3. We see the same behavior, the error in the simplified model is still always larger than the complete model. As there is essentially no reason to simplify the model and the errors can become quite large (up to 15%) when we do simplify we chose to use the complete model.

3.2 Error propagation

Now that we know what kinds of errors we can expect in the different steps of the conversion to concentration, let's have a look at how these errors propagate into the uncertainty in the concentration estimates. For every non-linear function f dependent on multiple variables you can

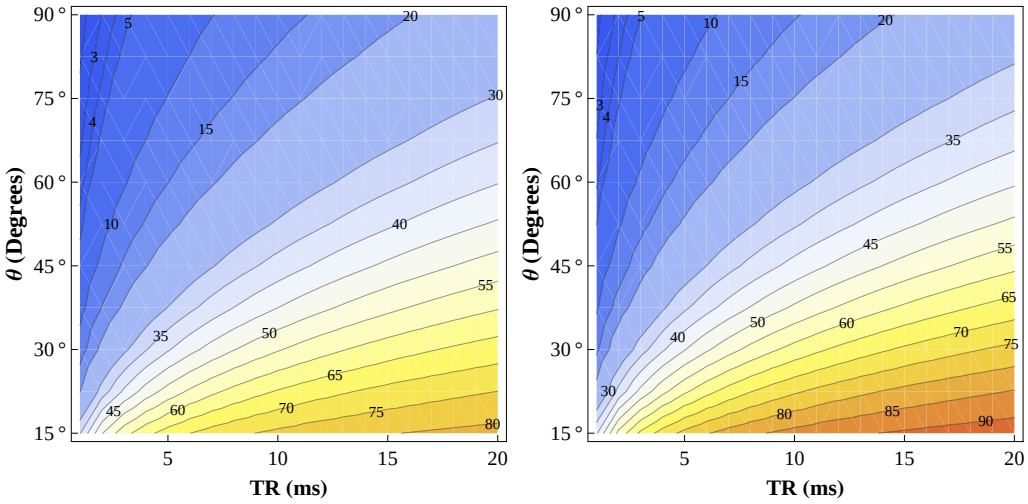

(a) Errors made by the complete model in estimation of R1=1/1400

(b) Errors made by the simple model in estimation of R1=1/1400

Figure 3.3: Contour plots of the error in $R_1[0]$ when estimating $R_1[0]$ when there is a flip angle error of 65% at different TR and flip angle

write a first order Taylor expansion around 0 were n is the number of variables:

$$f = f_0 + \sum_{k=1}^{n} \frac{\partial f}{\partial x_k} x_k \tag{3.13}$$

As f_0 is a constant and does not contribute to the error we may write the following for the standard deviation of f:

$$\sigma_f^2 = \sum_{k=1}^{n} \left(\frac{\partial f}{\partial x_k} \right)^2 \sigma_{x_k}^2 \tag{3.14}$$

If we have a look at the concentration formula (3.2) lets look into the variables that have an uncertainty. Lets assume that there is no uncertainty in TR, as we have no reason to assume there is any uncertainty there, which leaves the uncertainties in θ, $R_1[0]$, r_1 and S_{rel}. That means that the standard deviation can be written as:

$$\sigma_{C[t]}^2 = \left(\frac{\partial C[t]}{\partial \theta} \right)^2 \sigma_\theta^2 + \left(\frac{\partial C[t]}{\partial r_1} \right)^2 \sigma_{r_1}^2 + \left(\frac{\partial C[t]}{\partial R_1[0]} \right)^2 \sigma_{R_1[0]}^2 + \left(\frac{\partial C[t]}{\partial S_{t/0}} \right)^2 \sigma_{S_{t/0}}^2 \tag{3.15}$$

Here $S_{t/0} = S[t]/S[0]$. For the full analytical formula we direct the reader to appendix C. If we look at equation 3.15 we need to define values for the standard deviations of the parameters. For r_1 we know from the University of Chicago Medical Center that the uncertainty is .1 on the value of 3.9. In this formula, the standard deviations for the flip angle is assumed to be 10%, the same as previously and the flip angle inhomogeneity does not change when comparing $S[t]$ and $S[0]$ as they are in the same spatial location. For S_{rel} the standard deviation is estimated by using 3.14 for a simple division which results in:

$$\sigma_{S_{t/0}}^2 = \frac{1}{S_0} \sigma_S - \frac{S}{S_0^2} \sigma_{S_0} \tag{3.16}$$

Here σ_S and σ_{S_0} can be estimated from the image background as described in chapter 2.

Lastly, the standard deviation of $R_1[0]$ is a little more complicated, to find that one we need to do another Taylor expansion. Assuming again that there is no uncertainty in TR we get:

$$\sigma_{R_1[0]}^2 = \left(\frac{\partial R_1[0]}{\partial \theta} \right)^2 \sigma_\theta^2 + \left(\frac{\partial R_1[0]}{\partial R_{1r}} \right)^2 \sigma_{R_1}^2 + \left(\frac{\partial R_1[0]}{\partial S_{\text{rel}}} \right)^2 \sigma_{S_{\text{rel}}}^2 \tag{3.17}$$

Here we assume that the differences between the flip angle of the reference tissue and the flip angle of the tumor is negligible. If we chose the reference tissue ROI close to the tumor ROI than this is approximately true[9]. Again, for the complete mathematics the reader is referred to appendix C. In this formula, the standard deviations for the flip angle is assumed to be 10%, the same as previously. The relative signal intensity is analog to equation 3.16 with $S_0 \rightarrow S_{\text{ref}}$. For the R_1 of our reference tissue however, it is harder to define a standard deviation. In literature we found values between 1/260 and 1/300 so if we assume that these are the extremes and the R_1 has a Gaussian distribution we can say that if 95% of the R1 values of fat should be between 1/260 and 1/300 (approximately 2 standard deviations from the mean on either side) we can say that the standard deviation of R_{1r} is 1/10.

We now have a completely closed algebraic equation to estimate the uncertainty propagation of the concentration. However, we need to keep in mind this is an estimate. The linear approximation we use in the Taylor expansion is not completely valid as we are only using the first order terms. If we would like have a higher accuracy we could include higher order terms. There also might be some covariance between certain parameters, for example the flip angle and the noise at a certain spatial location, but these are difficult to determine and probably relatively small, so we decide to neglect them. Finally, the assumptions made on the spread of certain values (R_{1r} for example) might differ in other settings, by changing the values in these formulae these differences can be handled. Now that we have a complete framework for the conversion of data signal intensity to concentration lets have a look at how wel this toolbox performs on our clinical data.

3.3 Conversion of clinical data to concentration

In the previous chapter we saw that in the clinical data the low and high temporal resolution signal intensities did not match up (figure 2.6). Now lets have a look at 3 example data sets with different characteristics, shown in figures 3.4 and 3.5. What we can see is that when the data is discontinuous in signal intensities this difference is largely resolved when the data is represented as concentration versus time. The data sets that cause the most problems are the ones which have a large ratio in slice thickness in the coronal direction to spatial resolution in the sagittal direction. Difference as large as 4.4 millimeter to 1.5 millimeter cause problems because entire tissue parts can be missed and thus cannot be restored by interpolation. In addition, different tissues can be represented in one voxel, leading to differences in $R_1[0]$ and pharmacokinetic behavior. In future clinical scans this should be taken into account. To minimize the effect of this problem we look for areas with the same $R_1[0]$ between high and low temporal resolution within the area of enhancement to maximize the likelihood that we have the same tissue types. On average the concentration curves correspond quite nicely between low and high temporal resolution and curve shapes and heights correspond to the clinical description (the report on curve shape by the radiologist).

The error bars on the concentration are determined by the formulae (3.15 and 3.17) in section 3.2. In comparison to the standard deviation in the signal intensities the resulting concentration curves are adequate, the remaining error is lower than or close to 10%. Increasing the certainty in especially $R_1[0]$ could further decrease the standard deviation.

As mentioned before, the noise level of the original signal intensities only contribute about 2-4 % to the total uncertainty. We chose to discard the noise reduction algorithm (section 2.2) in this situation because the added uncertainty in the concentration curve caused by noise is rather low in addition to the fact that we would trade a known uncertainty for an unknown uncertainty caused by the blurring effect of the noise reduction filter. If the noise level would increase significantly however, one would still be able to use noise reduction schemes.

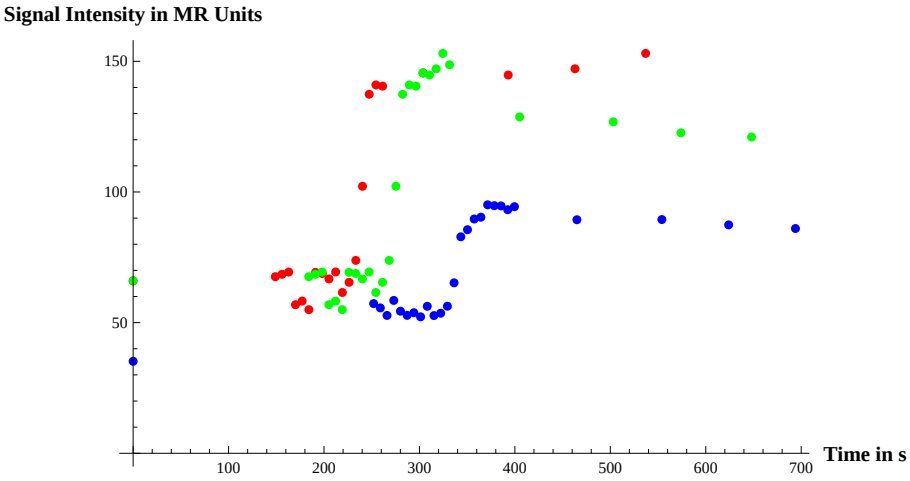

(a) Three signal vs time curves of patients 10 (blue), 441 (red) and 1185 (green)

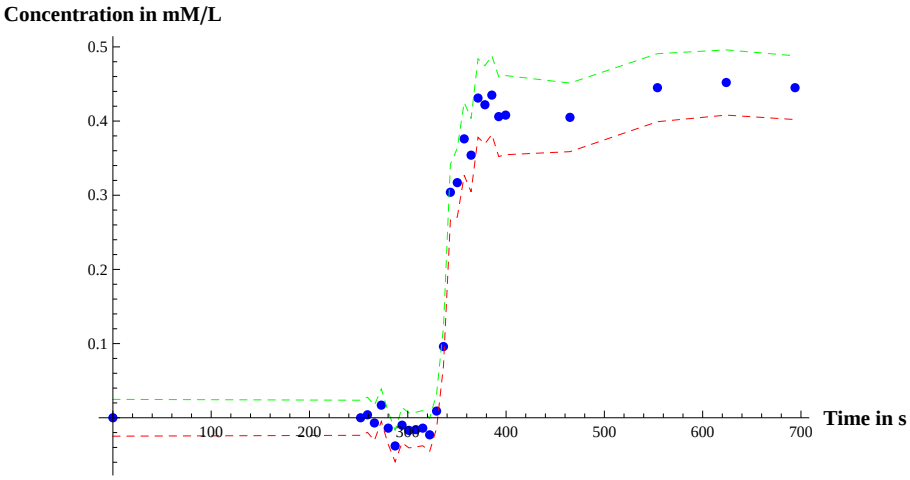

(b) Concentration vs time curve of patient 10

Figure 3.4: Signal vs time curves of three patients and concentration vs time of the lesion ROI of one patient, including a line plot of plus and minus one standard deviation

3.4 Conclusion

Concluding, we state that the use of an MRI signal model is valid in our clinical data. We gave an overview of the assumptions made in using this model, in addition to the estimation of the unknown parameters. Secondly, we estimated the effect of the neglecting of R_{2^*} and discarded its contribution to the signal model. Thirdly, we introduced an $R_1[0]$ estimation method which does not require any additional scanning, although further study into the effects of proton density on this estimation should be considered. Lastly we investigated a simplification of this method to remove repetition time and flip angle from the equation, which might allow more accurate calculation of the relaxation time because of flip angle inhomogeneity effects in the complete model. This is true in some cases, however, in our clinical scans this assumption would introduce additional errors and as there is no reason to choose for this simplification otherwise, we will use the complete model for the rest of this study.

We also derived a closed algebraic equation to approximate the error in concentration caused by all uncertainties in the signal model parameters, after which we used the model to calculate the concentration curves for our clinical data and can see that the average error in the high temporal

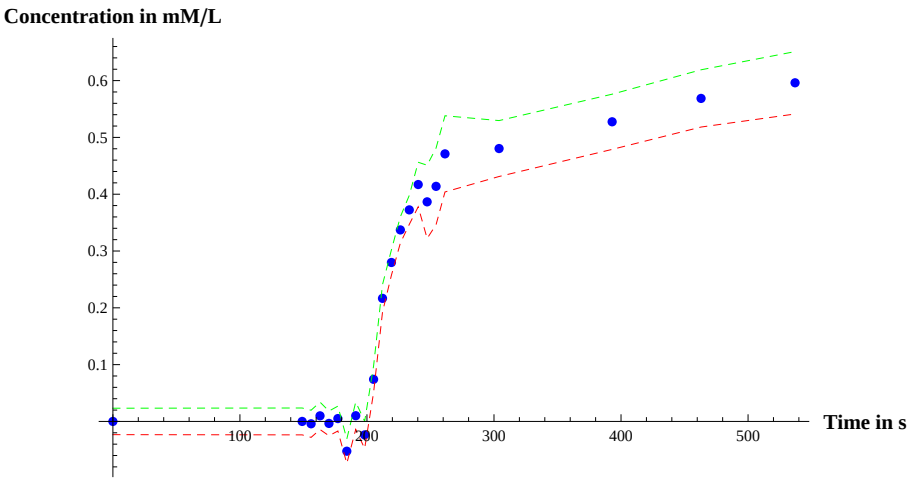

(a) Concentration vs time curve of patient 441

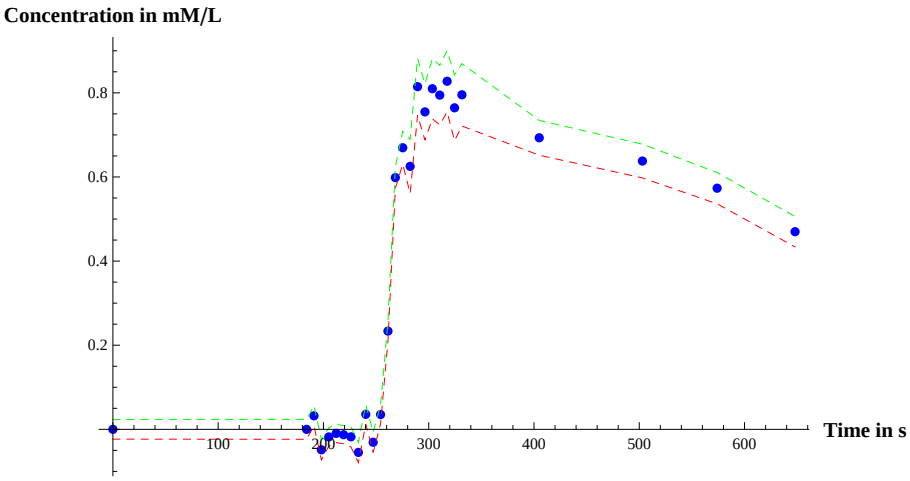

(b) Concentration vs time curve of patient 1185

Figure 3.5: Concentration vs time of the lesion ROI of two patients, including line plots of plus and minus one standard deviation

resolution part of the curves stays under the 10%, which is an adequate result.

Chapter 4

Pharmacokinetic modeling

To estimate underlying physiological parameters of tumor tissue we need an input-response model to relate the input (the arterial input function, or the concentration of the contrast agent in the arteries over time) to the output (the concentration in the tumor, estimated from the signal intensities, over time). To this end several pharmacokinetic models have been developed over time, each with its own limitations and possibilities. In this chapter we will derive the mathematics for these models from the simple mass balance and diffusion equations and investigate the useability of these models in a clinical setting using simulations.

4.1 Mathematical basis of the pharmacokinetic models

Pharmacokinetics is a modeling framework that describes the effect that the body has on the distribution of a drug, or in our case, a contrast agent. The kinetic behavior of a drug can be estimated using both non-compartmental and compartmental models, depending on what aspect you are interested in. Non-compartmental models are often used to estimate clearance rates and residence times of drugs and are based on area under the concentration curve calculations, which are measured from for example blood samples. However, we are interested in the physiological parameters of a certain tissue in the whole body, not in the response of the body as a whole. This is why we want to use a compartmental model, in which the system is split into different compartments which are interconnected with each other. A compartment can be defined as an amount or volume of material that is kinetically homogenous and well-mixed. Kinetically homogenous means that the kinetic behavior is the same within the compartment. The assumption of well-mixedness means that it does not matter where in the material we take the sample, the concentration is always the same. In the DCE MRI case, as we measure the concentration indirectly by signal intensity change caused by faster relaxation (T_1) of proton magnetization, this means that the protons affected are uniformly distributed through the tissue. In the DCE MRI case that is equal to the assumption that the exchange of water protons between the intracellular and extracellular, extravascular space is infinitely fast.

This requires some explanation. In DCE MRI we measure the signal intensity of a voxel. The composition of a tissue voxel is in general not homogenous, we can roughly divide a tissue voxel in three parts: the intracellular space, the extracellular, extravascular space (EES) and the vascular space. The intracellular space consist of the volume within the cells of the tissue, the vascular space consists of blood volume within the capillaries and the EES is the volume of the extracellular water. MRI contrast agents cannot enter the cell, so they are restricted to the EES and the blood. This means that without water proton exchange the contrast agent would only effect the water in the EES. If water exchange is infinitely fast it means that contrast agent has access to all tissue water. That means when we measure a voxel, which is thus the averaged signal intensity of those three spaces we can state that the compartments all behave the same. We will investigate that assumption further when we talk about the shutter speed model.

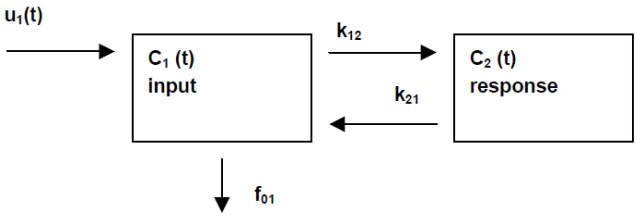

Figure 4.1: A basic two compartment model. We see the input u_1, the clearance f_{01} and the transfer constants k_{12} and k_{21} [12]

One of the most basic pharmacokinetic models is a simple two compartment model, as depicted in figure 4.1. As you can see there is an input, which is dependent on time, u[t], which is essentially the inflow of concentration in compartment one. Compartment one has a clearance term f, which is the permanent removal (through metabolism or excretion) of the drug/contrast agent. In addition there is exchange between compartment one and two, in which the flow from one to two is represented by the parameter k_{12} and k_{21} represents the reverse process. These can be different if the transport is facilitated in one direction and not in the other direction (membrane enzymes). The mass balance equations representing this system are:

$$V_{C_1}\frac{dC_1[t]}{dt} = u[t] - (k_{12} + f)C_1[t] + k_{21}C_2[t] \tag{4.1}$$
$$V_{C_2}\frac{dC_2[t]}{dt} = k_{12}C_1[t] - k_{21}C_2[t]$$

C_1	(mmol/L)	Concentration in compartment 1
C_2	(mmol/L)	Concentration in compartment 2
V_{C_1}	(L)	Volume of compartment 1
V_{C_2}	(L)	Volume of compartment 2
$u[t]$	(mmol/s)	Input function of contrast agent
f	(L/s)	Clearance term
k_{12}	(L/s)	Transfer rate of contrast agent from compartment 1 to 2
k_{21}	(L/s)	Transfer rate of contrast agent from compartment 2 to 1

If we try to fit our physiological system to this framework we would get three compartments, the input compartment being the arterial blood plasma in which the contrast agent is injected, the second compartment would be the capillary network in the tissue and the third would be the EES. We did not model the input compartment itself, because in this case we are not interested in for example excretion rates. We start modeling with C_p which is the concentration in arterial plasma. For the remaining two compartments we may write the following pair of mass balance equations, in which we assume that transport across the capillary membranes is not facilitated and thus that $k_{12} = k_{21}$. For two compartments which are in exchange with each other we can write:

$$V_c\frac{dC_c[t]}{dt} = F\left(C_p[t] - C_v[t]\right) - \mathrm{PS}\left(C_c[t] - C_t[t]\right) \tag{4.2}$$
$$V_t\frac{dC_t[t]}{dt} = PS\left(C_c[t] - C_t[t]\right)$$

C_p	(mmol/L)	Concentration in arterial blood plasma
C_v	(mmol/L)	Concentration in venous blood plasma
C_c	(mmol/L)	Concentration in capillary compartment
C_t	(mmol/L)	Concentration in tissue compartment
V_c	(L)	Volume of the capillary compartment
V_t	(L)	Volume of tissue compartment
F	(L/s)	Flow of arterial blood
PS	(L/s)	Permeability-surface area product

The first compartment was the arterial blood, the second the capillaries and the third the EES, so F is essentially k_{12} and k_{21} and PS is k_{23} and k_{32}. All pharmacokinetic models used in breast MRI are based on these basic formulae. However, there are different ways to solve them. The biggest challenge in these equation is the C_v term, as this is very difficult to measure using MRI. There are several ways however to remove this unknown from the equation. We will discuss the models by Tofts and Kermode[45] (based on the Kety[17] model for inert gasses), Brix[4] (based on the Morales and Smith[30] model for inert gasses) and the shutter speed model by Yankeelov, Springer et al.[60] in detail. We will also briefly look into the other well known models in this field, the Patlak[41], Larsson[22] and St. Lawrence and Lee[24] models.

4.1.1 Kety model

The approach used by Kety to solve this model is the basis of the standard Tofts and extended Tofts models. Kety essentially reduced the model to a one compartment model by using the assumption that the capillary fraction is so small ($< 5\%$) that the change in the mean tissue concentration during the time of passage of an element of blood is negligible. This is equivalent to the assumption that $V_c \frac{dC_c[t]}{dt} \approx 0$. This reduces equation 4.2 to:

$$0 = F\left(C_p[t] - C_v[t]\right) - \mathrm{PS}\left(C_c[t] - C_t[t]\right) \rightarrow F\left(C_p[t] - C_v[t]\right) = \mathrm{PS}\left(C_c[t] - C_t[t]\right)$$

$$\frac{V_t \frac{dC_t[t]}{dt}}{\mathrm{PS}} + C_t[t] = C_c[t] \tag{4.3}$$

Substituting the second equation into the first finally gives us:

$$V_t \frac{dC_t[t]}{dt} = F\left(C_p[t] - C_v[t]\right)$$

This reduces the model to one equation, but C_v is still a problem. However, we can now find a solution for $C_p[t] - C_v[t]$ using Ficks law of diffusion. Let's start from the the second law of diffusion equation[48]:

$$\delta Q_c[x,t] = Ps'\delta x\left(C_t[x,t] - C_c[x,t]\right)\delta t \tag{4.4}$$

δQ_c	(mmol)	Unit amount of contrast agent in capillary blood at a certain position x at time t
P	(L/(m^2s))	Permeability per unit area
s'	(m)	Surface area per unit length
δx	(m)	Unit length
$C_t[x,t]$	(mmol/L)	Concentration in the tissue at a certain position x along the capillary at a time t
$C_c[x,t]$	(mmol/L)	Concentration in the capillary at a certain position x at a time t
δt	(s)	Unit time

Now let us assume that $C_t[x,t]$ is approximately uniform for x=0 to x=L, were L is the length of the capillary. We can then write:

$$\delta Q_c[x,t] = \delta C_c[x,t]v'\delta x = \delta C_c[x,t]v'f\delta t = Ps'\delta x\left(C_t[t] - C_c[x,t]\right)\delta t \tag{4.5}$$

v'	(m^2)	Volume per unit length
f	(m^2)	Linear average velocity of the blood

We can rewrite this equation to:

$$\frac{\delta C_c[x,t]}{\delta x} = -\frac{Ps'}{v'f}\left(C_c[x,t] - C_t[t]\right) \tag{4.6}$$

And then solving this equation gives us:

$$C_c[x,t] - C_t[t] = Ae^{-\frac{Ps'}{v'f}x} \text{ where A is an integration constant} \tag{4.7}$$

Now we can further simplify the equation by using the boundary condition that at $x = 0 \rightarrow C_c[x,t] = C_p[t]$ and at $x = L \rightarrow C_c[x,t] = C_v[t]$:

$$C_c[0,t] - C_t[t] = C_p[t] - C_t[t] = A \tag{4.8}$$

$$C_c[L,t] - C_t[t] = C_v[t] - C_t[t] = \left(C_p[t] - C_t[t]\right)e^{-\frac{Ps'}{v'f}L} = \left(C_p[t] - C_t[t]\right)e^{-\frac{PS}{F}}$$

Now that we have this result we can extract an expression for $C_p - C_v$:

$$C_v[t] - C_t[t] = \left(C_p[t] - C_t[t]\right)e^{-\frac{PS}{F}} \tag{4.9}$$

$$\left(C_p[t] - C_t[t]\right) - \left(C_v[t] - C_t[t]\right) = -\left(C_p[t] - C_t[t]\right)e^{-\frac{PS}{F}} + \left(C_p[t] - C_t[t]\right) \tag{4.10}$$

$$C_p[t] - C_v[t] = \left(1 - e^{-\frac{PS}{F}}\right)\left(C_p[t] - C_t[t]\right) \tag{4.11}$$

And if we then add equation 4.11 together with equation 4.3 we get our final Kety model:

$$V_t\frac{\delta C_t[t]}{\delta t} = FE\left(C_p[t] - C_t[t]\right) \text{ where } E = 1 - e^{-\frac{PS}{F}}\text{, the extraction fraction} \tag{4.12}$$

However, Kety created this model for the transport of inert gasses throughout the body. To use this model for MRI contrast agents, we still need to add some extra constraints, which has been done by several researchers. The most used of these variants is the model proposed by Paul Tofts in 1993[45].

Tofts Model

The major difference between inert gas and Gd-DTPA and similar contrast agents is that Gd-DTPA does not uniformly distribute throughout the tissue but can only reach the extracellular, extravascular space (EES), which we will call C_e. This is the leakage space, which is the space which can be reached by the contrast agent from the blood plasma, the Kety equation changes to:

$$V_t\frac{\delta C_t[t]}{\delta t} = FE\left(C_p[t] - \frac{C_t[t]}{v_e}\right) \tag{4.13}$$

v_e () Extracellular, extravascular space volume fraction

This is because the concentration in the EES is larger than in the whole tissue, because the contrast agent does not distribute evenly. This means that the concentration gradient between C_p and C_t is smaller than with inert gas. This means we can state that the tissue concentration can be expressed as $C_t = v_eC_e$.

$$v_eV_t\frac{\delta C_e[t]}{\delta t} = FE\left(C_p[t] - C_e[t]\right) \tag{4.14}$$

Lastly, Tofts also expresses his parameters per unit mass. This introduces the tissue mass to the equation M_t:

$$v_eV_t\frac{\delta C_e[t]}{\delta t} = FE\left(C_p[t] - C_e[t]\right)M_t$$

$$v_e\frac{\delta C_e[t]}{\delta t} = FE\left(C_p[t] - C_e[t]\right)\frac{M_t}{V_t}$$

$$v_e\frac{\delta C_e[t]}{\delta t} = FE\rho\left(C_p[t] - C_e[t]\right)$$

We then define the following two parameters $K_{\text{trans}} = FE\rho$ and $k_{\text{ep}} = \frac{K_{\text{trans}}}{v_e}$. We can distinguish three different situations in which these two variables have different meanings, namely the flow limited situation, the permeability limited situation and the mixed situation:

Flow limited In this case the flow F is small compared to the permeability PS. In that case the extraction fraction $E \approx 1$ and thus $K_{\text{trans}} = F\rho$. This essentially means that K_{trans} is now a measure of blood flow to the tissue. This situation is probably never true in tissue, although there are no experiments to confirm this. In tumor tissue the permeability does increase but this is accompanied by an increase in blood flow too.

Permeability limited In this case the F is large compared to PS. In that case we can use a Taylor expansion of E to get $E = \frac{PS}{F} \rightarrow K_{\text{Trans}} = PS\rho$. This is the situation that Tofts for example uses in MS brain lesions. In tumor tissue this might be invalid, as permeability is increased compared to the normal situation.

Mixed And of course we also have the situation in which both flow and permeability play a part, which is essentially the most realistic one. It does remove the ability to independently estimate flow or permeability from a single measurement. If additional flow measurements are done in an experiment, one would then be able to get a real permeability and flow measure.

Now to look at our final differential equation, using $k_{ep} = \frac{K_{\text{trans}}}{v_e}$:

$$\frac{\delta C_e[t]}{\delta t} = k_{\text{ep}} \left(C_p[t] - C_e[t] \right) \tag{4.15}$$

The solving steps are detailed in appendix C; the solution to this equation is:

$$C_t[t] = K_{\text{trans}} \int_0^t e^{-k_{\text{ep}}(t-s)} C_p[s] ds \tag{4.16}$$

This final equation is the basic form of the Tofts model. Tofts himself used it mainly for MS brain lesions but moved to breast cancer MRI later on. However an important difference between the two is that in cancer the vascularity is usually increased, which reduces the chance the original assumption made by Kety that the capillary compartiment is negligibly small is true. To this end an extended version of the Tofts model was later introduced

Extended Tofts Model

The extended version of the Tofts model includes the plasma fraction as a direct throughput of $C_p[t]$:

$$C_t[t] = K_{\text{trans}} \int_0^t e^{-k_{\text{ep}}(t-s)} C_p[s] ds + v_p C_p[t] \tag{4.17}$$

$$v_p \quad () \quad \text{Plasma fraction}$$

However, in equation 4.3 we stated that the volumes of the capillaries, which is essentially the same as the plasma volume, is negligible. We need a different assumption to allow this model to still be true, which is a step that is often overseen. What we want is an assumption which leads to $C_p = C_c$ (this also decouples the equations). The solution can actually be found in the assumption that the system is permeability limited. If this is the case we might state that the change in C_c is only due to the inflow from C_p and not due to to the outflow. This means that the equation are decoupled and that $C_c[t]$ will follow $C_p[t]$. The higher the flow, the better this approximation. However, this also means that K_{trans} is only a measure of permeability.

If we would not use this assumption the use of the extended model seems invalid, as the assumption of C_p as input function will likely overestimate the input function. This might also be solved if we can find a more localized input function, which we will discuss in more detail in chapter 5.

4.1.2 Morales and Smith model

Another approach, which was developed at approximately the same time as Kety's model, was postulated by Morales and Smith. They stated that there is a constant fraction between $C_p - C_v$ and $C_p - C_c$ so that $C_p[t] - C_v[t] = \frac{1}{r}(C_p[t] - C_c[t])$. This means that if r is 1 $C_c = C_v$ and if r is 0 $C_c = C_p$, everything else is in between those values. You can see r as a sort of slope of the concentration gradient, it weights which of C_p or C_v has the biggest influence on the value of C_c. This reduces the basic model equations to:

$$\begin{aligned} V_c \frac{dC_c[t]}{dt} &= \frac{F}{r}(C_p[t] - C_c[t]) - \mathrm{PS}(C_c[t] - C_t[t]) \\ V_t \frac{dC_t[t]}{dt} &= PS(C_c[t] - C_t[t]) \end{aligned} \tag{4.18}$$

These equations are coupled differential equations, which have no analytical solution. This is probably why the Kety model has been the model of choice for many years. However, since we entered the computer era, it is very well possible to calculate these equations numerically. The use of this model on breast MRI was first done by Brix in 2004[4]. There is little knowledge on the value of r however, or if it even is a scalar value. To our knowledge no research has been done on this subject. We however have no knowledge about the correctness of assuming r has a scalar value. It might very well be a more complex function, but as far as we know, no research has been done into this assumption.

Brix model

Brix essentially uses the above equations to estimate the tissue concentration. He does however express them with respect to C_e, because the leakage space of Gd-DTPA only consists of the EES, which is equivalent to the adaption Tofts did to the Kety model. The model used by Brix can then be written as:

$$\begin{aligned} V_c \frac{dC_c[t]}{dt} &= \frac{F}{r}(C_p[t] - C_c[t]) - \mathrm{PS}(C_c[t] - C_e[t]) \\ V_e \frac{dC_e[t]}{dt} &= PS(C_c[t] - C_e[t]) \\ C_t &= v_p C_p + v_e C_e \end{aligned} \tag{4.19}$$

We altered these equations slightly to enable comparison between this model and the models by Tofts (equation 4.20). First we will express the variables per unit mass and then will use the assumption that V_c is V_p and the substitutions $V_c = v_p V_t$ and $V_e = v_e V_t$. This will result in these final equations:

$$\begin{aligned} v_p \frac{dC_c[t]}{dt} &= \frac{F\rho}{r}(C_p[t] - C_c[t]) - PS\rho(C_c[t] - C_e[t]) \\ v_e \frac{dC_e[t]}{dt} &= PS\rho(C_c[t] - C_e[t]) \\ C_t &= v_p C_p + v_e C_e \end{aligned} \tag{4.20}$$

This is one of the most complete pharmacokinetic models available for MRI. However, these extra parameters (F, v_p) also add more requirements to your data, and if the data is not up to par, the fitting procedure will probably fail.

Another aspect which we have not included up to now is the fact that our pharmacokinetic models are using the assumption that our compartments are well-mixed. However, at high contrast agent concentrations that may not be the case. The reason for this is that we assume that our contrast agent has the same effect on all the water within a voxel. However, we already know that our contrast agent can only reach the water in the EES directly. The rest of the water in a voxel should reach the contrast agent via exchange of water between compartments. If we assume that

this is infinitely fast, our assumption of well-mixedness holds. Of course, in reality, this is not the case, although the exchange is rather fast. In high concentrations of contrast agent however, not all contrast agent may have effect on all the water. This effect has been implemented in the shutter speed model.

4.1.3 Shutter Speed Model

In essence this method states that in a voxel we can no longer use the linear relation between relaxation rate and concentration of contrast agent (Eq. 3.2), due to the fact that the exchange between intracellular and EES water is not infinitely fast. This means that we get two different R_1 times in voxel, of which the population ratio is determined by the reaction rate of $|H_2O|_i \rightleftharpoons |H_2O|_e$. We can extend this to exchange between protons in blood, EES and intracellular space as follows $|H_2O|_i \rightleftharpoons |H_2O|_e \rightleftharpoons |H_2O|_b$ in which we assume that there is no direct exchange between blood and intracellular space.

The former water exchange equation forms the basis for the first generation shutter speed model and the latter forms the basis for the second generation shutter speed model. We will start with the derivation of the first generation model:

First generation

Let's have a look at the equation of restoration of the longitudinal magnetization after a 90°pulse:

$$M_z = M_0 \left(1 - e^{\frac{-t}{T_1}}\right) \rightarrow 1 - \frac{M_z}{M_0} = e^{\frac{-t}{T_1}} \tag{4.21}$$

If we then write this for two different populations within one voxel we can state that:

$$1 - \frac{M_z}{M_0} = a_L e^{-tR_{1_L}} + a_S e^{-tR_{1_S}}, \text{ where } (a_S + a_L) = 1 \text{ and } R_1 = \frac{1}{T_1} \tag{4.22}$$

M_z	(T)	Longitudinal magnetization
M_0	(T)	Longitudinal magnetization at time 0
a_L	()	Fraction of protons with large relaxation rate
a_S	()	Fraction of protons with small relaxation rate
R_{1_L}	(s^{-1})	Smaller relaxation rate (larger T_1)
R_{1_S}	(s^{-1})	Larger relaxation rate (smaller T_1)

We now need to find an expression for R_{1_L} and R_{1_S}, we start from the modified Bloch equations for two site exchange. The full derivation can be found in appendix C. We can neglect a_S due to the fact that concentration in a clinical setting almost never reaches a value where a_S becomes significant.[60]

This derivation proces reduces the final equation for the relaxation rate R_1 to:

$$\begin{aligned} R_{1_L} =& \frac{1}{2}\left(C_t[t]r_1 + R_{1_i}[0] + \frac{R_1[0] - (1-p_e)\,R_{1_i}[0]}{p_e} + \frac{1}{\tau_i} + \frac{1-p_e}{p_e\tau_i}\right) - \\ & \frac{1}{2}\sqrt{\left(-C_t[t]r_1 + R_{1_i}[0] - \frac{R_1[0] - (1-p_e)\,R_{1_i}[0]}{p_e} + \frac{1}{\tau_i} - \frac{1-p_e}{p_e\tau_i}\right)^2 + \frac{4\,(1-p_e)}{p_e\tau_i^2}} \end{aligned} \tag{4.23}$$

Here the subscripts i and e are intracellular and EES respectively. For the C_t term we can input a pharmacokinetic model. In this case we have to choose for the basic Tofts model. This is because the first generation shutter speed assumes that that the vascular fraction is so small that we can neglect the exchange of water proton between the vascular space and the EES.

In addition, we cannot fit the shutter speed part of the model and the pharmacokinetic part separately because $v_e = f_w p_e$ were f_w is the fraction of tissue space that is able to interact with aqueous solutes, so they both have a v_e dependency. We will assume for the rest of this study that all water in the EES is reachable by the contrast agent and thus that $p_e = v_e$. That gives us three parameters to fit in the final model, K_{trans} , v_e and τ_i.

Second generation

The second generation of the shutter speed model includes a vascular term, both in the exchange and pharmacokinetic parts of the model. For the equations of this model we will refer the reader to the paper by Li et al.[26]

The physiological meaning of this model is that the exchange between blood water protons and EES protons is not infinitely fast. This means that the contrast agent in the plasma does not have access to all the tissue water, thus if this effect is neglected it will lead to an overestimation of the influence of C_p on the total relaxation rate of the tissue. The pharmacokinetic model used in this variant is the extended Tofts model.

This extension adds extra variables to the model (v_p and τ_e, where the latter refers to the mean transit time of a water proton from the blood to the EES), however, the inclusion of the blood water exchange with the EES water only has a significant effect in tissues with a really low K_{trans} (in the order of 10^{-5}), which is unrealistic even in normal tissue[58;60]. This extension is usually only useful in certain brain lesions where K_{trans} can be extremely low due to the blood-brain barrier. That is why we decided to not incorporate these extra parameters and keep using the first generation shutter speed model.

It might be possible in future research to look into combining the first generation shutter speed model with for example the Brix model to create a sort of 'ultimate' model which incorporates both flow, permeability and shutter-speed in one model.

4.1.4 Other models

There are also several other models which are common in literature, for example the model by Larsson, the adiabatic solution of the tissue homogeneity model by St. Lawrence and Lee[24] and the model by Patlak[41]. We will briefly introduce these models and explain why they were not included in this investigation.

Larsson Model

The model by Larsson was developed around the same time as Tofts developed his model and was at first mostly different in the way they estimated the arterial input function. However, over time the predefined biexponential AIFs were replaced by specific input functions (population averaged or patient specific), which actually meant that the Tofts model and Larsson model are the same, except the parameters are slightly different as Larson expresses them per 100 grams of tissue.

Mathematically his model is:

$$C_t[t] = K_i \int_0^t e^{-\frac{K_i}{\lambda}(t-s)} C_p[s] ds \tag{4.24}$$

Where $\frac{K_i}{\lambda}$ is equal to k_{ep}. Here λ is similar in nature to v_e but also includes a conversion from mMol/ml to mMol/100 grams. However, in his original paper[22] he seemed to be fitting his model to mMol/mL curves, which essentially makes his model equivalent to that of Tofts. In addition, a slight error of units occurs in his original paper as he writes the concentration of arterial blood as mMol/L and it should be mMol/mL (or change the tissue concentration to mMol/L). As his model is essentially the same as the Tofts model, it has no additional advantages.

St. Lawrence and Lee Model

In 1998 St. Lawrence and Lee published a solution to equation 4.2 using an adiabatic approximation. He stated (for brain tissues) that the change of concentration in blood is much higher than the change in the concentration in the tissue and that we thus could express C_t as a discrete time step function. This essentially means that during a time dt in which C_c changes, C_t would remain constant. The full mathematical workout is quite extensive and can be found in his original

	Standard Tofts	Extended Tofts	Shutter Speed Model	Brix Model
Parameters	K_{trans} , v_e	K_{trans} , v_e, v_p	K_{trans} , v_e, τ_i	F, K_{trans} , v_e, v_p
Assumptions	$v_p \approx 0$, $F \gg 0$, $\tau_i \approx 0$	$F \gg 1$ min^{-1}, $\tau_i \approx 0$	$v_p \approx 0$, $F \gg 0$	$\tau_i \approx 0$

Table 4.1: Model overview

paper[24]. This assumption leads to the following equation:

$$C_t[t] = F \int_0^{\tau} C_p[t-u]du + K_{\text{trans}} \int_{\tau}^{t} C_p[u] e^{-\frac{K_{\text{trans}}}{v_e}(t-u-\tau)} du \tag{4.25}$$

τ (s) Mean Capillary Transit Time

This essentially states that during the capillary transit time the tissue concentration is completely described by C_p and that after that time diffusion start to play a role.

This model was originally developed for diffusion in the brain, in which, due to the blood brain barrier diffusion is often low. In this case the adiabatic assumption seems a valid one. However, in cancer it is typical that the vessels are leaky and thus that diffusion is a lot faster, which means that the adiabatic assumption might not hold. In addition, this model contains the same terms as the model postulated by Brix (F, K_{trans} and v_e, v_p is replaced by τ). The fact that the assumptions in this model are questionable in breast cancer made us choose for the Brix model.

Patlak Model

The last model we will talk about is the model developed by Patlak and only includes k_{ep} and v_p. This model states that in the beginning of the curve there is no significant flux back into the vascular compartment. The equation for this model is:

$$C_t = k_{\text{ep}} \int_0^{t} C_p[\tau]d\tau + v_p C_p[t] \tag{4.26}$$

This model can be used for fitting the initial rise of the curves to estimate k_{ep} and v_p. This is why these types of models are known as 'first pass models', as they essentially only model the first pass of the bolus. As we have data up to 5 minutes, we choose not to use this model because it does not allow separate estimation of K_{trans} and v_e, which we are able to do using the Tofts models.

Thus four models remain for further evaluation, the standard and extended Tofts models, the shutter-speed model and the Brix model, a summary is given in table 4.1.

Before looking into simulations and model performance we will first research the possible need for pre-fitting of the data.

4.2 Pre-fitting data with an empirical model

Before fitting our data with the pharmacokinetic models, which we implemented in Wolfram Mathematica[54], we investigated the use of an empirical model to fit the data. This might reduce fitting problems in the other fitting process due to noise and differences in temporal resolution. The advantage of using an empirical model is that in addition to the fact that we solve the temporal resolution problem is that we have an analytical function, which makes the calculations of the models easier. The empirical mathematical model (EMM) we used for this study has been developed by Fan et al[11]. The equation to this model is:

$$C_t[t] = A(1-e^{-\alpha t})^q e^{-\beta t} \frac{1+e^{-\gamma t}}{2} \tag{4.27}$$

The fitting of this model generally gives good results using it together with the standard Tofts model. The EMM is more robust to the differences in temporal resolution and noise, probably because it has a more restricted shape. We simulated a curve using the standard Tofts model with a K_{trans} and v_e of .5 min^{-1} and .3 respectively and undersampled it and added noise (the concentration uncertainty). The exact steps that were taken are detailed later in this chapter (subsection 4.3.1). The results of the fitting on a simulated curve can be seen in figure 4.2. All fitting in this report has been done using the Nelder Mead (Simplex) method [34]. However, these

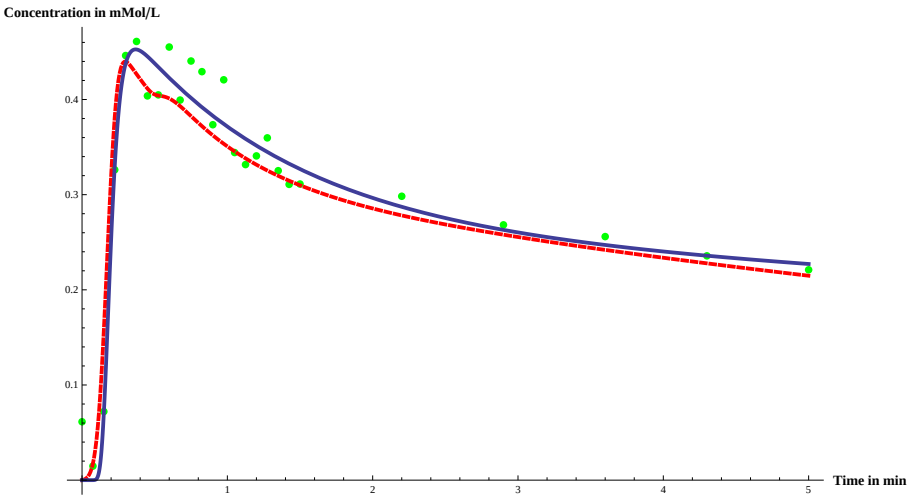

Figure 4.2: The green dots are the original simulated data belonging to a tumor with $K_{\text{trans}} = .5$ and v_e=.3. The red dashed line belongs to the direct fit of the standard Tofts model, which corresponds to an estimate of .47 and .29 for K_{trans} and v_e respectively. The blue line is the model fit after a prefitting with the EMM, which results in a better estimate .501 and .309 for K_{trans} and v_e

restriction in shape also have a huge drawback. The EMM cannot fit certain curve shapes, for example with high K_{trans} and low v_e or low K_{trans} and low v_e, as shown in figure 4.3. This the reason why we did not use this method, as this requires visual inspection of each fit to make sure that the EMM fit represents the true data adequately. In addition, this method is not able to fit subtle difference which occur when we use more complicated models (extended Tofts, Brix).

4.3 Model of choice: ideal data

4.3.1 General simulation framework

In this chapter we will use simulations to test certain models, so we will introduce a general simulation framework in this subsection. To simulate data we need several parts. First we need a method to solve our models.

For the Tofts and extended Tofts models there are two ways to solve them explicitly. We can use the Fourier or Laplace transforms to calculate the convolution or we could solve the convolution numerically. We choose to solve them numerically, because it is actually faster than using the Laplace and Fourier transforms. For the Brix model we need to solve the differential equations numerically, for which we used an explicit Runge/Kutta solving method [43]. Lastly, for the shutter speed model we will also calculate the convolution of the pharmacokinetic part numerically. Our models also require an input function. For the simulations an input function from literature would be good enough. In the case of real patient data the acquisition of the input function is not that trivial, but we will look into that in chapter 5. We will use the AIF developed by Parker [40], which

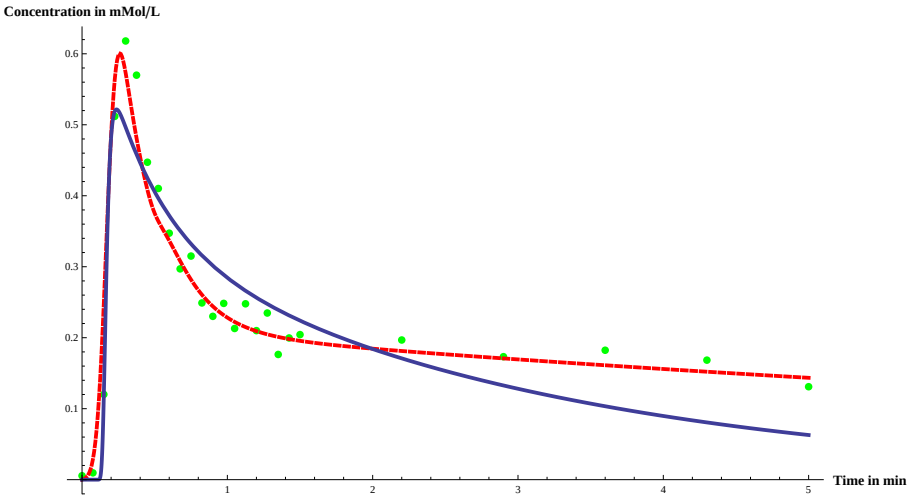

(a) Tissue with K_{trans} and v_e of .95 and .3 respectively, the Tofts fit corresponds to .79 and .2 respectively, the EMM (after Tofts fit) to .67 and .18

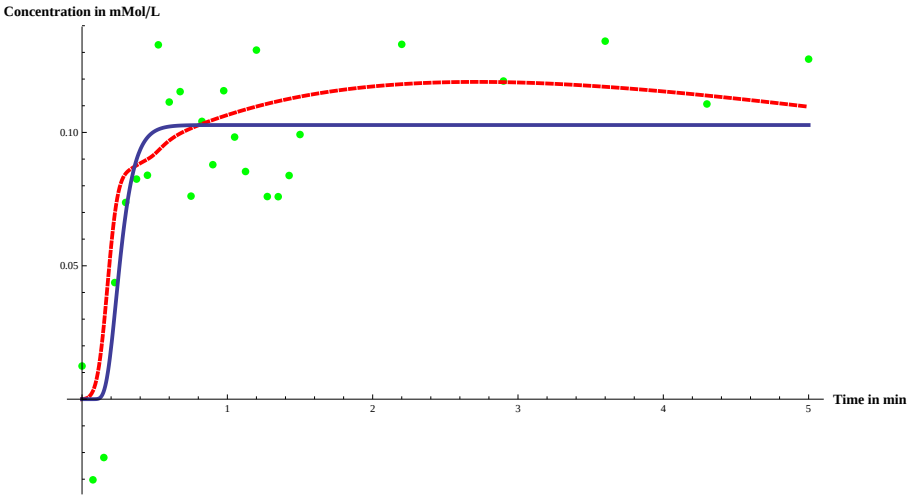

(b) Tissue with K_{trans} and v_e of .07 and .14 respectively, the Tofts fit corresponds to .068 and .13 respectively, the EMM (after Tofts fit) to .077 and .15

Figure 4.3: Two simulated tumors were fitted with the Tofts model, the green dots represent the original data, the red line the Tofts fitted data and the blue the EMM prefitted data

has been adapted by Yang et al.[57] to give the following equation:

$$C_b[t] = 7.5527e^{\frac{-(t-.171)^2}{.00605}} + 1.003e^{\frac{-(t-.364)^2}{.035912}} + \frac{1.064e^{(-.083t)}}{1+e^{-37.772(t-.482)}} \tag{4.28}$$

We can manipulate the height of the first pass (essentially a representative of the bolus injection), which corresponds to an increase in blood flow and the amount of contrast agent injected, by changing the 7.5527 in this equation. Parker has already shown in his article that the first pass peak is the most variable characteristic of a patient and additionally that a change in this peak has no to little influence on the rest of the curve. An example of this AIF using several values for first pass height is shown in figure 4.4 We do need to remember that these are the concentrations of the whole blood. As the contrast agent only spreads throughout the plasma we need to calculate the plasma fraction using the percentage of blood that consists of red blood cells, the hematocrit value. This value is between .36 and .46 in women and is also dependent on the location in the blood vessel structure, it is higher in large vessels and lower in small vessels. In this AIF we will

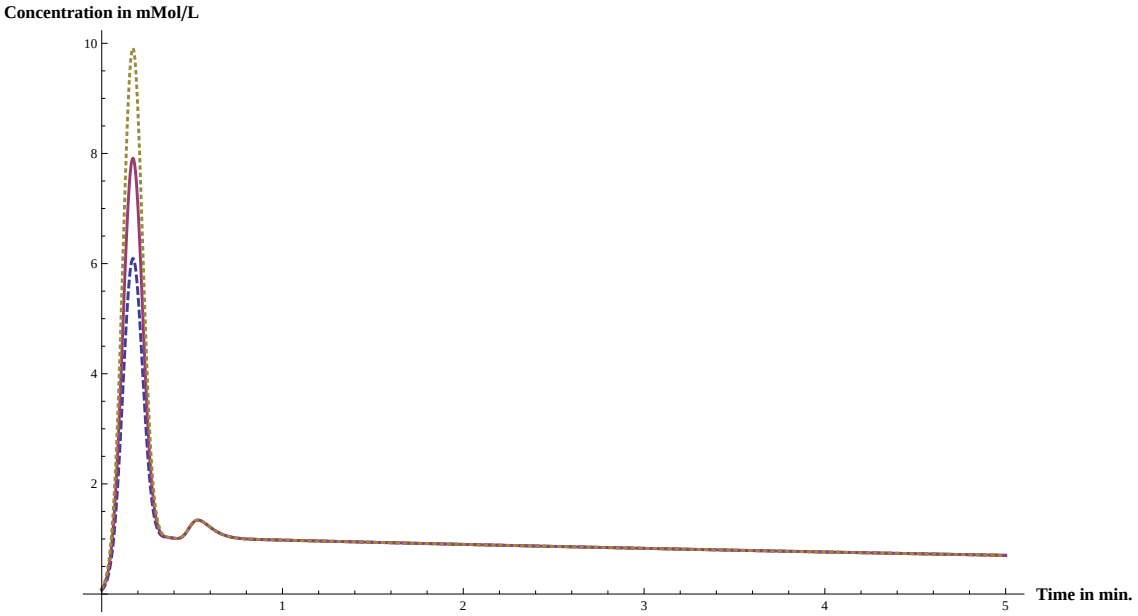

Figure 4.4: Examples of the Parker AIF using different first pass heights

use the value Parker himself used, which is .42 [40]. This means for C_p we write:

$$C_p[t] = \frac{C_b[t]}{1 - HCt}$$

Now that we have a way to solve our model and have an input function we can generate tissue response curves. In the last parts of this chapter we will also simulate clinical data. The clinical data in our setup can be characterized by a certain temporal resolution in combination with a certain level of noise. The temporal resolution differs in the first part and the last part of the curves, as does the noise level. Using the noise level in the images and the other uncertainties we can calculate the uncertainty in the concentration curves, as we already covered in chapter 3. The uncertainties in the high-temporal resolution parts are usually around 8 to 9 % and in the low temporal resolution around the 4 to 5 %.

This means we can add uncertainties manually using a Gaussian distribution. We assumed a Gaussian distribution of the other uncertainties and a concatenation of Gaussian distributions leads to a Gaussian distribution. This means we can add noise to our ideal data to reduce the quality to that of clinical data.

In addition we also need to undersample the data. There are several ways to do this, the easiest one being just picking points at a larger time step. The resolution in our data is that we usually have around 20 frames in the first 90 seconds of measurements, which means one frame for every 4.5 seconds. In the low temporal resolution we have a timestep of around 45 seconds with in total 4 frames. Our ideal data has a time step of .5 seconds, which means that we could undersample by just selecting one time point out of every 9 timepoints. However, if we look at how MRI scanners collect images this would be equivalent to assuming that each frame would be collected instantaneously, which of course is not true. MRI scanners continuously fill the imaging (k) space. As we do not have k-space data which we could undersample, we do the next best thing. We assume that after a certain time point the scanner starts filling k-space until we are at the next frame. If we convert this to the undersampling of the concentration curve this process would go as followed, at time 0 we start by summing all the points up till frame 1, which is at time = 4.5 s. At time 4.5 we would take the mean of those points and assign that value to that time point. This method has been used by other researchers and is a quite reasonable approximation

to the real situation in MRI scanners[59]. The low temporal part of the curve is undersampled the same way as the high temporal part. The 3.5 minutes after the first 1.5 have 4 equidistant time points.

Now we can create simulated clinical data by first creating an ideal tissue response curve using the process used for the ideal data. After we have this response curve we first undersample it using the method described above to the temporal resolution of clinical data and after that we will add noise uncertainty to these points using randomly selected values from a Gaussian distribution with a standard deviation comparable to clinical data. This results in a simulated clinical data curve.

4.3.2 Model equivalency with specific assumptions

If we look at the derivation of our models in this chapter, we see that they are all derived from the same basic equation. If this is correct our implementations of these models should reduce to each other if we choose specific assumptions.

If we have a look at the behavior of the models when using different assumptions, essentially different values of F, v_p and τ_i. First lets look at how the Tofts, extended Tofts and Brix behave when we use different values for F and v_p while keeping K_{trans} , v_e and the AIF constant in figure 4.5. As you can see when we reduce v_p the extended and standard Tofts models are actually

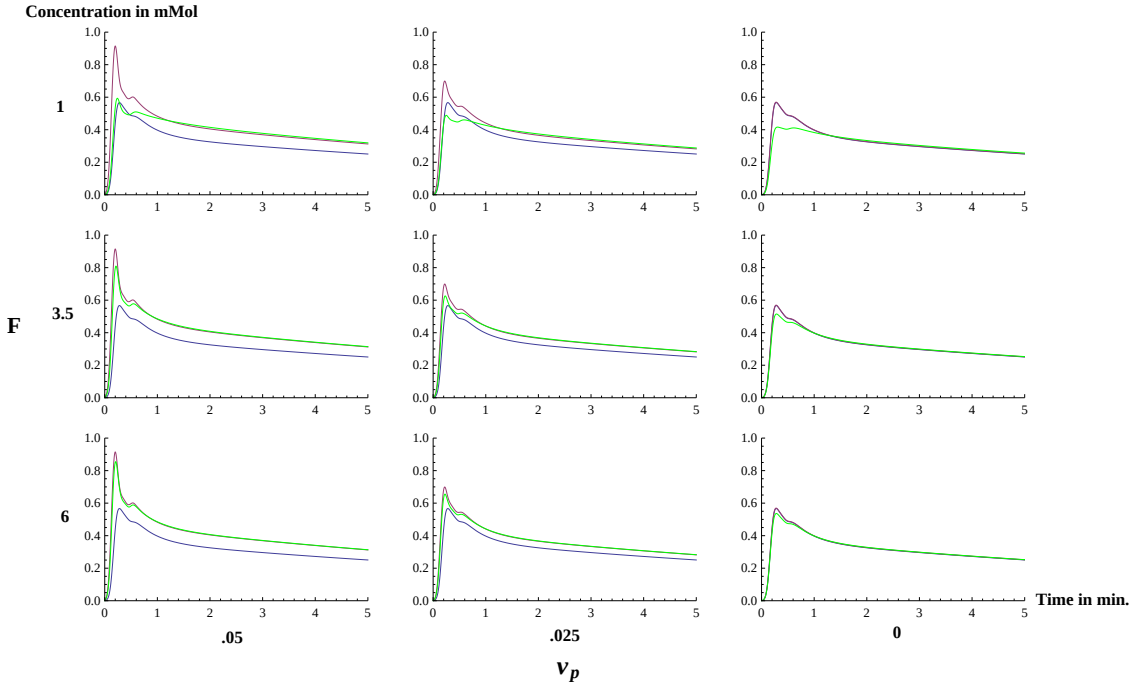

Figure 4.5: Different models outputs for $K_{\text{trans}} = .5$ and $v_e = .2$ with differing v_p and F. The blue line represents the standard Tofts model (K_{trans} and v_e), the purple line the extended Tofts model (K_{trans} , v_e and v_p) and the green line the Brix model (K_{trans} , v_e, v_p,and F)

equivalent and when we then increase F, the Brix model is also equivalent. This essentially means that when we can assume certain things (v_p approaches 0, F is large) about our data we can use simpler models. For example, in tissue where we expect a reasonable blood flow and low plasma fractions we might be just as well off using the standard model compared to the Brix model, the extra parameters F and v_p can only cause problems in that case, for example worse fitting performance.

Looking at the shutter speed model, it was stated that when τ_i approaches zero the linear relationship between contrast agent and relaxation rate is valid. Our model implementations

confirm this, as can be seen in figure 4.6. Now that we know that the models can actually give

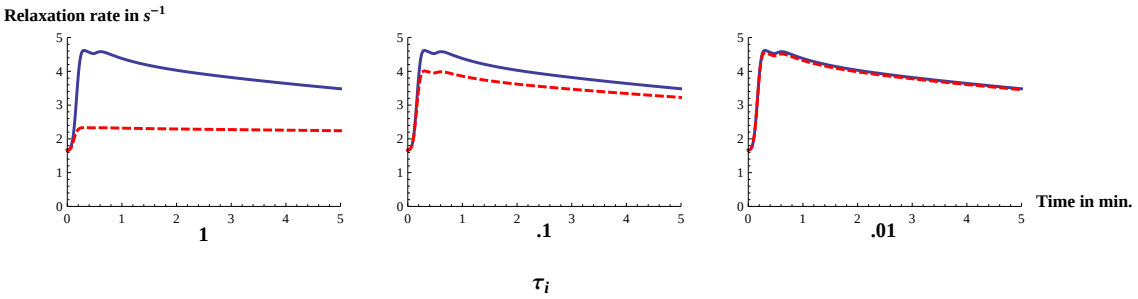

Figure 4.6: Different models outputs for $K_{\text{trans}} = .5$ and $v_e = .2$ with differing τ_i, the blue solid line corresponds to the standard Tofts model (K_{trans} and v_e), the red dashed line to the shutter speed model (K_{trans} , v_e and τ_i)

the same tissue response functions when we reach certain parameter values we can ask ourselves if some parameters are even calculable if we just have data. In other words, is there a large correlation between parameters are we able to find individual parameters from the data? We first have a look at the sensitivity functions of the parameters, which is a qualitative way of assessing parameter correlation. Using the sensitivity functions we can also calculate a correlation matrix, which shows if it might be difficult to assess parameters quantitatively.

4.3.3 Sensitivity functions and correlation matrices

We will look at the most complete model (Brix) for this analysis. First let us introduce the sensitivity function:

$$S_i = \frac{\delta C_t}{\delta p_i} \tag{4.29}$$

Here p_i is the i^{th} parameter giving the S_i of that parameter. In the case of the Brix model $i = 4$, were we will use 1=F, 2=K_{trans} , 3=v_p and 4=v_e. As the sensitivity functions are hard to calculate for the Brix model, we will use a Forward Euler Approximation [15] of the sensitivity function. As the sensitivity function can change due to a change in variables (for example if K_{trans} changes value, it's sensitivity function can change due to the influence of the other parameters on the curve), it is useful to remember that these are indications and by no means exact measures. We will plot the sensitivity functions corresponding to $F = 2$, $K_{\text{trans}} = .75$, $v_p = .05$ and $v_e = .3$ as an illustration of the relative effects of these parameters in figure 4.7. These curves show the effective

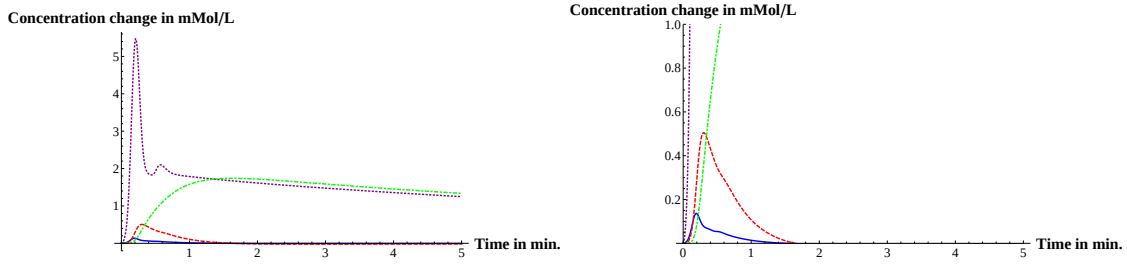

(a) Sensitivity functions of the Brix model

(b) Zooming in on the F and K_{trans} contributions

Figure 4.7: Sensitivity functions of the Brix model, F is solid blue, K_{trans} is dashed red, v_e is dashdotted green and v_p is dotted purple. These function show the change in Ct when we have a unit change in each parameter. This means that v_p is by far the most sensitive parameter and F the least sensitive

of a unit change in each parameter. It might be more illustrative to look at the contributions of

each element in a real setting. So let's take a look at the behavior of the parameters when we have a real tissue response. In figure 4.8 there is a plot when $F = 2$, $K_{\text{trans}} = .75$, $v_p = .05$ and $v_e = .3$. As you can see the contributions of F, K_{trans} and v_p are in the same range, which might cause

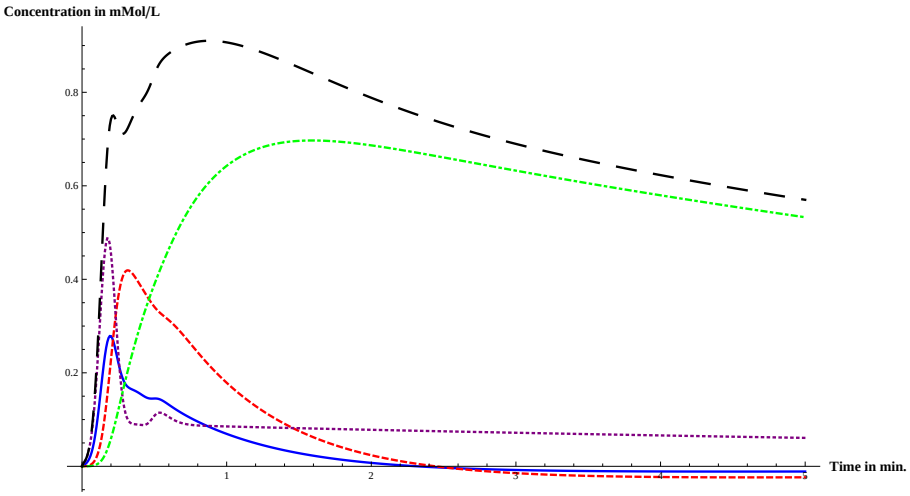

Figure 4.8: Sensitivity functions and the tissue response, F is solid blue, K_{trans} is dashed red, v_e is dashdotted green and v_p is dotted purple. The black line dashed line is the complete tissue response, which is also the sum of the sensitivity functions. This illustrates the contribution of each parameter to the complete tissue response

trouble distinguishing them individually. To see this numerically we can calculate a covariance matrix. From the sensitivity functions we can create this matrix using the following formula:

$$\text{COV} = \sigma^2(F^T F)^{-1}, F_{ij} = \text{SF}_i[j] \tag{4.30}$$

Inspection of this matrix yields that most uncertainty is contained in the parameter F, which has a negative covariance with K_{trans} and v_p meaning an underestimation in F will lead to an overestimation of K_{trans} and v_p. The rest of the correlations are positive, meaning an overestimation in a parameter leads to an overestimation in another parameter. Removing F from the matrix (reducing it to a covariance matrix of the extended Tofts model) shows a negative covariance between v_p and K_{trans} and between v_p and v_e, which means we expect underestimation of v_p creates overestimation in K_{trans} and in v_e. In the standard Tofts model we see a small negative covariance between K_{trans} and v_e which means a relatively large overestimation of K_{trans} would result in a small underestimation of v_e.

We did not derive the sensitivity functions for the shutter speed model and thus we do not go into that in this report, but we know from the paper by Yankeelov et al.[60] that underestimation of τ_i leads to underestimation of K_{trans} and v_e.

Now that we have some basic hypotheses about what we would expect from our models, we wanted to investigate if all the model could be fitted when we would have perfect data. To this end we will use Monte Carlo based simulations.

4.3.4 Model performance with simulated ideal data: Monte Carlo Simulations

First we look at 'ideal' data, which means data with a very high sampling rate (2 Hz) for MRI and no noise, using Monte Carlo Simulations. The basis of this technique is that we will randomly select pharmacokinetic parameters and use an AIF to generate a tissue response function. Then, given this AIF and tissue response function, we will look if our solving mechanism can extract the correct parameters. The Monte Carlo method is suited for this problem because we want to

estimate the behavior of the model independent of the parameters we would choose, we want to study the ability to find biasses or inherent faults independent of parameter value.

Monte Carlo setup

Firstly, we need a domain to select the pharmacokinetic parameters from. For K_{trans} and v_e there are several researchers which have studied the ranges of these parameters in breast cancer [42;10]. In our simulations we will use K_{trans} values ranging from 0 to 1.5 min^{-1} and v_e values ranging from .1 to .6. For v_p the situation is a little more difficult as the number of researchers using the extended Tofts model is smaller than the number of researchers using the standard model. However, for v_p we also found a range of $0 < v_p \leq 0.2$ [7], were the latter is quite high. Lastly, for F and τ_i the only references we have are the papers of Brix [4] and Yankeelov/Springer [60], so deciding on a range for these parameters was the most difficult. The maximum values for F found by Brix were in the range of 4.3 min^{-1}, assuming a K_{trans} of 1.5 min^{-1}. So we take 6 min^{-1} as the maximum value and 1 min^{-1} as minimum value. For τ_i we take a range between 0 and 1.5 s^{-1}, the value used by Yankeelov/Springer et al. is usually around 1. The maximum values found were 1.5 s^{-1} in a rat glioma [60].

We decided to assume a rectangular distribution within these ranges, which means that when randomly selecting, every value has the same chance of being picked. The reason for this is that there is no to little knowledge if some values of parameters are more likely than other values, or that certain combinations are impossible. This is why we assumed that every value has an equal chance of being selected.

We would also like to know if the model is robust to different AIF shapes. To this end we decided to differ the bolus height with a factor between .5 and 1.5, which is reasonable in clinical situations [40] and additionally used a convolution with a gamma-variate function [56] to create different AIF widths. The formula used for the gamma variate function is:

$$GV[t] = \frac{1}{\Gamma[\alpha]\beta^{\alpha}} t^{\alpha-1} e^{\frac{-t}{\beta}} \tag{4.31}$$

Here we vary α and β to get different spreads. We choose a random value between 1 and 5 for α and .01 and .05 for β. These values were determined empirically to still give realistic results. An example of the effect of this function is shown in figure 4.9. We now have our tools to start our Monte Carlo simulations, but we use a different sampling method for the selection of the parameter values to reduce the number of simulations we need to get a representative results. This method is called Latin Hypercube Sampling.

Latin Hypercube Sampling

The basis for Latin Hypercube Sampling is that we divide the probability distribution of each parameter in N parts, where N is the number of simulations we wish to perform. Then we randomly select one of those parts and select a value within that part randomly. Then this part is marked as 'visited' and we select a value using the same procedure for another parameter. At the next iteration we select a part, which has not been selected before and then continue as before until we are out of parts. The difference between this method and the regular method is shown in figure 4.10. This method makes sure we visit the entire range of a parameter, thus allowing for fewer iterations to get a complete overview. This method could also be extended to the entire parameter space at once instead of using it iteratively for each parameter, however to sample that entire range we would require several thousands of iterations, which could not be done in this study. We decided to choose 500 iterations.

The step-by-step process then is:

1. Create an AIF using the literature AIF by Parker convolved with a randomly adapted gamma variate function

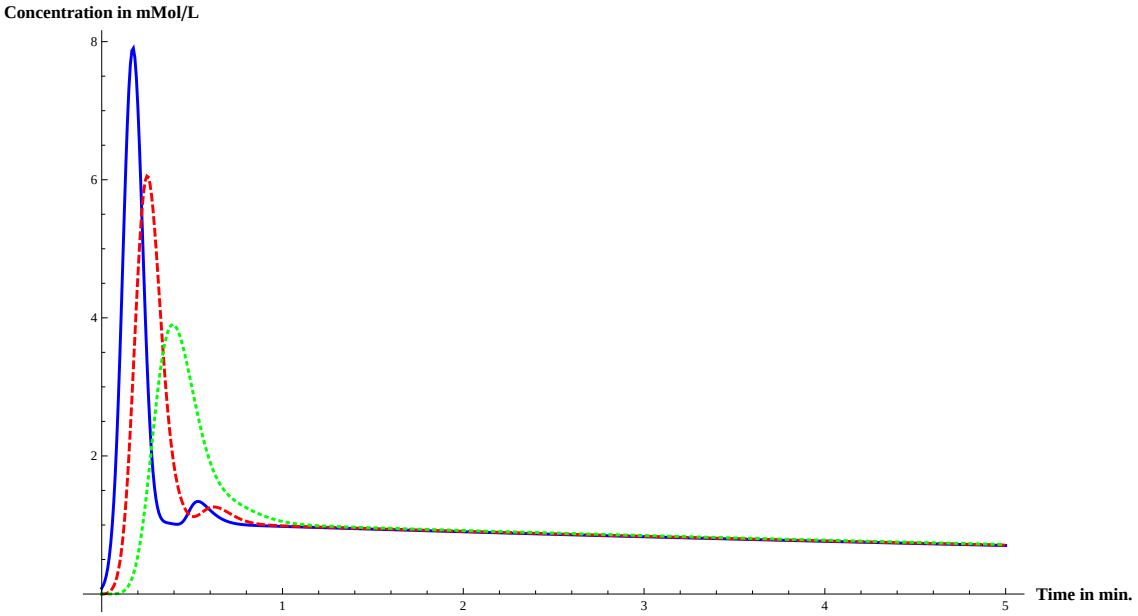

Figure 4.9: Different input functions using a convolution with a gamma-variate function. Blue is the original Parker input function, red is using $\alpha = 3$ and $\beta = .03$ and green is using $\alpha = 5$ and $\beta = .05$

2. Create a tissue response curve using pharmacokinetic values randomly selected using Latin Hypercube Sampling
3. Try to fit the model using the input AIF and store fitting results. The fitting algorithm used is the Nelder-Mead (Simplex) global optimization technique[34]
4. Go back to step one until we have done 500 iterations

We then implemented the Monte Carlo Simulations for each model and looked at the behavior with ideal data.

Results: Standard Tofts Model

First let us have a look at the standard Tofts model, which only considers K_{trans} and v_e effects. To estimate the succes of fitting we will define an error measure. The error measure we will use is:

$$\text{Error} = 100\frac{P_i^{\text{Ori}} - P_i^{\text{Fit}}}{P_i^{\text{Ori}}} \tag{4.32}$$

Here P_i is the i^{th} pharmacokinetic parameter. This expresses the error of the fit as percentage difference between the original value and the fitted value. We can then plot a histogram of the error over the simulations per parameter and show them together. In addition it also insightful to plot the fitted value and the real value as a scatter plot to detect certain value dependent effects.

For all models we would expect almost perfect fits with small errors and no bias when using these 'ideal' data. It could however be possible that a model is overparameterized and that it is not possible to identify the individual parameters even from 'perfect' data. If that is the case in one of our models, we can immediately conclude that the model is not suited to be used on clinical data. Firstly we will look at the standard Tofts model.

The results for the standard model using ideal data is shown in figure 4.11. As can be seen in the figures, the fitting procedure using ideal data results in almost perfect fits, with errors in the parameters around .1 percent. Also there is no apparent bias in the parameter estimates. This is what we would expect, the model has identifiable parameters and the fitting procedure is stable.

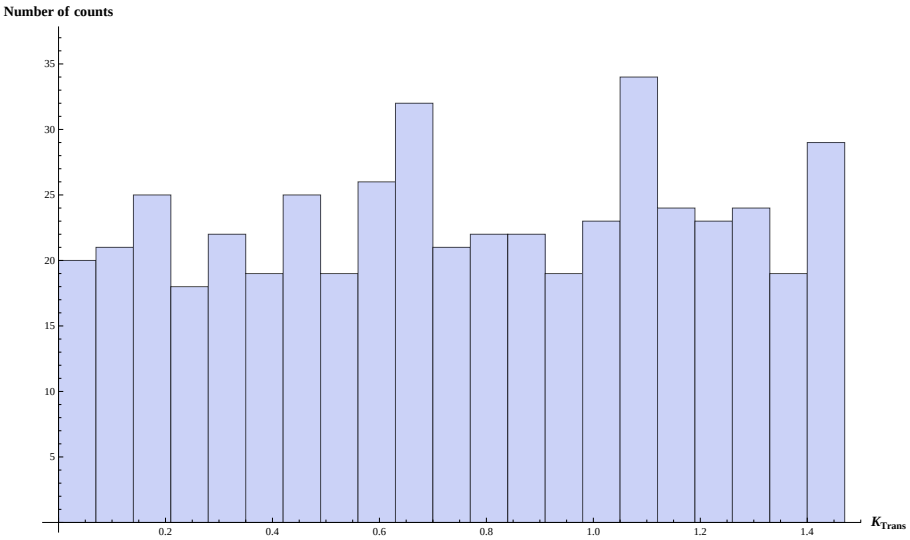

(a) Histogram of a regular sampling procedure of 500 K_{trans} values

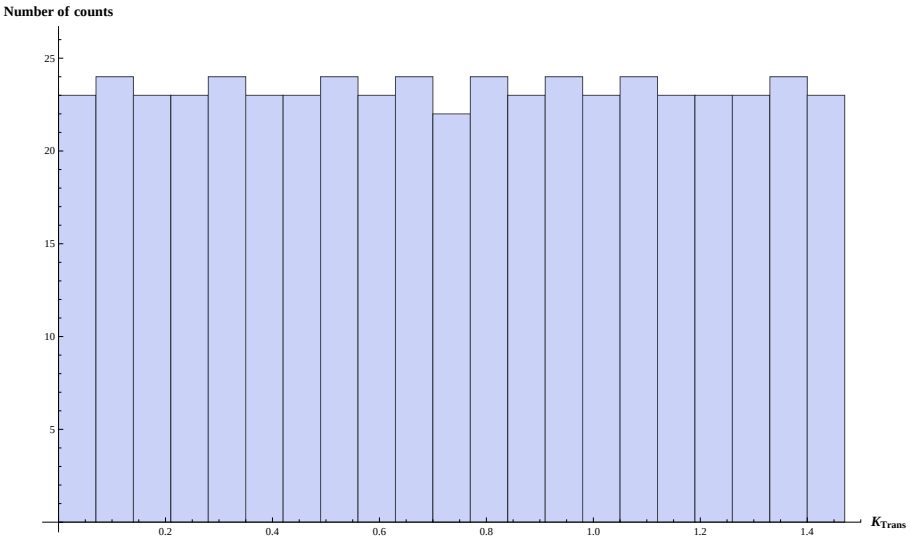

(b) Histogram of a the Latin Hypercube sampling for 500 K_{trans} values

Figure 4.10: Differences between regular sampling and Latin Hypercube Sampling in Monte Carlo Simulations

Results: Extended Tofts Model

Now let us have a look at the extended Tofts model and see if we get similar results, which are shown in figure 4.12. We can see here that it is slightly more difficult to get good estimates, the fitting procedure sometimes finds a local minimum instead of the global minimum. This can be solved by visual inspection of the fits, or a more rigorous fitting procedure, for example simulated annealing. However, more rigorous procedures and visual inspection require more user interaction and time and that is generally not wanted. Looking at the overall picture, the fits still seem very good with by far the largest portion fitting quite nicely. The errors are also for the most part in the range of .1 to .2 % for approximately 470 of the 500 fits. There seems to be a little bias in parameter estimates of v_e, which seem to be underestimated when fitted incorrectly. There is no clear reason for why this is, however we can see that this only occurs in cases were there is a clear fit failure. Inspection of those data points show that these effects usually occur when

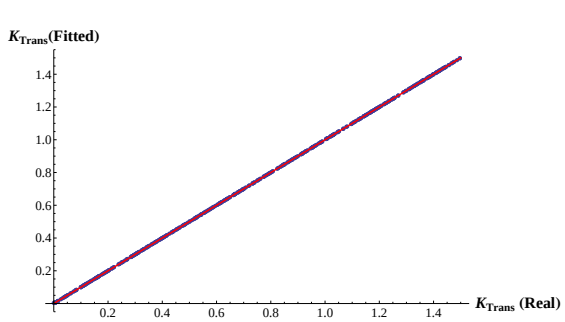

(a) Scatter plot of K_{trans} values, the red line corresponds to real K_{trans} = fitted K_{trans}

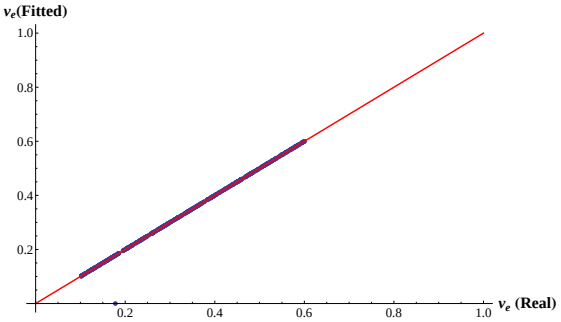

(b) Scatter plot of v_e values, the red line corresponds to real v_e = fitted v_e

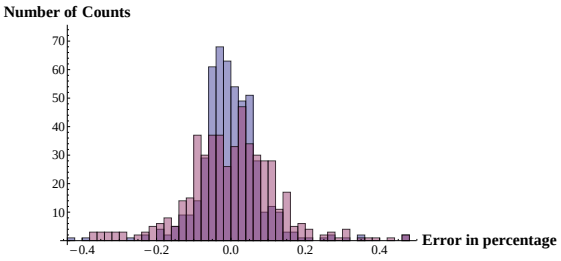

(c) Histogram of the error for K_{trans} (blue bars) and v_e (purple bars) in percentage

Figure 4.11: Scatter plots and the histogram for fitted parameters using the standard Tofts model with ideal data

K_{trans} approaches .001. The model then can't find K_{trans} and usually overestimates it's value, which results in underestimation of v_e and v_p, the underestimated points of v_e also correspond to underestimated points in v_p. However, it also sometimes fits really low K_{trans} values correctly, so this is not a limitation of the model. However, extremely low K_{trans} values may require some extra inspection after the fit.

Results: Shutter Speed Model

The results of the shutter speed model when used with ideal data are shown in figure 4.13. For the shutter speed model we see that there is some overestimation of τ_i, which seems to be a harder parameter to fit compared to for example v_p. On average the fits are still quite good, with approximately 360 fits within the .1% error margin for τ_i. As expected the overestimation in τ_i also leads to overestimation in the other parameters. It seems that this has more effect on v_e than on K_{trans} , which indicates that τ_i has a larger effect on the second part of the curve. To be certain of a correct fit, we suggest visual inspection of the fit afterwards.

Results: Brix Model

Lastly we will inspect the results of the Brix model, which is shown in figure 4.14. We can see that the value of F is hard to fit, even when data is perfect. We already saw this effect in the sensitivity function as F has a very similar shape to K_{trans} but has a lower effect, which makes it hard to distinguish as an individual parameter. If we inspect the fits of the other variables when F is fitted poorly, we see in our data that a mean error of 15% only leads to errors of .3% in K_{trans} and v_e and to errors of 3% in v_p. This raises the question how important F is in clinical situations in tumor tissues.

Two other effects are seen in the data, K_{trans} has a higher uncertainty at high values. This is because the tissue response is then flow limited, meaning that F becomes a more important

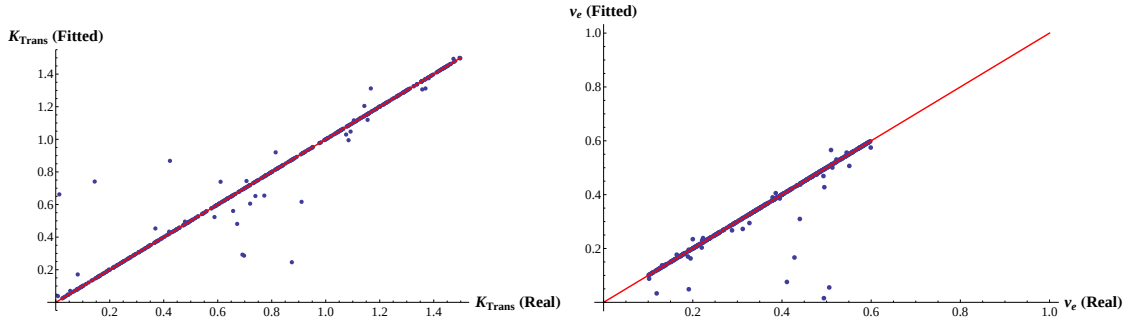

(a) Scatter plot of K_{trans} values, the red line corresponds to real K_{trans} = fitted K_{trans}

(b) Scatter plot of v_e values, the red line corresponds to real v_e = fitted v_e

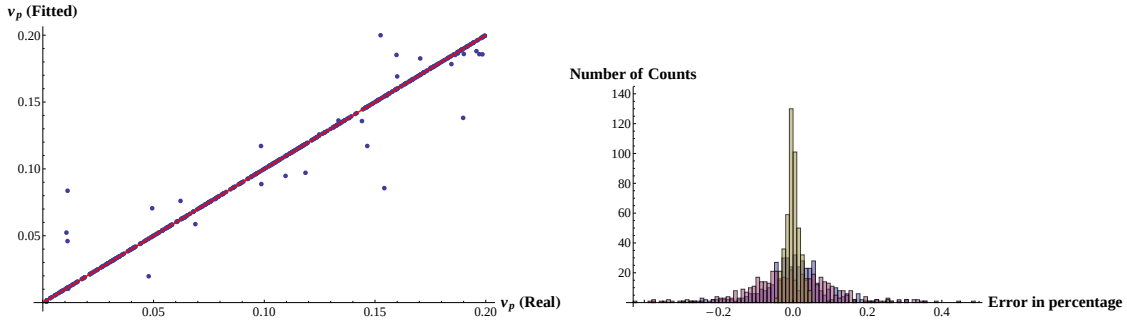

(c) Scatter plot of v_p values, the red line corresponds to real v_p = fitted v_p

(d) Histogram of the error for K_{trans} (blue bars), v_e (purple bars) and v_p (brown bars) in percentage

Figure 4.12: Scatter plots and the histogram for fitted parameters using the extended Tofts model with ideal data

parameter. In these cases it is easier to determine F than K_{trans} . You would also see this effect in the curve of F when we would extend the range towards zero, however those values are physiologically unrealistic.

The last effect we can see is that there is a bias in the errors in v_p which are dependent on the value of v_p. We have no real explanation for this but when we observe the behavior of the sensitivity functions we can see that v_p and F become more alike when v_p gets larger and that F becomes more important in general. That means that for small v_p it could be that during the fitting the effects of F are not attributed to F, but to v_p, overestimating v_p. As v_p increases, the importance of F increases. At a certain point v_p effects may be introduced into F leading to an underestimation of v_p. We might state that in general this model should be used in cases were we expect very little flow (F < 1) or were permeability is extremely high ($K_{\text{trans}} > 1.5$). In those cases F becomes an important factor and it may play a substantial role, however, at the moment it's effect seems negligible.

Now that we know what to expect from ideal data, let's have look at how the models perform when we simulate clinical data, which is done to assess the usefulness of the models in a real clinical setting.

4.4 Model of choice: clinical data

Monte Carlo setup

The Monte Carlo simulations are done in the same way we did them with ideal data with additional undersampling and noise addition steps. After that process we try to fit the model to this curve using the ideal input function. This is thus a sort of forward-backward approach, creating a curve

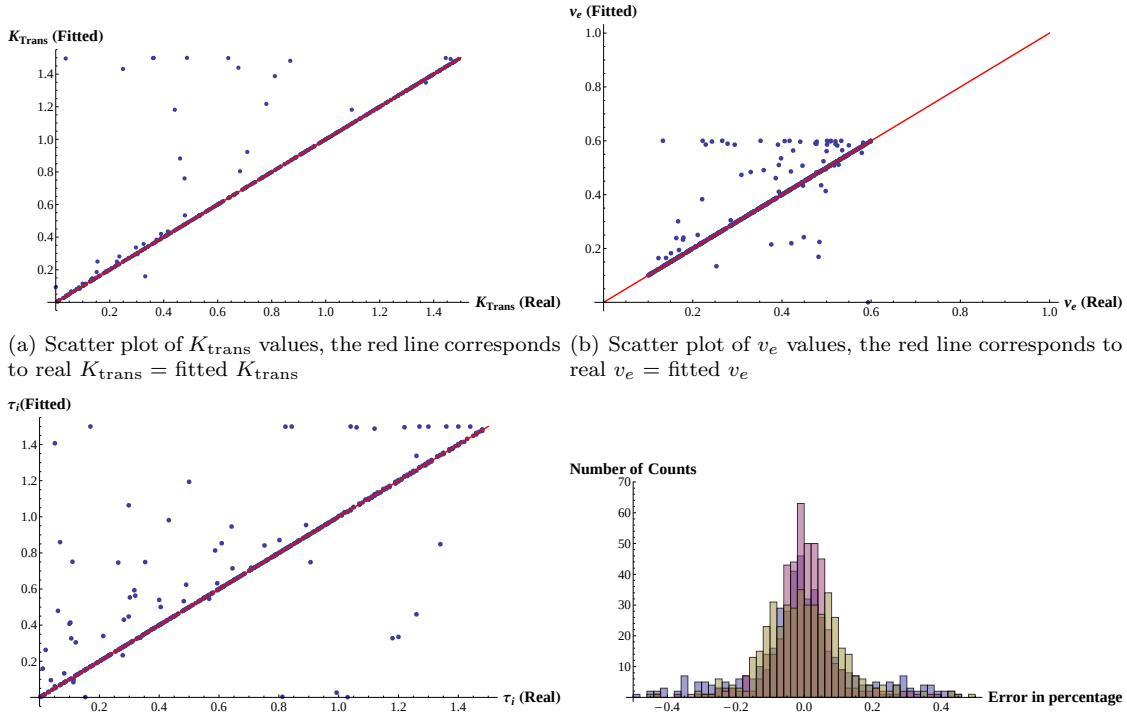

(a) Scatter plot of K_{trans} values, the red line corresponds to real K_{trans} = fitted K_{trans}

(b) Scatter plot of v_e values, the red line corresponds to real v_e = fitted v_e

(c) Scatter plot of τ_i values, the red line corresponds to real τ_i = fitted τ_i

(d) Histogram of the error for K_{trans} (blue bars), v_e (purple bars) and τ_i (brown bars) in percentage

Figure 4.13: Scatter plots and the histogram for fitted parameters using the shutter speed model with ideal data

using a model, undersampling that curve, adding uncertainties and than trying to fit that curve with the same model. The effects of non-ideal input functions will be discussed in chapter 5. We also did 500 simulations for each model. The results will show that not every model can handle these situations.

4.4.1 Model performance with simulated clinical data: Monte Carlo Simulations

Results: Standard Tofts Model

Let us first have a look at the results of the standard Tofts model, which are shown in figure 4.15. Remember that the errors in this models are in addition to the errors we make by neglecting F, v_p andτ_i, which we will research in subsection 4.4.3. The simulated curves are thus generated with the same model they are fitted with, the only difference is that the simulated curves are undersampled and uncertainties ('noise') are added. The results we can see in these graphs are what we would expect. First let's look at K_{trans} . We see that in larger values of K_{trans} a small bias seems to appear. This is because due to the undersampling we miss the exact peak of enhancement and as a higher K_{trans} increases the steepness of the initial slope, the higher K_{trans} the higher the risk of missing the peak and the higher the part we miss. If we miss the peak the fitting procedure will underestimate K_{trans} , which is the behavior we see in both the curve (4.15a) and the histogram (4.15c). On average, if we can not assume anything about K_{trans} , we could do a bias subtraction of around 7%. The spread in the error can be attributed to both the noise and the fact that higher K_{trans} values have a higher bias and lower have a lower bias.

Secondly, if we look at v_e we see a smaller, opposite effect. The high values of v_e seem to have a little overestimation on average. This bias is caused by the fact that the underestimation of

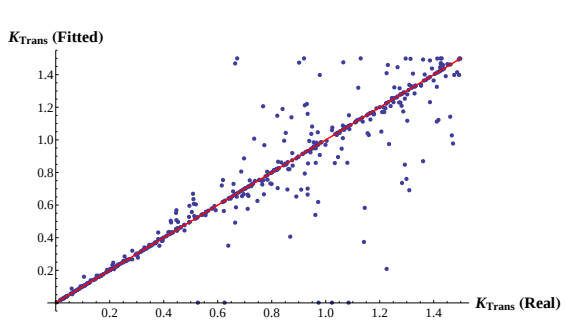

(a) Scatter plot of K_{trans} values, the red line corresponds to real K_{trans} = fitted K_{trans}

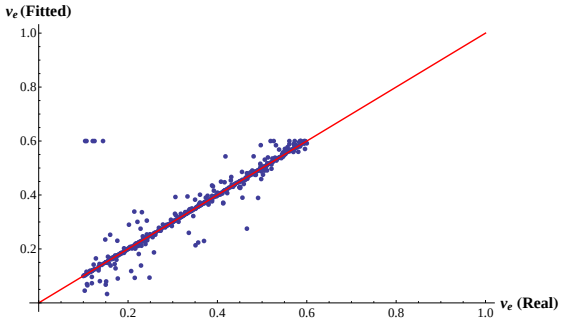

(b) Scatter plot of v_e values, the red line corresponds to real v_e = fitted v_e

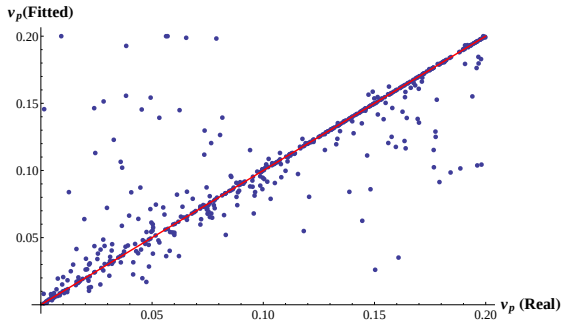

(c) Scatter plot of v_p values, the red line corresponds to real v_p = fitted v_p

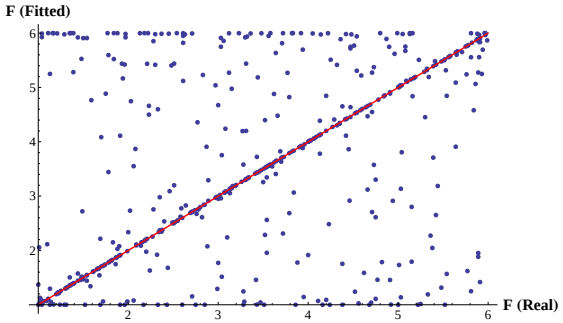

(d) Scatter plot of F values, the red line corresponds to real F = fitted F

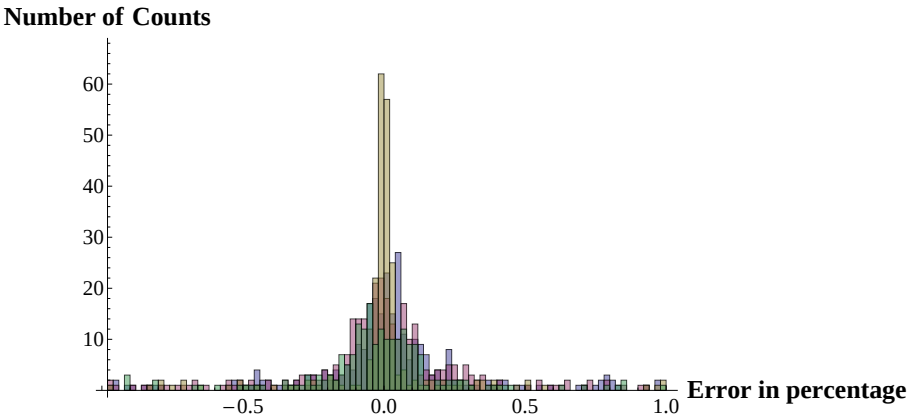

(e) Histogram of the error for K_{trans} (blue bars), v_e (purple bars), v_p (brown bars) and F (green bars) in percentage

Figure 4.14: Scatter plots and the histogram for fitted parameters using the Brix model with ideal data

the peak leads to the need for a higher v_e to still get the same low temporal part of the curve. If we underestimate K_{trans} on average, this will results in an overestimation of v_e. This effect is larger for large values of v_e because those often correspond to a quicker wash-out and when we have a quick wash out the undersampling will lead to an underestimation of that effect due to the averaging. Now if we compare the histograms of K_{trans} and v_e we see that K_{trans} has a much broader distribution than v_e. This is caused by the fact that v_e in general is a more stable parameter, because it corresponds mostly to the lower frequency effects in the tissue response curve. Thus the undersampling has less influence on that parameter than it has on K_{trans} .

In general we can say that this model is well suited for the fitting of clinical data, assuming that F, v_p and τ_i are negligible. The behavior for the range of parameters is predictable and

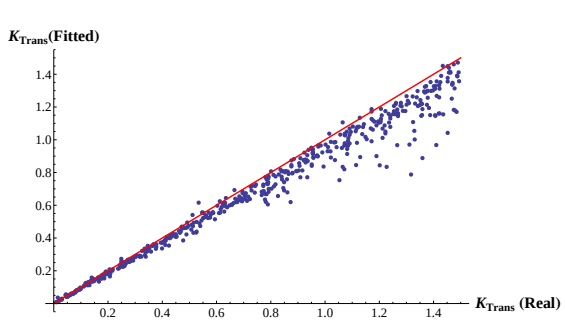

(a) Scatter plot of K_{trans} values, the red line corresponds to real K_{trans} = fitted K_{trans}

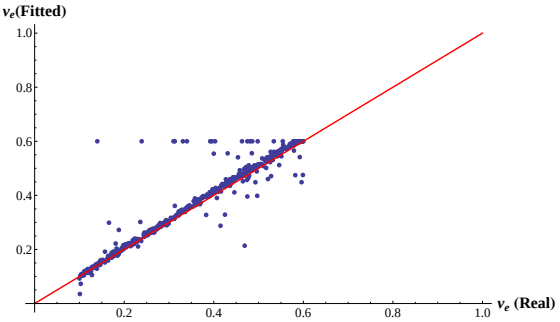

(b) Scatter plot of v_e values, the red line corresponds to real v_e = fitted v_e

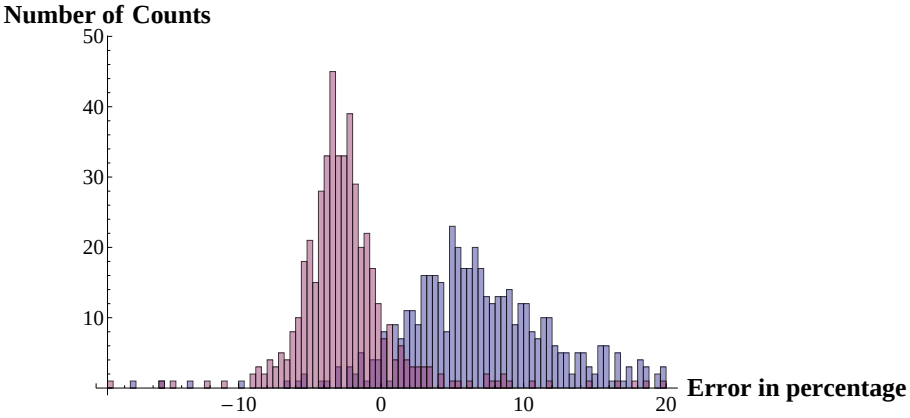

(c) Histogram of the error for K_{trans} (blue bars) and v_e (purple bars) in percentage

Figure 4.15: Scatter plots and the histogram for fitted parameters using the standard Tofts model with simulated clinical data

robust in the case of this simulated clinical data, meaning that we usually have a good fit of the data and that the effect of undersampling is clear.

Results: Extended Tofts Model

If we then move on to the extended model we get the following results, depicted in figure 4.16. Let's first look at the results of the parameter that has the most deviation, which is v_p. We already saw that the contribution of v_p is throughout the whole tissue response, but that the biggest contribution of its sensitivity function are in the initial enhancement. v_p is also the parameter which has the highest steepness in its sensitivity function, making it more prone to the temporal undersampling. We can also see this in the curves (4.16c), the underestimation of v_p is apparent throughout all values. In the lower range v_p is sometimes neglected by the fitting procedures, assigning the lower bound value to v_p. This happens because the contribution of v_p is so small it can not be estimated individually from the few time points we have.

The problems in estimating v_p give a different kind of graph for K_{trans} compared to the standard model. In the standard model K_{trans} was underestimated, in the extended model it is overestimated. This is because due to the underestimation of v_p the effects occurring due to v_p are attributed to K_{trans} by the model fitting procedure. This bias increases for higher K_{trans} values because it then becomes even harder to estimate the initial v_p effects effectively, increasing the risk of attribution of v_p to K_{trans} .

Thirdly, v_e is also overestimated, however rather slightly and consistently throughout all values. This is because v_p adds a concentration to the low temporal resolution part of the curve, but when this is underestimated this effect is attributed to v_e as higher v_e values correspond to a higher

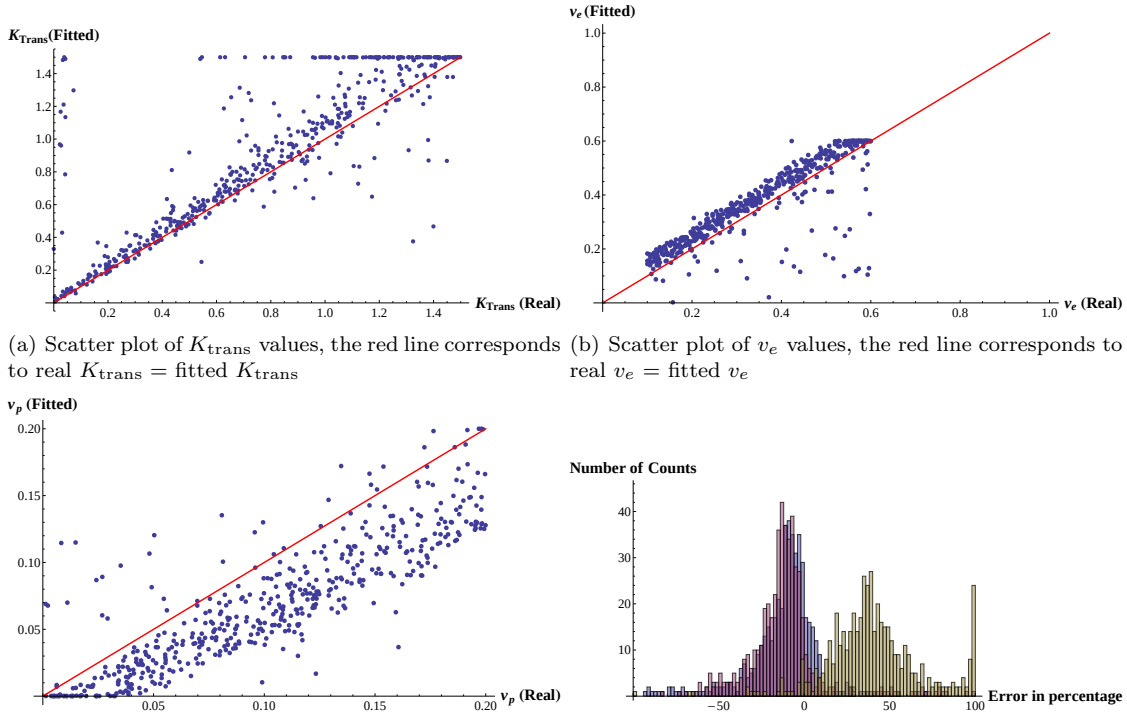

(a) Scatter plot of K_{trans} values, the red line corresponds to real K_{trans} = fitted K_{trans}

(b) Scatter plot of v_e values, the red line corresponds to real v_e = fitted v_e

(c) Scatter plot of v_p values, the red line corresponds to real v_p = fitted v_p

(d) Histogram of the error for K_{trans} (blue bars), v_e (purple bars) and v_p (brown bars) in percentage

Figure 4.16: Scatter plots and the histogram for fitted parameters using the extended Tofts model with simulated clinical data

concentration in the low temporal resolution part of the curve.

If we then inspect the histogram of the extended model (4.16d) we can see that when compared to the standard model the error in K_{trans} and v_e is higher on average then in the standard model (which is not good). v_p can generally not be fitted, the errors are too large and so is the spread of these errors, so you cannot define a bias correction factor. We can thus state that with clinical data with these uncertainties and this temporal resolution it is not possible to use the extended Tofts model adequately.

Results: Shutter Speed Model

Now that we inspected the Tofts models, lets look into the shutter speed model. The results of these simulations are shown in figure 4.17. Lets start with the analysis of the results for τ_i, this models specific extra parameter. We can see that it is generally underestimated and additionally there is a large spread in values, so we can rather safely state that this parameter can not be fit reliably. The general underestimation of this parameter leads to underestimation of the other parameters, K_{trans} and v_e, which is what we would expect if we look at the meaning of this parameter and the information we have from the initial reports of the developers of this model[60]. The extra underestimation in higher values of K_{trans} can be explained because the same effects as in the standard model are applicable here, the higher peak is generally underestimated due to the undersampling. The underestimation of τ_i is hard to explain because we do not have sensitivity functions, but because it directly influences K_{trans} and v_e effects it might be hard to distinguish it individually from those variables when we have a lower temporal resolution. To illustrate this we plotted three curves in figure 4.18. What we can see in these curves is that we can get almost equal curves with completely different parameter values. If we then reduce the quality of this data with undersampling and noise it will be almost impossible to find the parameter values correctly,

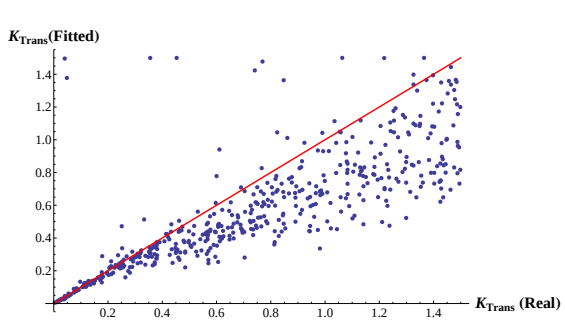

(a) Scatter plot of K_{trans} values, the red line corresponds to real K_{trans} = fitted K_{trans}

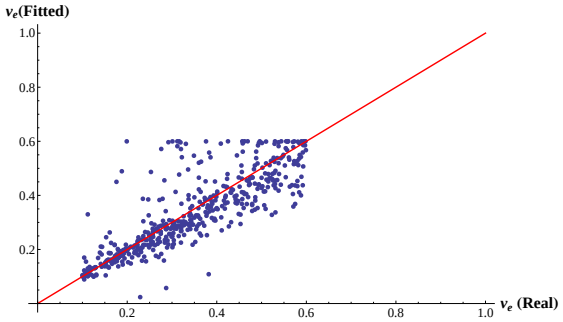

(b) Scatter plot of v_e values, the red line corresponds to real v_e = fitted v_e

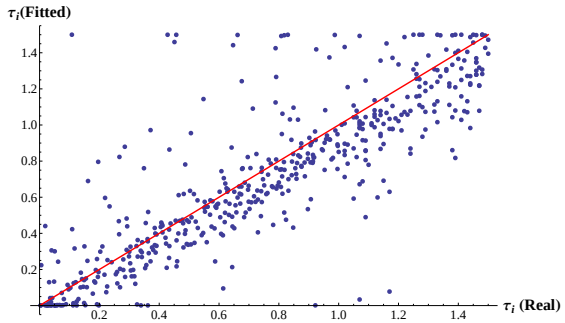

(c) Scatter plot of τ_i values, the red line corresponds to real τ_i = fitted τ_i

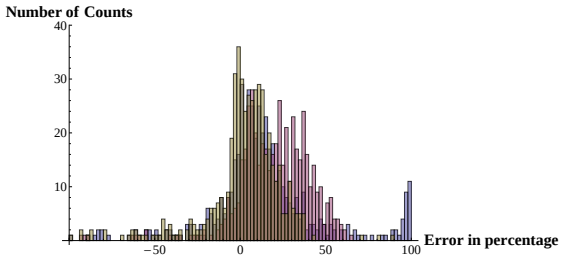

(d) Histogram of the error for K_{trans} (blue bars), v_e (purple bars) and τ_i (brown bars) in percentage

Figure 4.17: Scatter plots and the histogram for fitted parameters using the shutter speed model with simulated clinical data

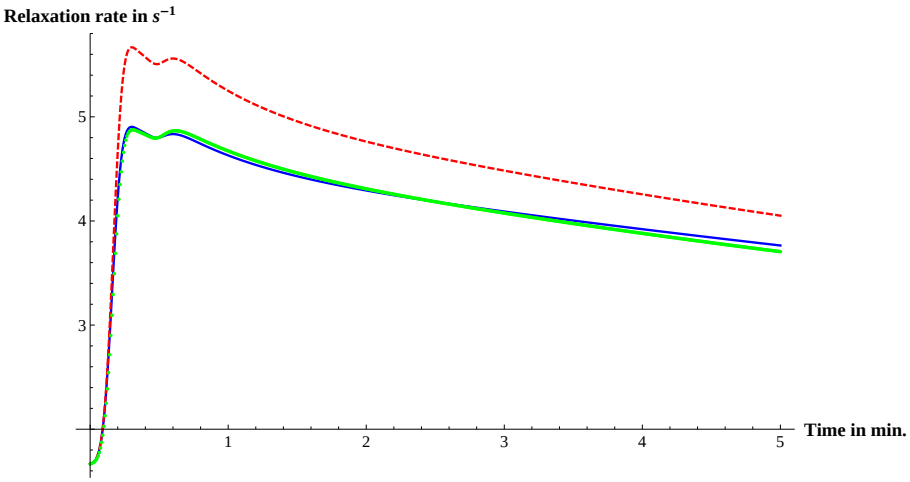

Figure 4.18: The relaxation rate vs time curves. The blue solid curve corresponds to K_{trans} =.7, v_e=.4 and τ_i=.3, the red dashed curve corresponds to to K_{trans} =.7, v_e=.4 and τ_i=.001 and the green curve corresponds to K_{trans} =.6, v_e=.34 and τ_i=.001

there will be too many local minima close to the global minimum to expect a good parameter fit. This immediately shows that this model is not suited for the fitting of data of this quality.

Brix model

Now we have one model left, for which we have the hypothesis that it will probably be worse in fitting simulated clinical data than the extended Tofts and shutter speed models, because it includes another extra parameter. The results of the simulations with the Brix model are shown in figure 4.19. We can see immediately that v_p and F are generally not fitted wel. The extension

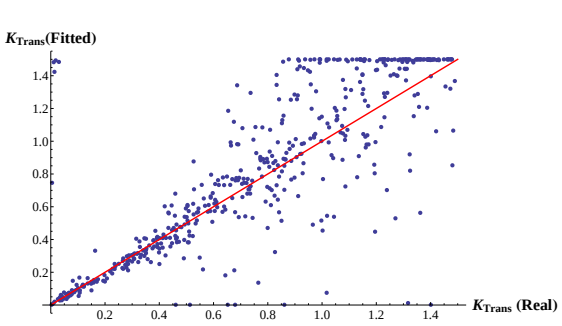

(a) Scatter plot of K_{trans} values, the red line corresponds to real K_{trans} = fitted K_{trans}

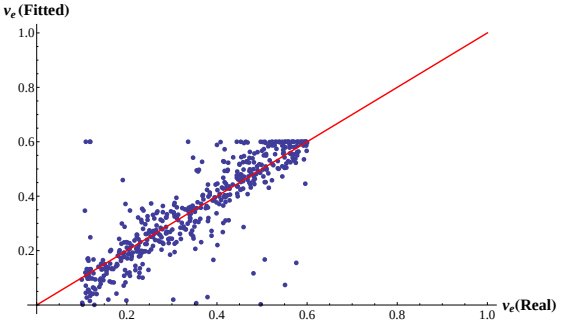

(b) Scatter plot of v_e values, the red line corresponds to real v_e = fitted v_e

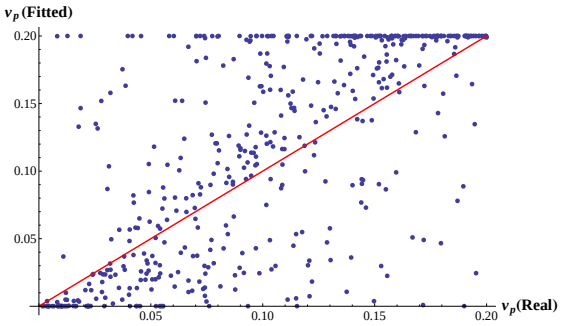

(c) Scatter plot of v_p values, the red line corresponds to real v_p = fitted v_p

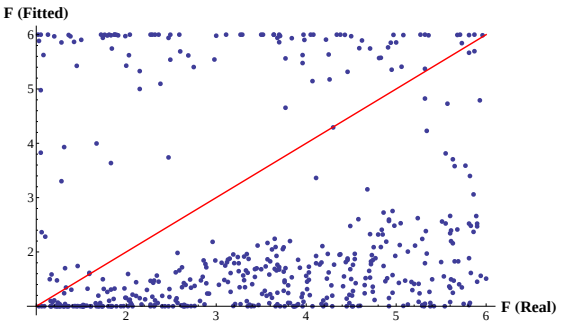

(d) Scatter plot of F values, the red line corresponds to real F = fitted F

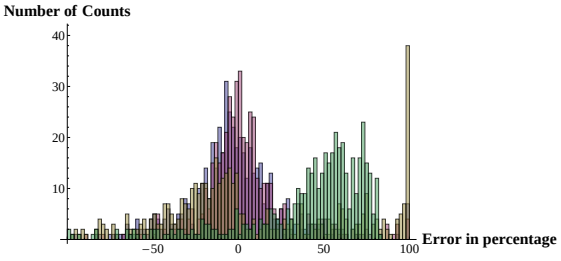

(e) Histogram of the error for K_{trans} (blue bars), v_e (purple bars), v_p (brown bars) and F (green bars)in percentage

Figure 4.19: Scatter plots and the histogram for fitted parameters using the Brix model with simulated clinical data

of the model with these parameters has no use for these types of clinical data. What we see is that F is underestimated on general, which means that there is an overestimation of its effect as a lower F has a higher effect on the tissue response curve. v_p seems to be rather random, which might mean that it has little effect in this model. The effect of v_p might be partly simulated by F, which could explain its underestimation.

For K_{trans} and v_e the results are not that bad, especially for low values of K_{trans} . However, the problems in estimating high K_{trans} values seem to be increased and randomized compared to the standard Tofts model. In general we can state that the extra parameters are not fitable and

the error in the other parameters is substantially larger than in the standard model.

We still need to keep in mind that the additional errors in assuming a simpeler model are not accounted for yet, extra errors can be introduced due to the neglecting of parameters that do have an effect (neglecting v_p when it is high for example). This will be investigated in subsection 4.4.3. But now that we now that the some models do not function adequately when we use clinical data, we are interested in the requirements we need to put on the data acquisition to be able to use more complicated models.

4.4.2 Estimation of performance at different temporal resolution and noise level

Now that we know that the standard model seems to perform rather well with regular clinical data it is interesting to investigate what requirements we need to get the pharmacokinetic parameters within a certain margin of error. To this end we will do some simulations with different levels of noise and different temporal resolutions, but only for the high temporal resolution part, thus the first 90 seconds of enhancement. The latter part of the curves will remain the same low temporal resolution throughout the simulations. The reason for this is that we want to keep clinical practice intact, for radiologists it is important to have several high spatial resolution post-contrast images to assess morphological features. To this end we will keep the last high spatial resolution points the same. In addition to the need of the radiologists the necessity for high temporal resolution in the latter part of the curves is not there. We can easily characterize the last 3.5 min of the curves with a few points.

Now for our simulations, for the standard model we will use 10, 20, 30, 40 and 50 time points in the first 90 seconds of enhancement and we will use noise levels of 0 to 2 times the clinical data concentration uncertainty with steps of 1/3. This results in 30 Monte Carlo simulation sets, for which it is not really illustrative to show all 30 histograms and scatter plots. We choose to estimate the mean error value and the standard deviation of the error for each parameter. To exclude clear fit failures which could influence correct estimation of the mean and the standard deviation we only consider the error values between the 1/8 and 7/8 quantiles. We empirically determined this boundary using visual inspection of the histograms. We also considered using a fit measure like R^2 but in very low temporal resolution situations that will not be adequate because the fit can be quite reasonable but the errors in parameters large due to the increase of local optima in the fitting procedure.

The mean value of the error is a measure of the bias in the parameter (which is related to accuracy in statistics) and the standard deviation is a measure for the reproducibility, related to the statistic term precision. This means that if for example the mean is high but the standard deviation is very low we might be able to use a bias subtraction to get better values. If the standard deviation is large than this cannot be done because there is too big a spread in the errors and there might be no real bias.

Results: Standard Tofts Model

Firstly we will investigate the results for the standard Tofts model. Let's look at the contour plots of the error compared to noise level and temporal resolution for K_{trans} , shown in figure 4.20 We can see that the bias in K_{trans} is mostly dependent on the temporal resolution, an increase in temporal resolution gives a more significant bias reduction when compared to noise reduction. If we want to give a recommendation of which temporal resolution and noise level to use we need to define a certain boundary. To this end we will first use the Jarque-Bera test[16] to test our histogram of K_{trans} distribution for normality. If this is true, we can use the rules stated by the central limit theorem, which means that for a 95% confidence interval all values should be within the mean plus/minus two standard deviations. We could then use this to state that at a certain resolution and noise level we can define a confidence interval for the error.

The Jarque-Bera test shows that we cannot assume a normal distribution of the parameter errors for our data sets ($p < .05$ in all cases). However, as our data does not have a normal

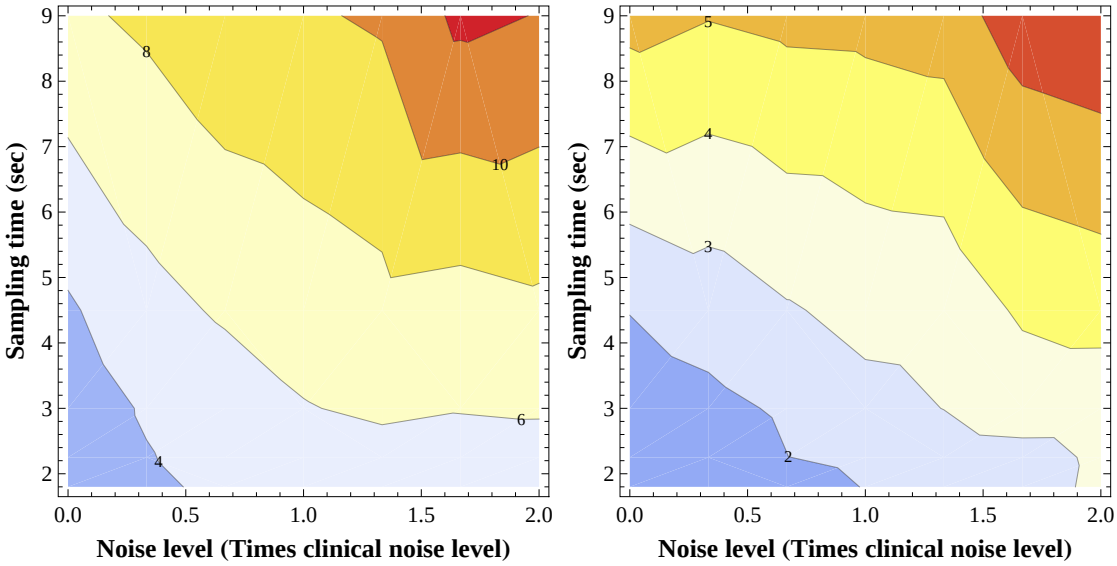

(a) Contour plot of the bias in K_{trans} in the standard Tofts model

(b) Contour plot of the standard deviation of the distribution of the errors of K_{trans}

Figure 4.20: Contour plots for K_{trans} using the standard Tofts model, the contour lines represent boundaries, you draw a line from the axes to get a value of bias or standard deviation for those two variables

distribution we need to revert to Chebyshev's inequality[39]. This states, for any distribution, that a 90% confidence interval can be established by the mean of the distribution plus/minus $\sqrt{10}$ standard deviations. If we use the one sided inequality (which we can if we use the absolute value of the error, as it is not important what sign the error has, only its value is of importance) we get a 90% confidence interval for the mean ± 3 standard deviations. We can then calculate what kind of errors to expect within a 90% confidence interval for each parameter. These are shown in table 4.2.

	$\frac{0}{3}$	$\frac{1}{3}$	$\frac{2}{3}$	$\frac{3}{3}$	$\frac{4}{3}$	$\frac{5}{3}$	$\frac{6}{3}$
10	23	23	25	25	26	32	32
20	9	12	15	16	17	19	20
30	7	9	11	14	15	16	16
40	7	8	10	11	13	13	14
50	6	7	9	10	12	12	14

Table 4.2: Error values in percentages for a 90% confidence interval on K_{trans} when using a different number of time steps (y-axis) and a noise level multiplier (x-axis)

The meaning of these values might be a little hard to interpret out of the blue. The error value in the table for a certain number of timesteps and noise level means that if we would repeat the experiment 100 times we would expect 90 of those experiments to be within the same error range (from 0 to the value in the table). So for our clinical data (20 timesteps, noiselevel 1) we can say that if we don't know anything about the value of K_{trans} beforehand we have a 90% chance that the error is somewhere between 0 and 16%.

For v_e noise in the high temporal part seems to have little to no influence, the bias and standard deviations fluctuate with small values. This means a contour plot might not be as illustrative as it is for K_{trans} . That is why we took the mean value of the error over all noise values for each temporal resolution and plotted a scatter plot in figure 4.21. What we see is logical, the chance of capturing the maximum of the data increases with higher temporal resolution and that is also

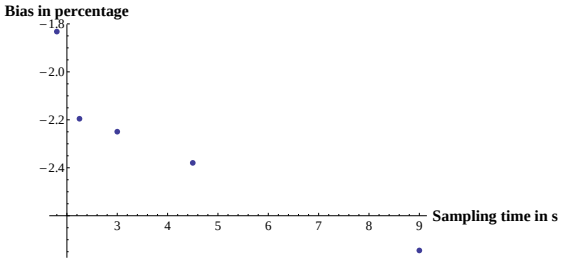

(a) Plot of the bias over different temporal resolution

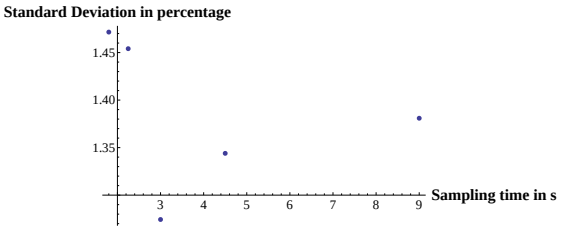

(b) Plot of the standard deviation in the error of v_e over different temporal resolution

Figure 4.21: Plots of the bias in v_e and standard deviation in the error distribution of v_e

important for the assessment of v_e, which we can see in both the bias and the standard deviation of v_e. If we work out the errors for v_e in a table similar to K_{trans} we get the results in table 4.3. What we see is that v_e has lower errors than K_{trans} , as expected. For v_e the requirements on the

	$\frac{0}{3}$	$\frac{1}{3}$	$\frac{2}{3}$	$\frac{3}{3}$	$\frac{4}{3}$	$\frac{5}{3}$	$\frac{6}{3}$
10	7	7	7	7	8	8	7
20	6	7	7	7	8	7	8
30	6	6	7	7	7	7	7
40	6	6	6	7	6	7	7
50	6	6	6	7	7	7	7

Table 4.3: Error values in percentages for a 90% confidence interval on v_e when using a different number of time steps (y-axis) and noise levels (x-axis)

data are much lower and we can get away with about any resolution and noise level. Now we know what we can expect from our standard Tofts model, let's move on to the extended Tofts model.

Results: Extended Tofts Model

For the extended Tofts model we will use the same procedure as we did for the standard Tofts model, but we have an extra parameter in v_p. First we will look at the contour plots for K_{trans} , which are shown in figure 4.22. What we can see is that the bias is negative and that it is a lot larger than for the standard model at lower temporal resolutions. We can also see that the bias is mostly influenced by temporal resolution and less by noise. For the standard deviation we see that the values are also a lot higher compared to the standard model. If we combine these results we can immediately see that the demands on the data are higher for the estimation of K_{trans} using this model. Before we look into the confidence intervals of this parameter we will have a look at the other parameters of this model and then combine the results in one table.

In figure 4.23 we can see the contour plots for the estimation of v_e in the extended model.

The behavior we see is fairly similar to that of K_{trans} . The bias is largely dependent on the temporal resolution and the standard deviation is more of a mixture, however still largely determined by the temporal resolution. In addition the errors here are much larger than the errors in the standard Tofts model. For high temporal resolutions we still have a quite accurate estimate. It has a worse bias than K_{trans} , but its standard deviation is better.

The third and last parameter, v_p is the most difficult to fit, which we can also see in the contour plots of this parameter in figure 4.24.

What we see is that for low temporal resolutions it is impossible to fit v_p, the bias is large and the standard deviation is too. What we see when visually inspecting the histograms that form the contour plot and when we look at the contour plot of the standard deviation is that the standard deviation is not stable over different noise levels for low temporal resolution. This is because there

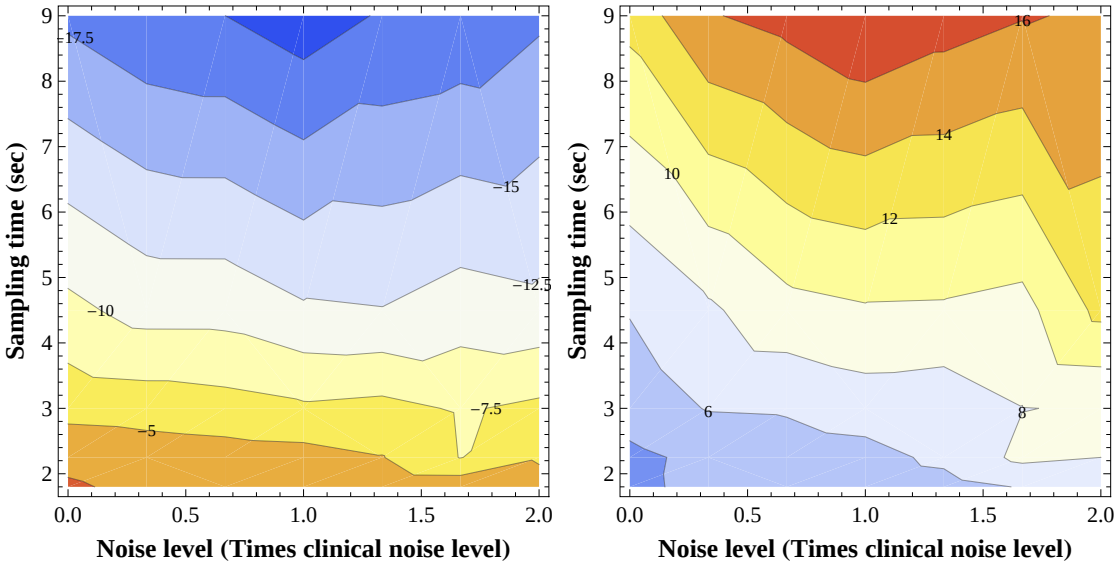

(a) Contour plot of the bias in K_{trans}

(b) Contour plot of the standard deviation of the error distribution of K_{trans}

Figure 4.22: Contour plots for K_{trans} using the extended Tofts model, the contour lines represent boundaries, you draw a line from the axes to get an error value for those two variables

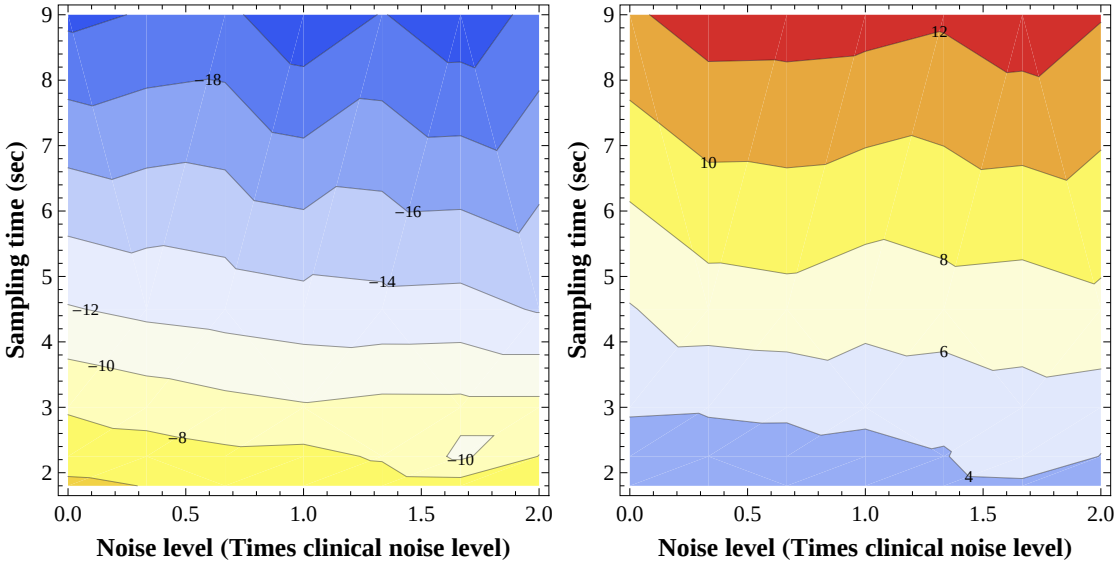

(a) Contour plot of the bias in v_e

(b) Contour plot of the standard deviation of the error distribution of v_e

Figure 4.23: Contour plots for v_e using the extended Tofts model, the contour lines represent boundaries, you draw a line from the axes to get an error value for those two variables

is an erratic data distribution, it is spread over the entire range and the histogram contains fit failures relatively often, especially at low values of v_p, were v_p is often neglected in the fitting proces.

When looking at all the contour plots for this model we can see that there seems to be an anomaly in the lower right corner, where the contours often change abruptly. This is probably caused by inclusion of a large error in the calculation of the mean in one of the 30 simulations.

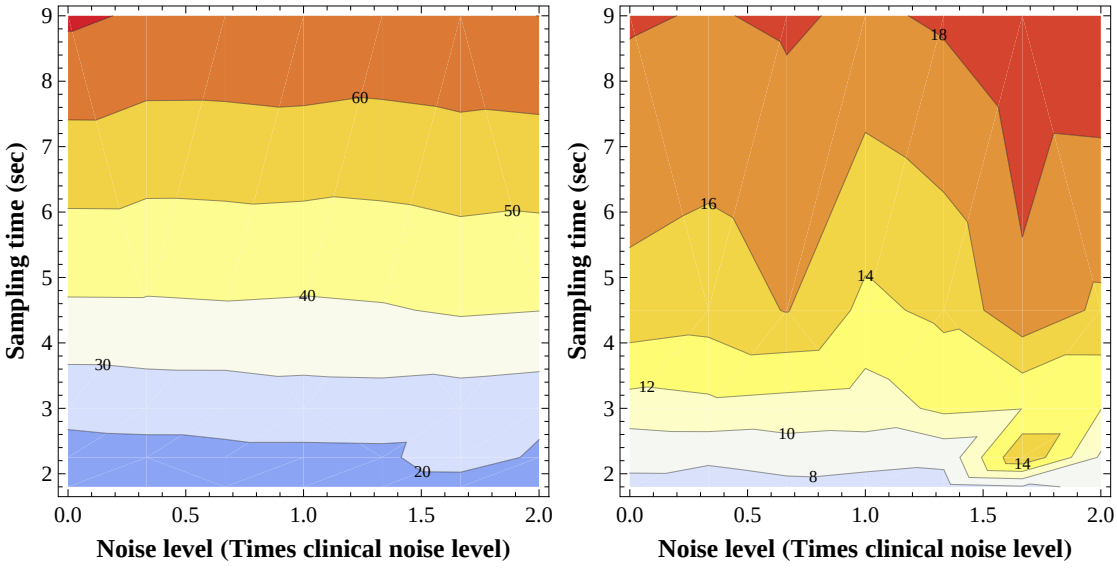

(a) Contour plot of the bias in v_p

(b) Contour plot of the standard deviation of the error distribution of v_p

Figure 4.24: Contour plots for v_p using the extended Tofts model, the contour lines represent boundaries, you draw a line from the axes to get an error value for those two variables

Due to the fact that the rest of the graph is interpolated one anomaly can cause those kind of disturbances.

If we then look at the confidence intervals for all three variables in table 4.4

(a) K_{trans}

	$\frac{0}{3}$	$\frac{1}{3}$	$\frac{2}{3}$	$\frac{3}{3}$	$\frac{4}{3}$	$\frac{5}{3}$	$\frac{6}{3}$
10	56	67	70	74	70	66	64
20	28	34	39	41	41	39	47
30	21	24	25	27	26	30	29
40	13	16	18	18	23	31	27
50	13	16	15	16	17	19	23
90	8	8	9	9	11	11	13

(b) v_e

	$\frac{0}{3}$	$\frac{1}{3}$	$\frac{2}{3}$	$\frac{3}{3}$	$\frac{4}{3}$	$\frac{5}{3}$	$\frac{6}{3}$
10	56	59	58	60	57	61	56
20	30	34	35	33	35	34	37
30	21	21	22	24	23	25	25
40	16	17	18	16	20	28	20
50	13	15	15	16	16	17	18
90	9	10	11	12	11	12	13

(c) v_p

	$\frac{0}{3}$	$\frac{1}{3}$	$\frac{2}{3}$	$\frac{3}{3}$	$\frac{4}{3}$	$\frac{5}{3}$	$\frac{6}{3}$
10	126	122	123	122	123	128	129
20	85	83	87	79	83	93	87
30	57	59	58	59	63	61	60
40	41	41	44	44	43	74	47
50	35	34	36	33	34	36	37
90	20	16	20	16	18	19	20

Table 4.4: Error values in percentages for a 90% confidence interval on extended Tofts model parameters when using a different number of time steps (y-axis) and noise levels (x-axis)

The first to note is that we added an extra simulation where the temporal resolution in the first part of the curve is 1 second, 90 timesteps. This is because the results are rather disappointing. We need a rather large temporal resolution, thus a small sampling time, to fit K_{trans} and v_e with errors lower than 20 percent and for v_p it's even worse. Although these errors are quite large, we

still might be able to distinguish between different classes of tumor. To know this we would need some sort of ground truth values for certain tumors, which are not available in current research. We also simulated the curves with the same temporal resolution as the ideal data and no noise in the first 90 seconds of the curve to look at the effect of the low temporal resolution in the final part of the curve. The errors in K_{trans} and v_p reduce to about 1 percent and 1.9 percent bias respectively with a standard deviation of 1.5 percent and 1.8. The error in v_e, which is largely determined by this final part is a 3 percent bias and a standard deviation of 1.9 percent. When compared to the 1 second temporal resolution we can see that especially v_p can benefit from further increases in temporal resolution in the high temporal resolution part, but also in the low temporal resolution part, as v_p also plays a part there.

For our clinical data we decided to not use the extended Tofts model, because we could never obtain a reasonable value for v_p and the errors in K_{trans} and v_e are much larger than when using the standard model. The errors caused by neglecting v_p we will discuss in subsection 4.4.3.

Results: Shutter Speed model

For the shutter speed model we can use the same proces as we did for the extended Tofts model. In figure 4.25 we see the contour plots for the error in K_{trans} . We can see that the errors in

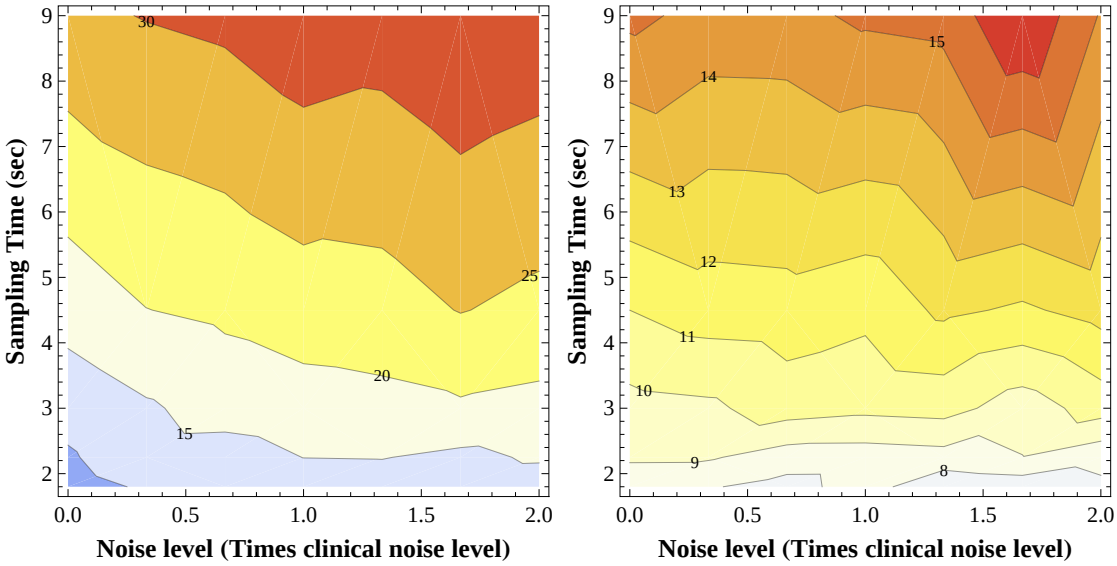

(a) Contour plot of the bias in K_{trans}

(b) Contour plot of the standard deviation of the error distribution of K_{trans}

Figure 4.25: Contour plots for K_{trans} using the shutter speed model, the contour lines represent boundaries, you draw a line from the axes to get an error value for those two variables

general are even larger than in the extended Tofts model, giving an indication that there are even more stringent demands on the quality of the data when comparing those two models. The error in K_{trans} is, as in the Tofts models, largely dependent on the temporal resolution of the data, the noise levels are of less importance. When we look at the standard deviation we can see the same general behavior, it is more noise dependent than the bias but is still largely determined by the temporal resolution.

If we look at the contour plots for v_e in figure 4.26, we can see the same effects we already saw in the other two models.

For v_e the errors are lower, the bias especially seems to have reasonable values over different temporal resolution and noise when compared to the extended Tofts model. The standard deviation is slightly worse when compared to the extended Tofts model. Generally we see that v_e is quite noise independent. Lastly, we have the third parameter, which is unique to this model, τ_i.

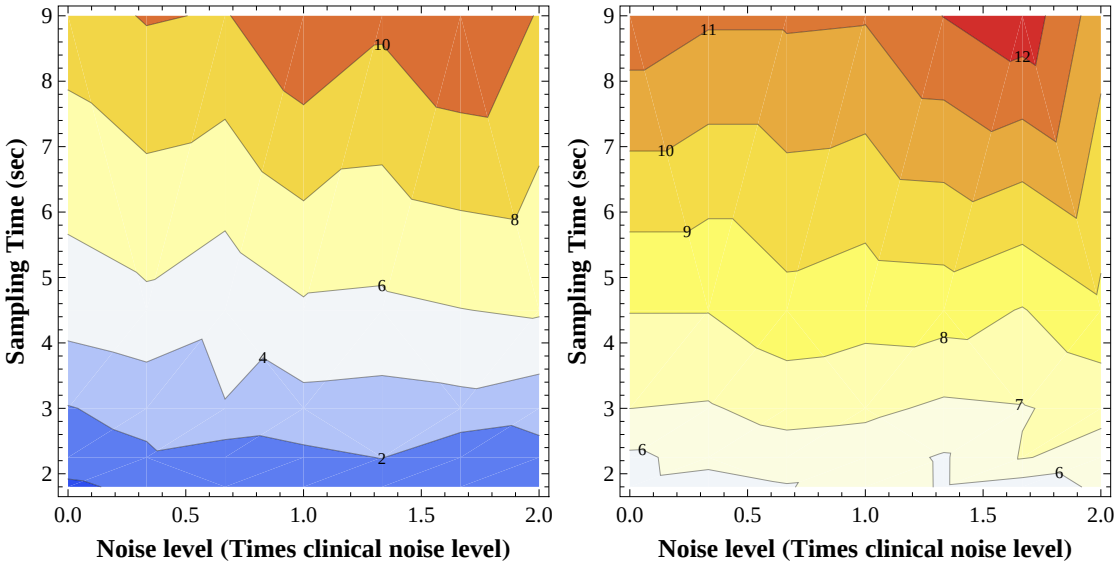

(a) Contour plot of the bias in v_e

(b) Contour plot of the standard deviation of the error distribution of v_e

Figure 4.26: Contour plots for v_e using the shutter speed model, the contour lines represent boundaries, you draw a line from the axes to get an error value for those two variables

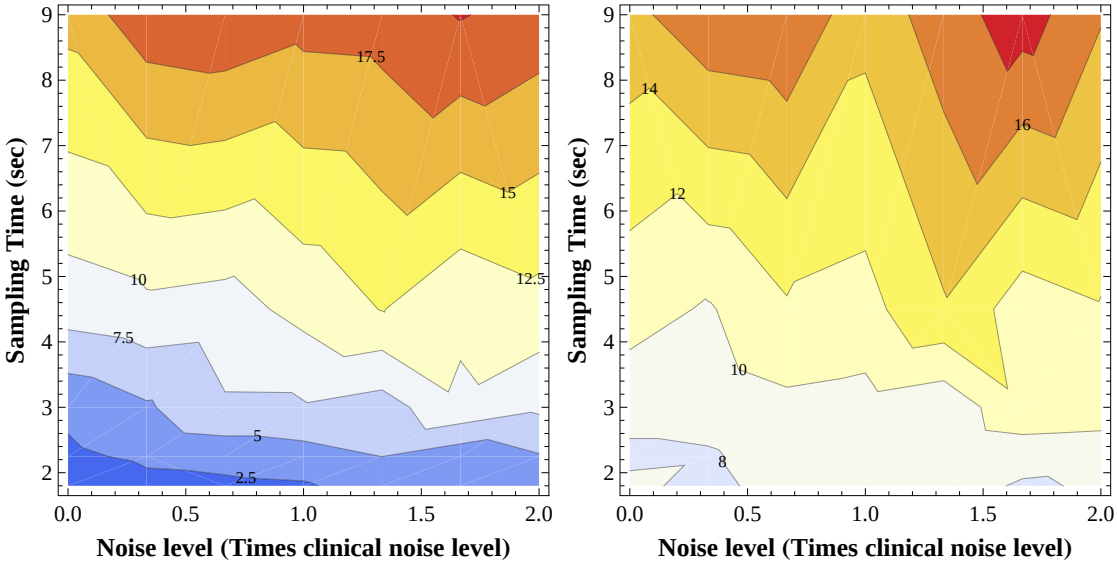

(a) Contour plot of the bias in τ_i

(b) Contour plot of the standard deviation of the error distribution of τ_i

Figure 4.27: Contour plots for τ_i using the shutter speed model, the contour lines represent boundaries, you draw a line from the axes to get an error value for those two variables

The bias of τ_i is generally quite good for different temporal resolutions, around 7.5 percent for clinical data. The standard deviation is worse, at around 11 percent, however still a lot better than for example v_p. But the question is if τ_i might be a clinical valuable parameter, there is no research on the distribution of τ_i for differente cancer types or even benign and malignant lesions. For v_p we can say that its values should be clinically relevant, so our preference would go to the estimation of v_p over τ_i. The reason for fitting τ_i, which is that we then get a better estimate

of K_{trans} and v_e seems to be lost in the fact that the error in K_{trans} is quite large for clinically relevant temporal resolutions, which is also true for the extended Tofts model, but to a lesser extent. Lastly, let's look at the confidence intervals for the shutter speed model in table 4.5

(a) K_{trans}

	$\frac{0}{3}$	$\frac{1}{3}$	$\frac{2}{3}$	$\frac{3}{3}$	$\frac{4}{3}$	$\frac{5}{3}$	$\frac{6}{3}$
10	75	74	75	79	78	85	78
20	50	54	56	56	60	61	61
30	41	44	48	49	50	48	50
40	37	41	38	40	41	41	40
50	34	35	34	38	34	35	36
90	19	22	22	24	24	25	24

(b) v_e

	$\frac{0}{3}$	$\frac{1}{3}$	$\frac{2}{3}$	$\frac{3}{3}$	$\frac{4}{3}$	$\frac{5}{3}$	$\frac{6}{3}$
10	44	44	43	45	47	50	41
20	29	30	31	31	31	30	33
30	23	23	26	25	24	24	25
40	19	21	21	21	20	22	21
50	17	17	18	20	18	17	19
90	14	13	11	15	15	16	15

(c) τ_i

	$\frac{0}{3}$	$\frac{1}{3}$	$\frac{2}{3}$	$\frac{3}{3}$	$\frac{4}{3}$	$\frac{5}{3}$	$\frac{6}{3}$
10	62	71	73	62	70	77	68
20	41	39	44	45	54	43	47
30	30	31	36	35	32	44	42
40	24	26	30	28	30	30	30
50	26	24	29	26	31	26	29
90	23	22	17	19	15	20	16

Table 4.5: Error values in percentages for a 90% confidence interval on shutter speed model parameters when using a different number of time steps (y-axis) and noise levels (x-axis)

This is the reason we do not choose the shutter speed model for our clinical data.

Results: Brix model

For the Brix model we choose a different approach. Due to time constraints and the knowledge that this model will probably yield inadequate results at lower temporal resolution we decided to not create a full map of this model. As it seemed that all models are relatively well suited in dealing with noise when compared to a lower temporal resolution we decided to only test the Brix model over different temporal resolutions with no noise in the high temporal part to see its best performance over different temporal resolution.

The results for its parameters are shown in figure 4.28. These results are comparable to the other models, results improve considerably especially in the biasses when temporal resolution is higher. The standard deviation only decreases substantially due to the first decrease in sampling time (from 9 to 4.5), so increasing the temporal resolution does not have a large impact when it is already quite high.

To finish up this part of our research let's look a the confidence interval for the Brix model:

	F	$\mathbf{K}_{\text{trans}}$	$\mathbf{v_e}$	$\mathbf{v_p}$
10	119	56	35	154
20	95	20	22	78
30	93	20	26	83
40	82	17	18	62
50	76	19	19	53
90	64	17	13	44

Table 4.6: Error values in percentages for a 90% confidence interval on Brix model parameters when using a different number of time steps (y-axis)

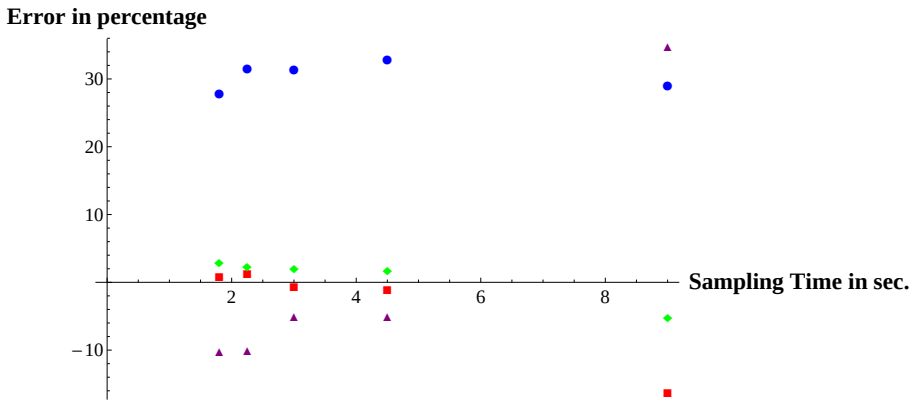

(a) Bias

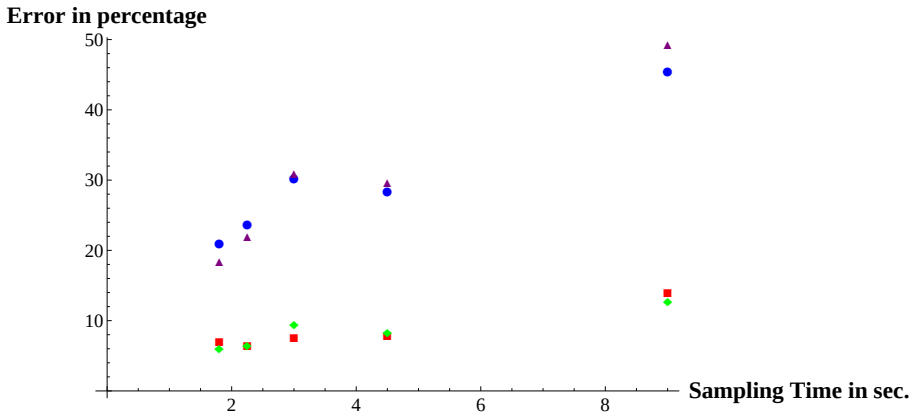

(b) Standard Deviation

Figure 4.28: Plots of the error and standard deviation of the pharmacokinetic parameters of the Brix model at different temporal resolution with no noise in the low temporal part (blue dots corresponds to F, red squares to K_{trans} , purple triangles to v_e and green diamonds to v_p)

4.4.3 Using the standard model on clinical data: what assumptions are done to ensure adequate performance?

The most interesting question that remains at the end of this chapter is what kind of assumptions on v_p, F and τ_i need to be done to be able to use the standard model within reasonable error margins. We will never know if these assumptions are really true without some ground truth, but they will do for our purposes.

To this end we simulated clinical data following the same scheme as in our Monte Carlo simulations using the Brix model and the Shutter Speed model and we then fitted those curves using the standard model. We did this 4000 times for the Brix model and 1000 times for the Shutter speed model to be able to cluster F, v_p and τ_i depending on their values. We can then compare the error in K_{trans} and v_e in each cluster to errors in other clusters, which can give indications of what errors to expect when the assumption that v_p and F are negligible are wrong. It would be even better if we could unite the Brix and Shutter Speed models, this would allow to also take into account the increase or decrease of the errors due to interplays between the extra parameters F, v_p and τ_i.

The results for the Brix model fitted with the standard Tofts model are shown in figure 4.29 The axes show the different values of v_p and F and the biasses and standard deviations in K_{trans} and v_e associated with those values. A surprising result might be that when v_p increases the bias in K_{trans} actually decreases. This is because an increase in v_p increases the maximum of the peak

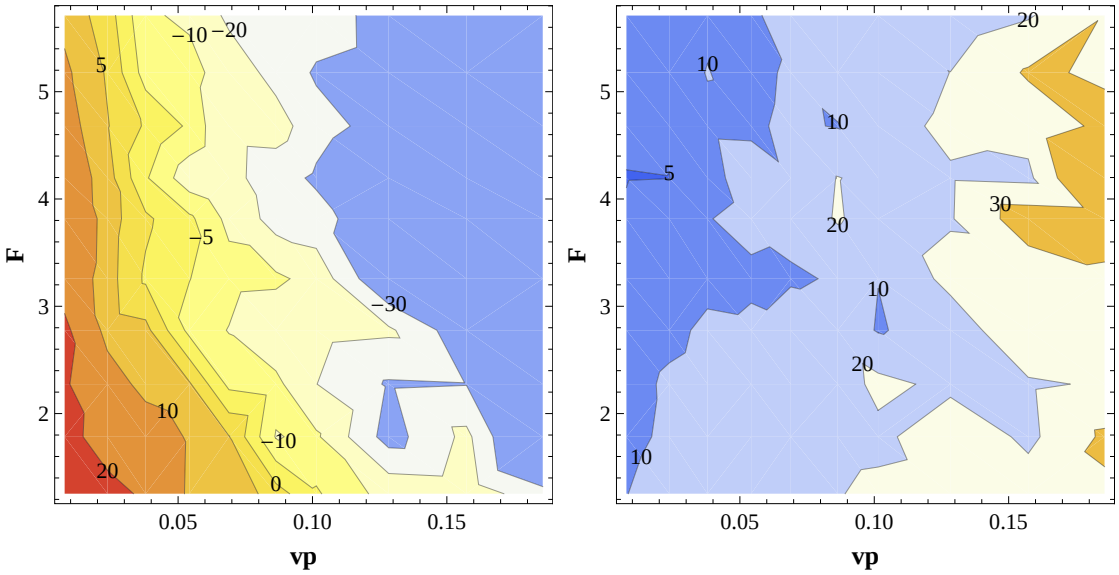

(a) Bias K_{trans}

(b) Standard Deviation K_{trans}

(c) Bias v_e

(d) Standard Deviation v_e

Figure 4.29: Contour plots of the error and the standard deviation of the error distribution in K_{trans} and v_e when fitting the standard model to Brix model simulated curves

of the concentration, which is underestimated because of the lower temporal resolution, which at a certain point are equal, which actually gives a 'better' estimate of K_{trans} . However, if we look at the standard deviation we can see that that increases substantially with increasing v_p, which is perhaps the most important indication of uncertainty in the parameters When v_p approaches zero and F approaches 6 we can say that the standard deviation approaches 5%. When compared to the standard Tofts model simulations this is about 2% higher, which can also be caused by the fact that we have less measurements in the cluster were $F = 6$ and $v_p = 0$ when compared to those simulations (15 compared to 500). The biasses are comparable at those values for v_p and F.

For v_e the biasses are a little higher when compared to the simulations using the standard Tofts model. We can also see that F has almost no influence on v_e. The standard deviations are

also comparable. In general we can say that v_e is the parameter that is easiest to fit with the lowest error.

If we then look at the effect of neglecting τ_i, which is the extra parameter in the shutter speed model we see for K_{trans} (figure 4.30). That it mostly affects the bias in K_{trans} and v_e, which

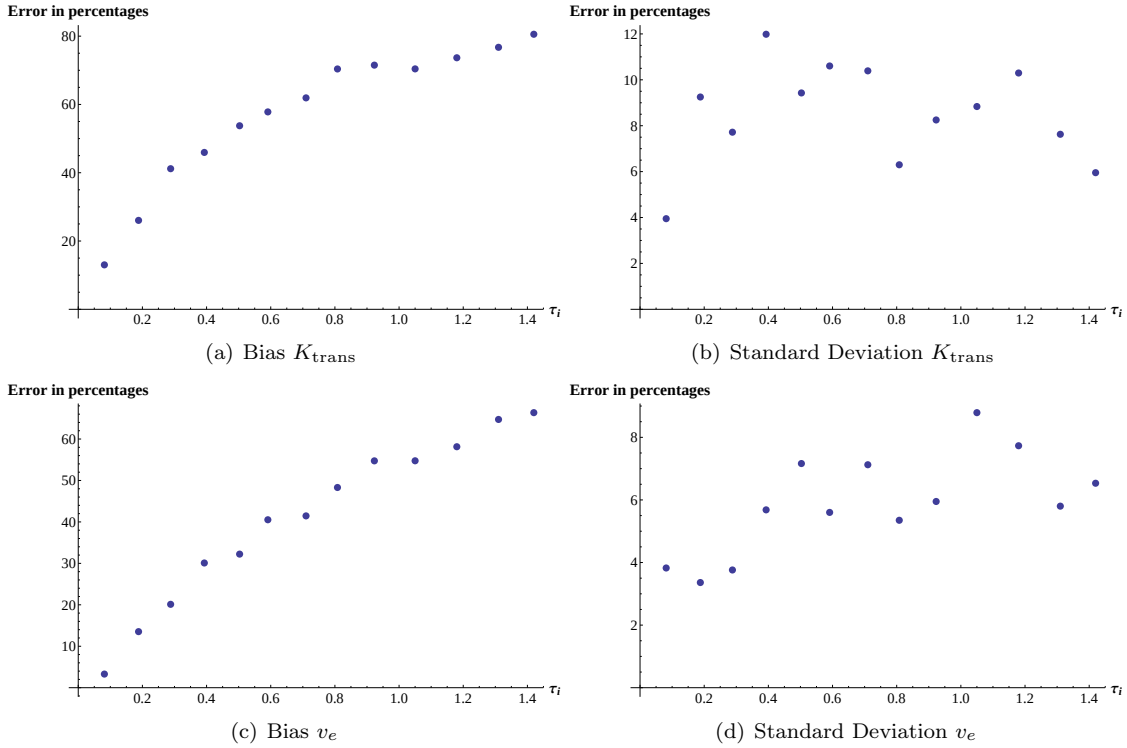

(a) Bias K_{trans}

(b) Standard Deviation K_{trans}

(c) Bias v_e

(d) Standard Deviation v_e

Figure 4.30: Plots of the error and the standard deviation of the error distribution in K_{trans} and v_e when fitting the standard model to shutter speed model simulated curves

increases rather rapidly with increasing τ_i. The standard deviation also seems to increase quickly but then remains stable. What we can say is that if we cannot assume a very low τ_i, we can introduce large errors into our estimates of K_{trans} and v_e.

4.5 Conclusion

We started this chapter by introducing several models that can be used in pharmacokinetic modeling, ranging in complexity and number of parameters. We saw that when we have perfect data the standard and extended Tofts models and the Shutter Speed model will have very good fits in general. The Brix model has more problems, especially in the estimation of the extra parameter F.

For simulated clinical data we saw that the only model that stays within acceptable error margins is the standard Tofts model. We investigated the effect of temporal resolution on the errors made by all models to be able to say something about data requirements for those models. We saw that most models, especially the shutter speed and Brix models need a much higher temporal resolution to adequately fit the extra parameters. We can also state that in general the temporal resolution in our models is more important than the uncertainty in concentration curves, so noise in our images is less important than temporal resolution. However, we do indicate that when SNR is low, the Rician noise might also introduce biasses, in which cases it is important to take those into account.

If we look at our models we can state that the standard Tofts model seems useable with current high temporal clinical data (17 to 22 timesteps during initial enhancement, which is ±90 seconds and 4 to 5 timesteps thereafter), although more investigation should be done in what ranges τ_i and v_p are to be expected in breast cancer to make sure that these parameters do not create large errors.

If we want to use more complex models there are essentially two choices, the extended Tofts model and the shutter speed model. Firstly, one needs to have data with a very high temporal resolution in the fast enhancing part of the curve (at least 2 seconds per image). Secondly, we need to look at what we expect for that specific lesion. If there is a large v_p fraction expected or if there is extra clinical relevance to measure that fraction, for example tracking the effects of anti-angiogenic therapies then the extended Tofts model might be an excellent choice. If we expect a small v_p fraction then we might choose the shutter speed model, which allows more accurate estimation of the parameters K_{trans} and v_e. The second generation shutter speed model includes both behaviors, but will probably have too stringent demands on temporal resolution and noise to be able to fit correctly. However, further investigation could be done to ensure that.

For the Brix model it seems that in general the extra parameter it introduces, F, is not a significant parameter in cancers. It has to have a low value (< 1) to start becoming really significant and as cancers usually have an increased blood flow, this is unlikely. We can see this effect in our simulations, where even in perfect data situations F is hard to fit. We thus do not see a use for this model in breast cancer pharmacokinetic modeling.

Up to this point we did all our simulations with perfect input functions. However, in a real clinical setting we do not have the perfect input function. How to obtain an input function is discussed in the next chapter.

Chapter 5

Obtaining the Arterial Input Function

The arterial input function is input for the pharmacokinetic models and is defined as the concentration of contrast agent in blood plasma. This input function varies greatly between patients and even between different imaging sessions with the same patient. It is thus important to try to get an accurate input function for each individual measurement. First we will discuss several ways to obtain the input function and then we will delve into the methods we investigated for this thesis.

5.1 Ways to obtain the arterial input function

There are several ways to obtain the input function, some more complex than others. At this moment in literature there are roughly five ways to determine the input function:

1. **Blood samples** During the MRI examination the radiologist can take blood samples from the patient, which can then be used to determine the concentration of the contrast agent. The advantage is that this gives very accurate estimates of the input functions at those times. Two very important disadvantages however are the fact that using this method you can never get a high temporal resolution input curve, as this is inherently limited by the time it takes to get a blood sample. Secondly, and perhaps most importantly, this is an invasive procedure. These two disadvantages are the reason why this is not the preferred method to estimate the input function, although it was used in the past [22].

2. **Using large arteries within the image field of view** Using the same method we use to extract the concentration vs. time curves from the tumor we can also estimate the input function from a large artery, for example the aorta. Advantages of this method are that it is non-invasive and that in theory we could obtain a high temporal resolution input function. However, this method has several challenges. Firstly, the changes in concentration in blood are very fast and we would need a very high temporal resolution to accurately estimate the AIF. Secondly, at very high concentration, which can occur in the blood, the linear relation between contrast agent and T_1 reduction is no longer valid. In addition, the larger arteries, especially the aorta suffer from motion and flow artifacts. Estimating the AIF this way is possible, but difficult. Thus, this is not our method of choice.

3. **Use a population averaged / mathematical input function** In literature there are several 'standard' input functions based either on a mathematical model of the bolus behavior in blood or on measurements in patients. Examples of these are the AIFs by Weimann, Orton and Parker. The advantages of these input functions are that they have a high temporal resolution, are noiseless and are easy to use. The most important disadvantage is that they

are not measurement specific and thus can differ significantly from the real AIF. However, if there is no additional data available, these types of input functions are often the only option.

4. **Use a reference tissue method** It is also possible to use a reference tissue. This means we use a tissue with known pharmacokinetic parameters within the image field of view to calculate the AIF with the inverse of a pharmacokinetic model. The advantages are that we have a measurement-specific AIF, we need a lower temporal resolution to estimate the AIF and it is a relatively easy method to implement. The disadvantages are that you need to know the tissue parameters, you need a reliable reference tissue and you need to assume a pharmacokinetic model for this tissue.

5. **Use a multiple reference tissue method** The last method we will discuss is a multiple reference tissue method which is a extension of the single reference tissue method which was recently developed by Yang[57]. The advantage is that you do not need pharmacokinetic parameters for all tissues because you minimize a cost function for the multiple tissues. The other advantages are the same as for the single reference tissue method, the disadvantage is that you need several reference tissues to get a good estimate and these are not easy to find.

We will investigate the useability of the last three methods in this chapter, starting with the population averaged / mathematical input functions.

5.1.1 Population averaged / mathematical input function

Standardized input functions are input functions that have been created using either an average over multiple patients, a so-called population averaged input function or using mathematical transfer functions for the body circulation and functions for the initial bolus. First we will go into the population averaged input functions.

Early population averaged input functions were mostly based on the measurements and knowledge at that time, for example by concentration measurements in blood samples obtained during contrast agent circulations. However, the temporal resolution of those measurement is much too low to correctly capture the characteristic features of the AIF. One example of those early input function models is the Weinmann input function, which is a simple bi-exponential decay[45].

Relatively recently, in 2006, Parker et al.[40] did more than 100 measurements in 23 patients over 5 visits at relative high temporal resolution (4.7 seconds) for the AIF by extracting the concentration information from the descending aorta. Using those measurements they created a mean arterial input function, to which they fit a rather empirical function. The goal of the function was to capture the shape of the curve and not necessarily have any physiological meaning and the function was adequate for this. We have already showed this function in chapter 4, but for completeness sake it is shown here too.

$$C_b[t] = 7.5527e^{\frac{-(t-.171)^2}{.00605}} + 1.003e^{\frac{-(t-.364)^2}{.035912}} + \frac{1.064e^{(-.083t)}}{1+e^{-37.772(t-.482)}} \tag{5.1}$$

This arterial input function is probably the most used function in pharmacokinetic research for breast MRI. During the analysis of the populations AIF they noted that the largest variability is in the first pass peak maximum, which can be changed by changing the amplitude of the first exponential function. This function has much more detail than the Weinmann input function and is the closest we are at the moment to the 'real' input function shape.

The second variant of a standardized input function we are going to look at is one with a mathematical basis instead of experimental basis. There have been several attempts to correctly create an input function from mathematical building blocks, for example a bolus function and a body transfer function[8]. We choose to investigate a model proposed by Orton et al.[37], which was compared to the experimental model by Parker and seemed to give similar results. The biggest advantage in using this model is that it allows analytic calculation of the convolution integral in the standard and extended Tofts models. Disadvantages are that there is no experimental validation for this model, it is based on the theoretical shape an AIF should have.

The model by Orton is based on a superposition of a bolus function and the convolution between a bolus function and a body transfer function, which result in the final AIF model. The final AIF model is then given by:

$$C_b[t] = C_{\text{Bolus}} + C_{\text{Bolus}} \otimes G[t] \tag{5.2}$$

$C_b[t]$	(mM/L)	Concentration in whole blood
C_{Bolus}	(mM/L)	Bolus function
$G[t]$		Body Transfer Function
$\otimes$		Convolution operator

In their own paper they introduced three different models for $G[t]$, in which model three is the most complex. They simulated tissue response functions with the Parker AIF and the extended Tofts model and then showed how large the errors are one would introduce by fitting those curves using their models. The third model gave the best results, so we will introduce that here. That model uses the following two functions for the bolus and the body transfer function.

$$C_{\text{Bolus}} = a_b \mu_b^2 t e^{-\mu_b t} \tag{5.3}$$

$$G[t] = a_e e^{-\mu_e t} + a_r (t - \tau_r) e^{-\mu_r (t - \tau_r)} \tag{5.4}$$

Here a_b determines the bolus area and μ_b the bolus width. For the body transfer function $G[t]$ the first part determines the spread of the bolus due to the transfer through the body and the second part is used for mixing/recirculation. The complete convoluted function is rather complex and is not shown here. The best values for the parameters are calculated by fitting the convoluted equation to the Parker AIF. The result of that proces is shown in figure 5.1.

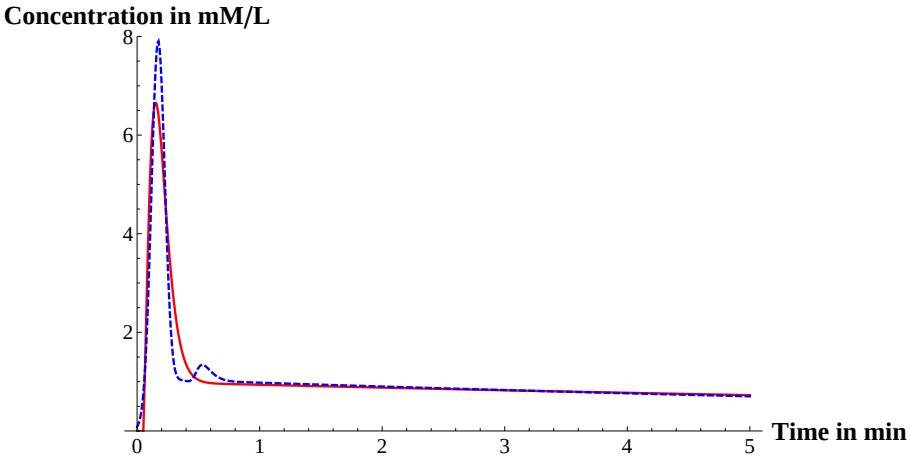

Figure 5.1: The Parker (Blue, dashed) and Orton (Red, solid) AIFs are plotted, where the Orton AIF is fitted to the Parker AIF

For our experiments we decided to choose one of the two AIFs, as they do not differ much in results, according to Orton's research[37]. We picked the AIF by Parker, as it has more detail in shape, has better clinical validation, is used by other researchers which makes our research more comparable.

Errors caused by assuming a population averaged input function

We already mentioned that Parker found that there can be huge deviations between first pass peak heights between different measurements, but what kind of errors are introduced in the pharmacokinetic parameters by these effect? To find an answer to that question we will simulate 5

different peak heights for the AIF and 5 different spreads using the body transfer function from chapter 44.31, the extremes of those 25 AIFs are shown in figure 5.2, which will be our local AIFs.

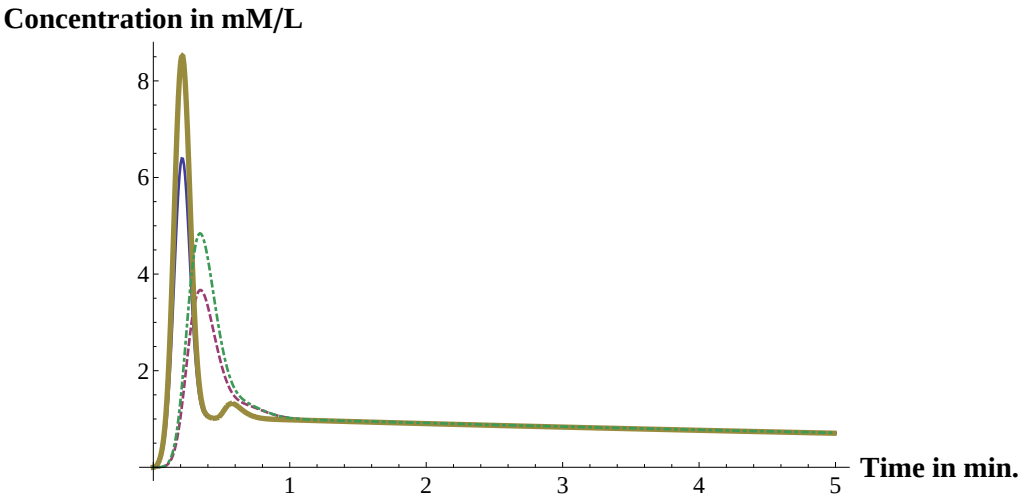

Figure 5.2: The lowest and highest first peak height AIFs with their largest spread counterparts

Then we will use 25 different combinations of K_{trans} and v_e (K_{trans} =.05, .1, .3, .5 and 1, v_e=.1,.2,.3,.4 and .5) to see if the effects caused by a wrong AIF are K_{trans} and v_e value dependent. We thus simulate a tissue response curves using the 25 AIFs for every combinations of K_{trans} and v_e, after which we fit that response curve with the regular Parker AIF. This results in a total of 625 simulations for which we have the fitted and original pharmacokinetic parameters so we can calculate the error the same way we did in section 3.6. The results are presented in 5.3 using the same contour plots we used in chapter 4: We can see that the error in K_{trans} is largely dependent

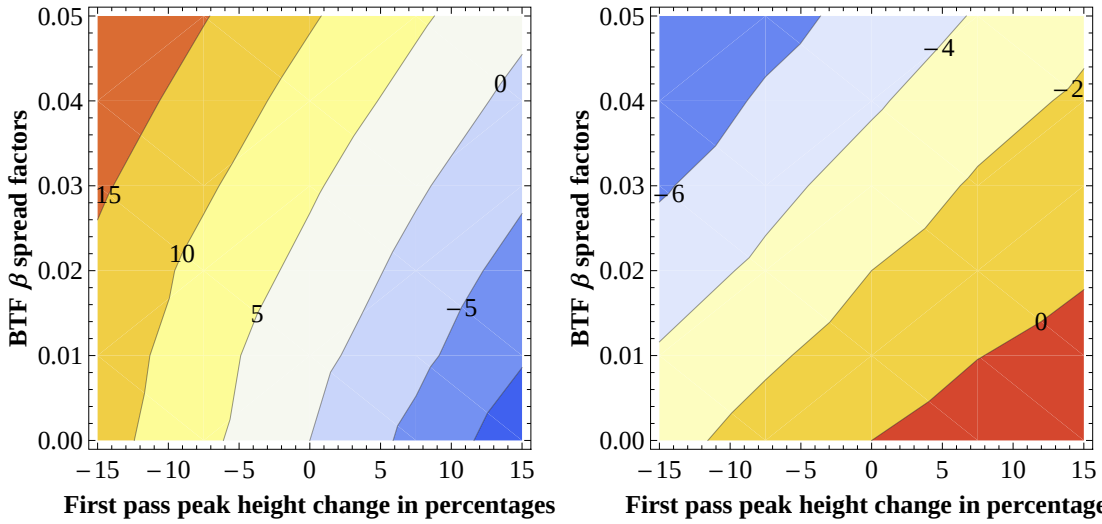

(a) K_{trans} (b) v_e

Figure 5.3: Contour plots for the error in K_{trans} and v_e when we assume the Parker arterial input function instead of the localized input function created using the body transfer function, the spread parameter for the BTF and the first pass peak height deviation are shown on the axes, the contour line represent the error in percentages of the pharmacokinetic parameter

on the height of the first pass, which was expected because K_{trans} determines the initial slope, which is affected by the first pass peak. When the AIF is perfect the error is approximately 0, up till 5% deviation we see that the error in K_{trans} follows the deviation of the first pass peak in the AIF. When deviations are larger than 5% we see that the absolute error in K_{trans} does not follow the deviation of the peak in the AIF but is a little larger when the peak change is negative and a little smaller when the peak change is positive. We also investigated if there was any spread in errors over different values for K_{trans} , but that was not the case, so the errors in K_{trans} value independent.

For v_e we can see that it is much less influenced by the first pass peak height. The influence of the spread is relatively bigger. In general we can say that errors in the AIF can cause rather large errors in the parameters, especially in K_{trans} . For v_e the error is less significant.

5.1.2 Reference tissue method

An entirely different way to estimate the arterial input function is the reference tissue method, which is based on the idea that if you have a tissue of which you would know the pharmacokinetic parameters you can use your pharmacokinetic model to transform that tissue response back to the arterial input function. That AIF can then be used to estimate the pharmacokinetic parameters of the tumor. The biggest advantage of this method is that we can create a measurement specific AIF for every case.

There are two major assumptions in this method, the first being the fact that the AIFs for the reference tissue and the tumor are the same. The second is that pharmacokinetic parameters of stable tissue do not differ very much between individuals. The first assumptions is dependent on wether the reference tissue and the tumor tissue are in close proximity and have for example the same feeding artery. So, one should prefer reference tissues which are close to the tumor over tissues that are far away. The second assumption requires more research, at the moment there has been little research into the spread of pharmacokinetic parameters of regular tissues[38].

Examples of reference tissues are the pectoralis muscles, the spleen (for the left breast) or the liver (for the right breast), which are often in the same field of view as the tumor. Reasonable values from literature for these tissue are K_{trans} =.1, .35 and .7 and v_e=.1,.21 and .28 for muscle, liver and spleen respectively[38;25;58;60].

There are then two methods used in literature, one first used by Kovar et al.[18] and a method proposed by Yankeelov et al[59]. The first method is rather simple and is simply the reciprocal of the differential equation for the standard Tofts model:

$$C_p[t] = C_e[t] + \frac{\frac{\delta C_e[t]}{\delta t}}{k_{\text{ep}}} \tag{5.5}$$

This relatively easy to calculate, however when we are working with clinical data we need to remember that there is noise in our data. The derivative that is in this equation will increase the effect of this noise. To circumvent this problem we can use a method proposed by Yankeelov, which rewrites the entire problem to an integral form. To this end we substitute this equation into the Tofts model and use integration by parts. This will give us:

$$C_t^{\text{TOI}} = R\, C_t^{\text{RT}} + R\left(\frac{K_{\text{trans}}^{\text{RT}}}{v_e^{\text{RT}}} - \frac{K_{\text{trans}}^{\text{TOI}}}{v_e^{\text{TOI}}}\right)\int_0^t C_t^{\text{RT}}[s]\, e^{-\frac{K_{\text{trans}}^{\text{TOI}}}{v_e^{\text{TOI}}}(t-s)} ds \tag{5.6}$$

C_t^{TOI}	(mM/L)	Concentration in tissue of interest
C_t^{RT}	(mM/L)	Concentration in reference tissue
R		$K_{\text{trans}}^{\text{RT}}\ \left(K_{\text{trans}}^{\text{ToI}}\right)^{-1}$

As we can see, this means there is no direct calculation of the AIF but the reference tissue is immediately used as the input for the concentration of the tissue of interest. We will use the last method to calculate the tumor parameters because it is more robust to noise.

Errors introduced by using the single reference tissue method

We will look at the increase of the error in the pharmacokinetic parameters when fitting tissue response curves, comparing the reference tissue method to when we have a perfect AIF for clinical data (section 4.4.1). Firstly we will look how the error in the pharmacokinetic parameters changes for simulated clinical data when compared to the ideal AIF we used in chapter 4. We will use the same simulations but instead of using an ideal AIF (the AIF we used to simulate the tissue response curves) we will use a reference tissue (pectoralis muscle) with the same temporal resolution and noise level as the tumor curve (this curve is generated the same way we generate the tumor curve). In these first simulations we will assume that we know the pharmacokinetic parameters for the reference tissue exactly (K_{trans} =.1 and v_e=.1). The results are shown in figure 5.4. When we look

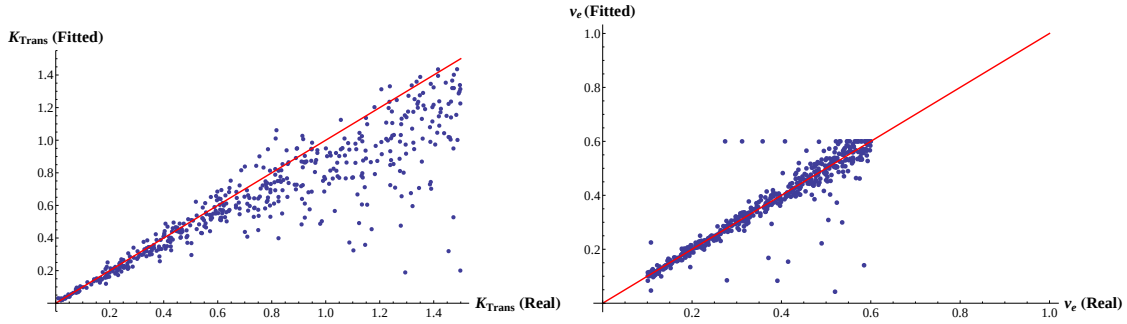

(a) Scatter plot of K_{trans} values, the red line corresponds to real K_{trans} = fitted K_{trans}

(b) Scatter plot of v_e values, the red line corresponds to real v_e = fitted v_e

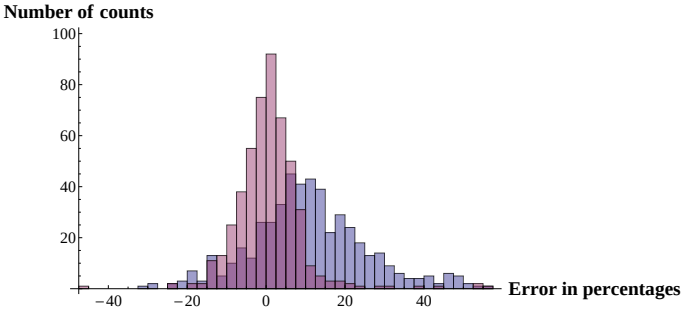

(c) Histogram of the error for K_{trans} (blue bars) and v_e (purple bars) in percentage

Figure 5.4: Scatter plots and the histogram for fitted parameters using the standard Tofts model with simulated clinical data using a reference tissue approach

at the graphs we can see that the bias hasn't changed much when compared to figure 4.15. It is still around 10 percent and it is still higher for larger values of K_{trans} . However, the standard deviation almost doubled. This is because the noise now has double effects. Firstly, when converting to the AIF we add the noise of the reference tissue to the AIF and then this makes it more difficult to estimate K_{trans} from the noisy data. Also the low temporal resolution effects may have doubled for certain K_{trans} values. We can use the same procedure as in section 4.4.1 to determine a confidence interval for K_{trans} . In this case the 90% confidence intervals is 30% compared to 16% when we have the ideal AIF, which means that when repeating the experiment 90% of the values would be within 30% error.

For v_e the situation is comparable when comparing to figure 4.15. The bias is almost the same but the standard deviation is almost doubled. However, the error in v_e is still quite low, its 90% confidence interval is 11% compared to 7%.

The second and last thing we would like to know is how errors in the assumed pharmacokinetic parameters of the reference tissue propagate into the tumor parameters. To this end we

picked three values for the parameters of the reference tissue with K_{trans} =.075,.1 and .125 min^{-1}, v_e=.075,.1, and .125, were the middle values are the true values for pectoralis muscle. We then picked the same 5 values for K_{trans} and v_e of the tumor as in the simulations for the population averaged AIF: (K_{trans} =.05, .1, .3, .5 and 1 min^{-1}, v_e=.1,.2,.3,.4 and .5). Because we have some general knowledge about the increase in the error using the reference tissue method with perfect reference tissue pharmacokinetic parameters from the previous experiment, we will use the Parker AIF to create ideal true reference tissue and tumor curves (noiseless, high temporal resolution) after which we will fit the tumor curves using the 9 different combinations of reference tissue parameters. We would expect one simulation, the one with true values, to have an error of approximately 0 for all different K_{trans} and v_e for the tumor. We will look if the error is stable over the range of tumor parameters. We do this on ideal data instead of clinical data to clearly see the effects of wrong assumption of reference tissue parameters. The results of these simulations are shown in figure 5.5: What we see in this figure is rather logical, the errors in the parameters

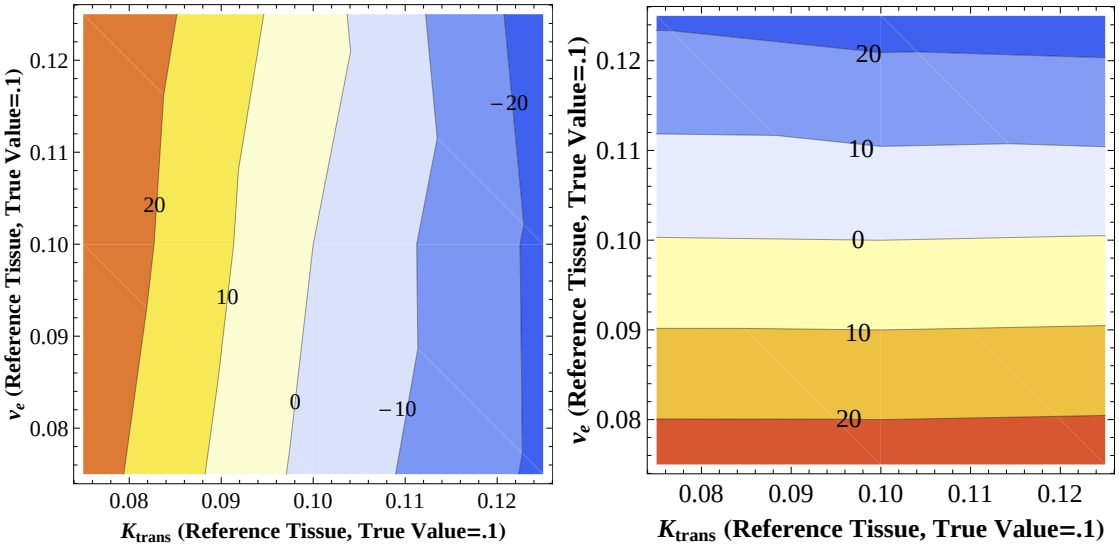

(a) K_{trans} (b) v_e

Figure 5.5: The error in the fitting of the pharmacokinetic parameters of the standard Tofts model when assumed reference tissue parameters are wrong, true values for the reference tissue are K_{trans} =.1 min^{-1} and v_e=.1

of the reference tissue have a linear but opposite effect on the estimation of the parameters of the tumor. A 20% error in the reference tissue parameters leads to an error of -20% in the tumor parameters. We can also see that errors in K_{trans} only effect K_{trans} and errors in v_e only v_e.

Summarizing, an extra error in the parameter estimates is introduced by using the single reference tissue method (compared to when we have an ideal AIF), but it is a lot smaller than compared to the population AIF, there the error in parameter estimates scales approximately linearly, thus errors up to 300%, while our reference tissue method is within 30%, if we have our reference tissue parameters correct. However, if these are incorrect those errors have a linear effect on the error in the tumor parameters, which can be large also. The biggest problems in this method are the reference tissue parameters and the noise in the reference tissue. Logically, noise has a larger effect in tissue with low enhancement, so it is best to look for a tissue with high enhancement (spleen for example). Another method is the multiple reference tissue method.

5.1.3 Multiple reference tissue method

The problem with the single tissue reference method is that we need the pharmacokinetic parameters of the reference tissue to be able to use it. These are often not known and more research is

needed to assess the variability among different individuals. Recently another method was developed that circumvents these problems by using multiple reference tissues by Cheng Yang et al.[57] In his paper Yang introduces a generalized mathematical framework for his method. We will here derive it more explicitly for the standard Tofts model. The basis of this method is the assumption that several reference tissues have the same AIF.

The process is as followed:

1. **Choose starting parameter values for the reference tissues** We need to choose starting parameters for every tissue randomly, which will change during the course of the minimization of the cost function.

2. **Calculate the AIF for each reference tissue and then create a mean AIF** We will use the inverse of the standard Tofts model, in which we will use the numerical calculation of the convolution integral to estimate the AIF for each reference tissue. Then we will take the mean of these AIFs as the 'true' AIF

3. **Calculate the cost function** After this we will use the reference tissue parameter values and the 'true' AIF to calculate the tissue response curves for all reference tissues. The cost function is the sum of squared differences between these calculated tissue response functions and the tissue response function from the data.

4. **Minimize this cost function** We then use a minimization scheme, once again the Nelder-Mead algorithm, to find the reference tissue parameters for which we find an AIF that minimizes the cost function

The reference tissue parameters we find in this case are not that important. The important fact is that we can construct an AIF this way that is independent of the pharmacokinetic parameters of the reference tissues. We do have a scaling problem because if a set of parameters is correct, a scaled version is also correct. We can solve this by fixing one parameter of all the reference tissues but also by matching the final part of the curve to a literature AIF.

So, let's have a look at how the AIF we get from the multiple reference tissue method depends on the number of tissues we use. We simulated five reference tissues (using the same procedures as before, with noise and undersampling) with K_{trans} and v_e values of (.1,.35,.4,.5,.7 min^{-1}) and (.1,.21,.3,.4 and .28) where the first two combinations are muscle and liver and the last one is spleen, the other two are random. We then estimated an AIF using all five of these and then 3 AIFs by removing one tissue randomly. We added the v_e of the liver tissue (.21) to the calculation to fix the scale. The results are shown in figure 5.6. We can see that the AIF with 5 reference tissues gives excellent results, but even the three and the four reference tissue AIF give reasonable results. The two reference tissue AIF is worse, but not all that bad. The biggest problem is the underestimation of the peak height, other remarkable things are the shift of the peak maximum (which occurs in all reconstructed AIFs), which is caused by wrong maximum estimation due to the undersampling and lastly we can see obvious noise in the beginning of the AIF caused by noise in the reference tissues. During the analysis of the clinical data we will probably have a maximum of two reference tissues as we can't use the heterogeneity of the tumor to our advantages due to the difficulties in finding ROI's with the same voxel tissue composition. However, what we do see is that this is an excellent method to estimate the AIF in general.

Secondly, we did simulations estimating the AIF from two reference tissues (pectoralis muscle and liver) we simulated with added noise and undersampling and then trying to estimate the tumor parameters. The results are shown in figure 5.7. If we look at the results we can see the bias in K_{trans} is a little higher when compared to simulations using an ideal AIF, probably because the height of the AIF peak is wrong. Secondly, we see that v_e is estimated very well, even better than when we have the perfect AIF, this is probably because some effects cancel each other out (the low temporal resolution effects for example in the last part of the curves of the reference tissues and the tumor curve). The standard deviation of the K_{trans} distribution is approximately equal to the one in the regular simulations (figure 4.15). The 90% confidence intervals for K_{trans} and v_e are 26% and 6% respectively, compared to 16% and 7% when we have the ideal AIF.

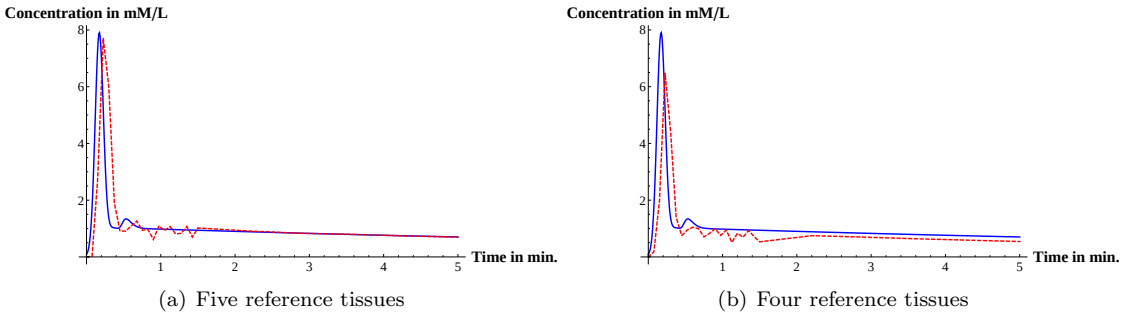

(a) Five reference tissues

(b) Four reference tissues

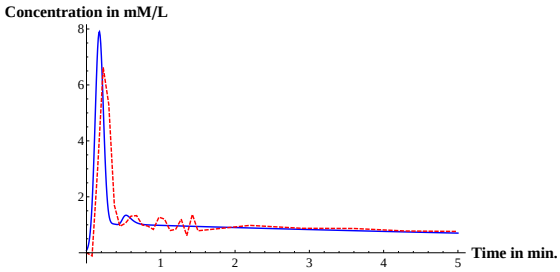

(c) Three reference tissues

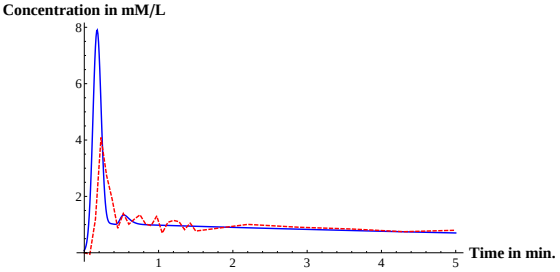

(d) Two reference tissues

Figure 5.6: Reconstructing the AIF using the multiple reference tissue method with different amounts of reference tissue, the solid line is the original AIF, the dotted line the reconstructed AIF

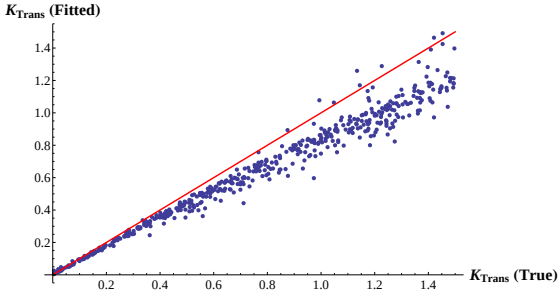

(a) Scatter plot of K_{trans} values, the red line corresponds to real K_{trans} = fitted K_{trans}

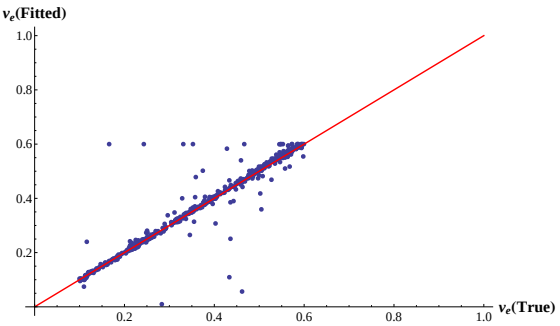

(b) Scatter plot of v_e values, the red line corresponds to real v_e = fitted v_e

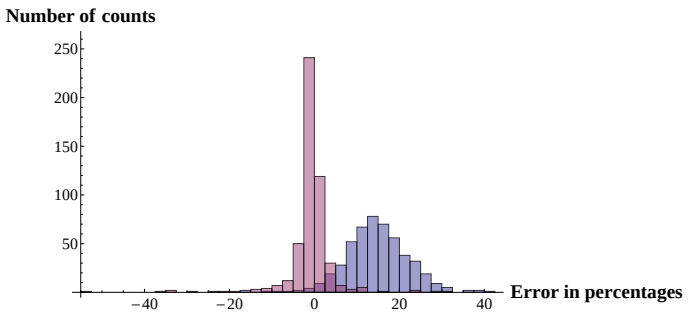

(c) Histogram of the error for K_{trans} (blue bars) and v_e (purple bars) in percentage

Figure 5.7: Scatter plots and the histogram for fitted parameters using the standard Tofts model using the multiple reference tissue method with two reference tissues to estimate the AIF

5.1.4 Conclusion

As we saw in the results for the three different methods, the use of a general population AIF can introduce large errors in the estimate of the tumor parameters. Logically, this is not the first method we would choose to use in the analysis of clinical data. However, we might be able to estimate parameters more accurately if we could fix the height of the first pass in the AIF to a certain value, which could be calculated using a relation between amount of contrast agent injected and the cardiac output of the patient.

The second method we introduced was the estimation of the AIF using a single reference tissue. This is the method of choice when there is one reference tissue available. Errors in this method often are due to wrong estimates for reference tissue parameters, of which the variation among the patient population is unknown. Secondly, errors might occur due to noise in the reference tissue curves, especially in reference tissues with a low enhancement. However, these errors are a lot smaller than the errors that are introduced when using a population averaged AIF.

The third and last method we introduced, the multiple reference tissue method removes the disadvantage of having to know reference tissue parameters by just assuming that multiple reference tissues have the same AIF. This method suffers from the least disadvantages and in addition to not needing to know the reference tissue parameters the use of more reference tissues reduces the effect of noise in the AIF, resulting in a relatively smooth AIF. Problems with this method include the need for multiple reference tissues within the field of view of the tumor, although in some cases parts of the tumor can be used to estimate the AIF. Secondly, the fitting process is not trivial, as erroneous fits do occur. Using correct constraints for your parameters is thus of importance. However, in general this method gives the best results by far, so if there are multiple reference tissues available, this is the method of choice.

Chapter 6

Analysis of clinical data for pharmacokinetic modeling

During this thesis we have suggested several possibilities for handling clinical data in pharmacokinetic modeling. In this chapter we will put the pieces of the puzzle together and use the processes we learned in such a way that we can most reliably handle the data we obtained from the University of Chicago Medical Center.

6.1 Protocol for data analysis

The data analysis can be detailed in a step-by-step protocol, which we followed for all data sets. This finally resulted in pharmacokinetic parameters for each patient or lesion.

1. Load data set into Mathematica including DICOM tags for position and scanning sequence information
2. Use position information to convert low temporal coronal data to low temporal sagittal to match the orientation of the high temporal resolution data (chapter 2)
3. Select a region of interest in the lesion, lesion location was taken from the reports of the radiologist
4. Calculate average ROI $T_1[0]$ in both high and low temporal data using reference tissue method (Chapter 3) to calculate T_1s, using a ROI in fat
5. Compare estimated average tissue $T_1[0]$s (from the previous step) in high and low temporal resolution data to maximize the chance for equal voxel tissue composition. Tweak ROI size to contain only voxels with the same average $T_1[0]$
6. Using information from the DICOM tags (repetition time, flip angle) and the $T_1[0]$ we calculated, using the reference tissue approach, the average ROI concentration over time
7. Use the Taylor expansion of the uncertainty in concentration from chapter 3 (equation 3.15) to estimate standard deviation of the concentration at each time point (the 'noise' in the concentration)
8. Inspect the data set for the possibilities to extract concentration curves of reference tissues using the same procedure as for the lesion curve
9. Fit the concentration curve obtained from step 6 using the standard Tofts model, depending on the amount of reference tissues use either the Parker AIF, a single reference tissue or multiple reference tissue approach to get an input function

10. Calculate the tissue response curve using the AIF and fitted pharmacokinetic parameters found in the previous step and compare this curve with the concentration curve from step 6 to assess fit success.

11. Estimate the uncertainty in the pharmacokinetic parameter estimate. We can use the contour plots (figure 4.20 for K_{trans} for example) and the combination of temporal resolution and uncertainty level to get an individual certainty for each estimate

We followed these steps for every data set, however during the analysis of our data we stumbled across several problems. For one, as we already mentioned in chapter 3, the fact that the orientations of the high and low temporal resolution data do not correspond causes much trouble. It is really hard to find good ROIs (ROIs with the same voxel tissue composition in both high and low temporal data) in these data sets. Secondly, the data is stored in a way that creates extra work, probably because the software used was not developed for gathering dynamic data, as it considers a time point as a slice. This means that slices and time points are stored in one large series of images, which is not intuitive. Thirdly, the time points can only be retrieved through the use of multiple DICOM tags from multiple image sequences within the data sets, which can cause trouble, as some software can not adequately read some of these tags.

For the data in general, sometimes part of the peaks in the rapid initial enhancement are missed because the start and the end of the high temporal series are not chosen adequately. That means we have a lot of unnecessary zero concentration time points at the beginning and a missing part between the low and high temporal resolution parts. This reduces the quality of the fits.

In some data sets the placement of the slices is not optimal for the high temporal series with slices bordering the edges of the tumor instead of one slice clearly on the tumor. In two cases the tumor was completely missed in the high temporal series, making these data sets not useable.

So, summarizing, we have some pointers for acquisition of high temporal resolution clinical data sets in the future:

- Use the same orientation for acquisition of the low and high temporal resolution data sets, if possible with the same resolution and slice thicknesses, to maximize voxel tissue composition similarity
- High temporal resolution is more important than noise on average, so put emphasis on that. Reducing number of averages or field of view is an option to increase scanning speed
- Try to have at least one tissue in the field of view that can be used as a reference tissue
- Measure patient blood pressure and heart rate during the scan so if no useable reference tissue is available the population AIF peak height can be fixed to a specific value to minimize errors
- Scan the patient in combination with a reference phantom or, if scan time allows this, make a $T_1[0]$ map of the breast to allow for simple $T_1[0]$ estimation.
- Introduce a standardized system for data storage for high temporal DCE MRI within the DICOM standard, to make reading of the images easier
- Make sure the entire fast initial enhancement falls within the high temporal sequence, 90 seconds is enough but timing of the start of the sequence is important.

6.2 Results of patient data fitting

Data sets that did not have any problems resulted in quite adequate fits, some examples are shown in figures 6.1, 6.2 and 6.3. The results for all data sets (we got fits for) are shown in table 6.1 Interpreting these results is not easy, because of the large uncertainties contained within them. In the table you can find the calculated values with their 90% confidence intervals. Do keep in mind that the errors caused by wrong estimation of the AIF and the neglecting of other pharmacokinetic

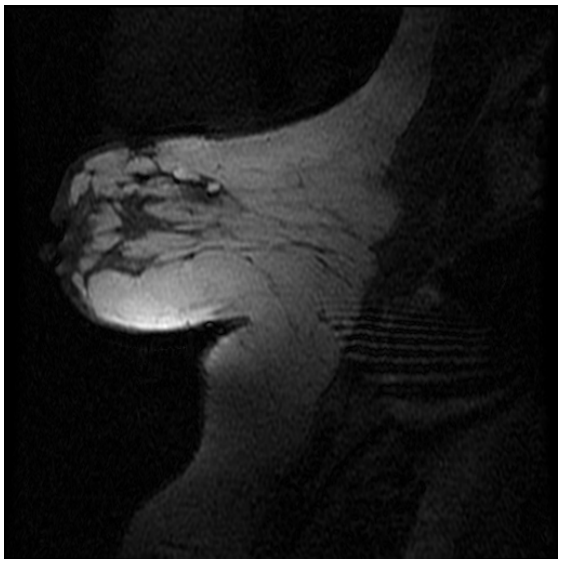

(a) Precontrast slice

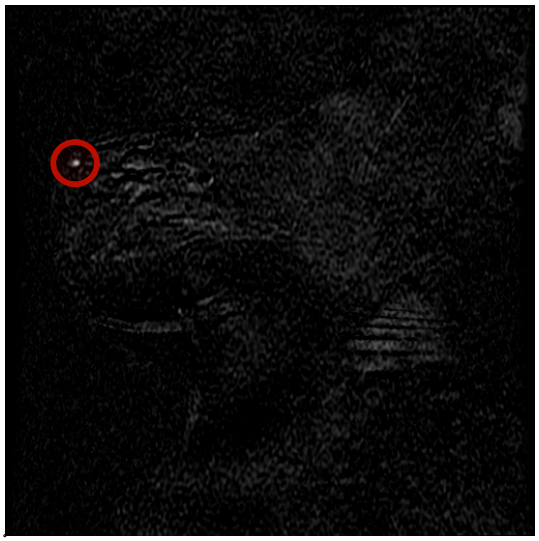

(b) Difference image postcontrast - precontrast, finding encircled

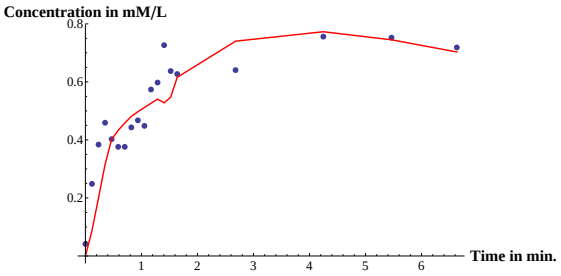

(c) Fit of patient 0098

Figure 6.1: Images and fit for patient 0098

Patient Number	K_{trans}	v_e	AIF	Lesion type
0010	.34 ± .05	.55 ± .04	Pop	high grade DCIS
0032	.65 ± .1	.54 ± .04	Ref (Muscle)	grade 3 IDC
0098	.17 ± .03	.47 ± .05	Ref (Muscle)	Benign
0441	.24 ± .04	.51 ± .04	Pop	Low-grade DCIS
0557	.10 ± .02	.64 ± .05	Pop	Benign
0640	.41 ± .06	.34 ± .02	Pop	grade 2 IDC
0793	.22 ± .04	.57 ± .04	Ref (Liver)	grade 2 IDC
0822	.27 ± .05	.75 ± .05	Pop	DCIS
1102	.28 ± .06	.53 ± .04	Pop	Malignant
1121	.51 ± .08	.29 ± .02	Pop	Malignant
1160	.23 ± .04	.40 ± .03	Pop	grade 1 IDC
1185	.26 ± .05	.33 ± .02	Pop	grade 2 IDC
1440	.12 ± .02	.34 ± .03	Pop	DCIS
1526	.06 ± .01	.18 ± .01	Pop	Benign

Table 6.1: Results of patient data fitting using the standard Tofts model

parameters are not contained in this interval. If we then pool them together in a table for special types of cancer and malignant / benign, where we consider DCIS to be malignant for the moment

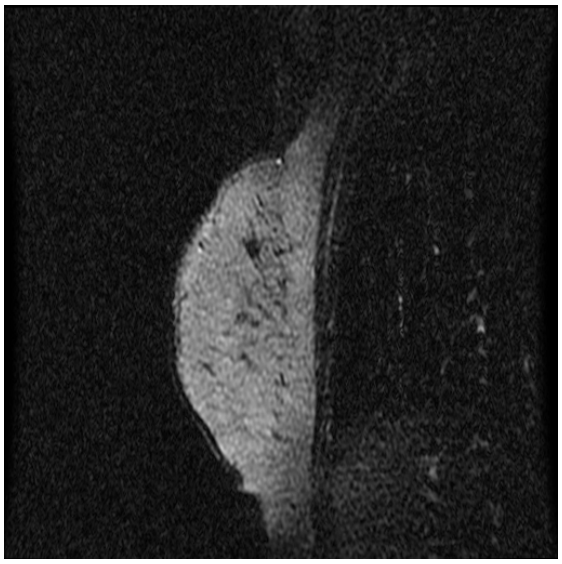

(a) Precontrast slice

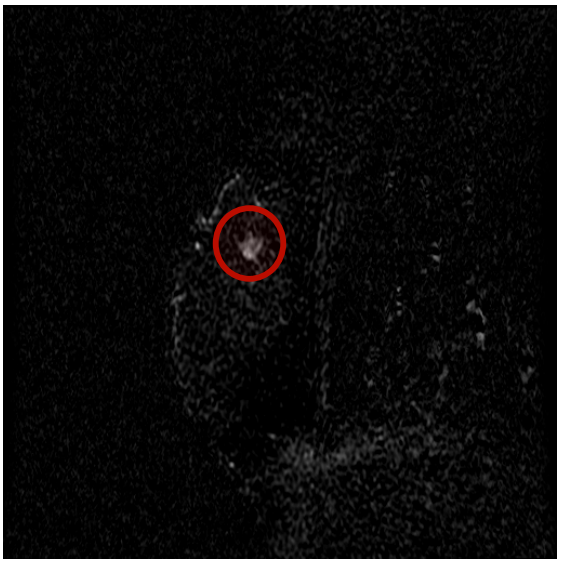

(b) Difference image postcontrast - precontrast, finding encircled

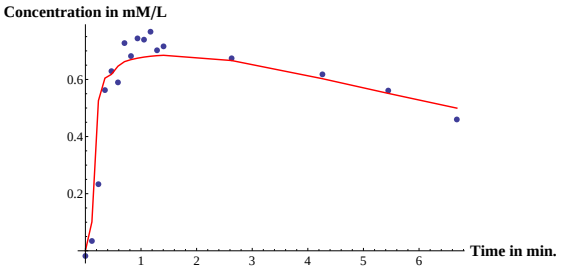

(c) Fit of patient 1185

Figure 6.2: Images and fit for patient 1185

we get the results in table 6.2. This table offers a little more insight. There is some evidence

Type	$\mathbf{K}_{\text{trans}}$	$\mathbf{v_e}$
IDC (5)	.35 ± .18	.40 ± .1
DCIS (4)	.24 ± .1	.54 ± .16
Other (2)	.40 ± .16	.41±.17
Grade 1 (2)	.24 ± .04	.45 ± .1
Grade 2 (3)	.30 ± .1	.41 ± .13
Grade 3 (2)	.45 ± .28	.54±.02
Malignant (11)	.32 ± .15	.45 ± .15
Benign (3)	.11 ± .06	.43 ± .23

Table 6.2: Results of patient data fitting using the standard Tofts model, categorized by lesion type. The first part of the table categorizes lesions by type and gives the average parameter values, the second part categorizes lesions by shape and the third part by malignant/benign

that malignant and benign lesion might be separable by pharmacokinetic parameters, especially K_{trans} being higher in malignant lesions. We do not see any difference in v_e. However, we have very little data, so coming to a real conclusion is not possible. If more data sets are acquired in the future then we might be able to do an accurate and statistically sound analysis. If we look at

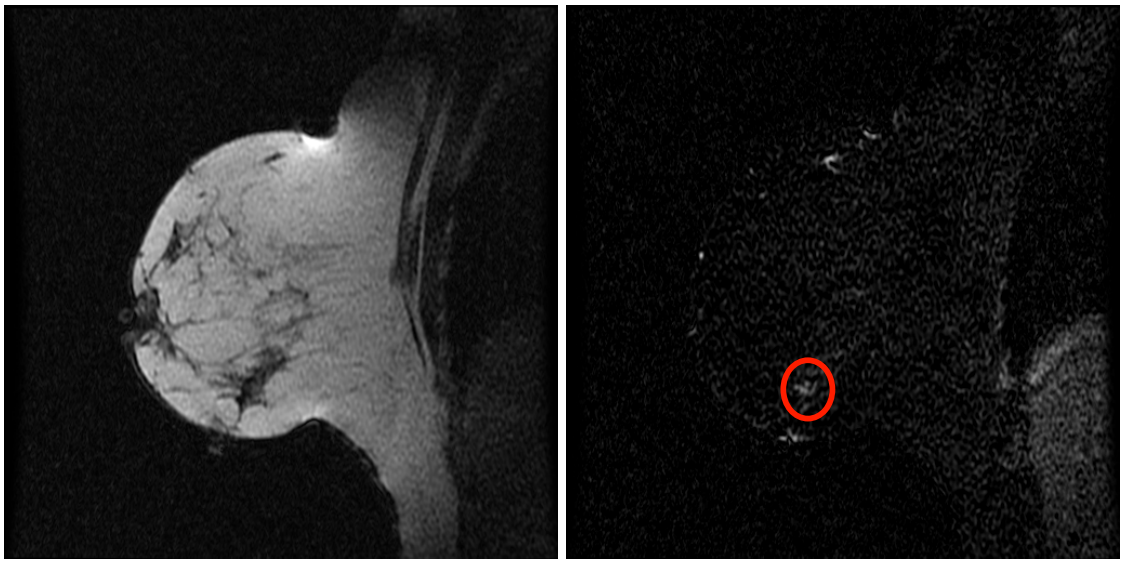

(a) Precontrast slice

(b) Difference image postcontrast - precontrast, finding encircled

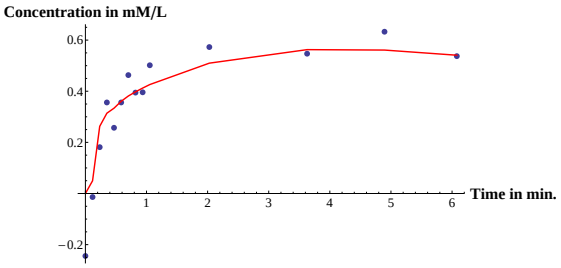

(c) Fit of patient 1440

Figure 6.3: Images and fit for patient 1440

the lesion or grade type differentiation we can say that we have no evidence that different types of cancer can be separated using pharmacokinetic parameters, although we need more data to make sure of that.

What we can do at the moment is compare the values we found to literature. There are some studies that have investigated the pharmacokinetic parameters in different types of cancer, for example by Hulka et al[14], who found values for benign tissue K_{trans} of .17 ± .11 and malignant tissue K_{trans} of .45 ± .22. Another investigation was done by Eliat et al[10], they found for 59 malignant and 41 benign cases values of $K_{\text{trans}} = .35 \pm .29$, v_e=.43 ± .22 and $K_{\text{trans}} = .14 \pm .18$, v_e=.49 ± .29 for malignant and benign respectively. These results agree with ours, so that it is positive sign for the diagnostic potential of pharmacokinetics.

6.2.1 Conclusion

Summarizing, we can say that analyzing the data was definitely not an easy task. Numerous problems quickly dwindled the amount of data that we had available. However, the data we do have left showed some interesting trends, which correspond with what we see in other studies. In the future, when more data is available, further research can be done into the diagnostic potential of the pharmacokinetic parameters and in the characteristics of specific cancer types.

Chapter 7

Discussion, conclusion and future work

Now that we are nearing the end of this thesis, it is useful to discuss the research we presented in this thesis, to find points that can be improved and to look if we answered the questions we had at the beginning of this thesis. In general we wanted to know what the most accurate way was to extract concentration curves from the clinical data we obtained from the university of Chicago Medical Center, secondly we wanted to know what pharmacokinetic model to use for these types of data, thirdly we wanted to know what options we have in estimating the AIF, lastly we wanted to know if the pharmacokinetic parameters we obtained from the lesion in our clinical data would allow for analysis on the diagnostic potential of such parameters.

Let's start with the data and data acquisition, which we discussed both in chapter 2 and chapter 6. The data we had was acquired some time ago at the University of Chicago Medical Center. During the viewing and analysis of the data, we discovered some imperfections. The most important one was the difference in orientation of the high and low temporal resolution data, which, due to the large difference in slice thickness and spatial resolution, often lead to different voxel tissue composition. Secondly, in some cases the data was not useable, sometimes due to misalignment of the high temporal resolution sequence with the tumor position, sometimes because a part of the fast initial enhancement was missed in the high temporal resolution sequence. The temporal resolution and image quality per se was high enough to allow reasonably accurate fitting of the standard Tofts model. In the future an effort should be made to acquire data at an even higher temporal resolution in which it is important that images are in the same orientation.

When we started to analyse the data sets our first step was to estimate the concentration of contrast agent from MR signal intensities, which is not a trivial matter. We investigated several approaches used in literature and concluded that the often occurring neglect of the T_{2^*} was allowed. After this we delved into the proces of estimating $T_1[0]$, which we tried to do from the data itself, without extra measurements. We investigated the use of a reference tissue or phantom as a means of $T_1[0]$ estimation and the experiments using the phantom proved hopeful, as our abstract to the RSNA about this subject was accepted. In the future it is necessary to look into the assumption that proton density differences within the breast are negligibly small and if this assumption is proven to be invalid, to look into an alternative, for example a look-up-table. The last part of that chapter was research into the effects of simplifying the gradient-echo formula further, which is often done in research. However, we found no reason to do this, as the function itself is easy to calculate using a computer and the simplification introduces extra errors. At the end we put all the uncertainties we encountered during the conversion to concentration together and, using a Taylor expansion of the uncertainty in the concentration, find the final uncertainty in the concentration for each time point. In the future further investigation can be done into the effect of flip angle errors and relaxivity constant uncertainties.

The second part of this thesis was investigation in pharmacokinetic modeling and models. In

literature at the moment there are literally a dozen of different models and model adaptations. We tried to pick a nice representative subset of these to show what kind of models are useable on clinical data. We choose to evaluate three pharmacokinetic models and the shutter speed model, which itself uses the standard Tofts model. We believe these models represent a good overview of the physiological processes that underly pharmacokinetics. As we saw immediately in chapter 4, if we have perfect data the fits of the models were generally good. The Brix model was the least performing model, already an indication that for clinically relevant values of F that parameter had little measurable influence. When we moved from simulated perfect data to simulated clinical data we immediately saw that almost all models except the standard Tofts model had major difficulties in accurately fitting their extra parameters, v_p in the extended Tofts model, τ_i in the shutter speed model and F and v_p in the Brix model. We also saw that there was some value dependent bias in parameters like K_{trans} , which made analysis of the error a little more difficult. However, if we would assume no knowledge of the parameters beforehand, we can just analyse the error distributions of these parameters and use those to say something about the models in general. What we saw is that the standard Tofts model reaches clinically acceptable confidence intervals for relatively low temporal resolution, even sample rates of 9 seconds are still reasonable (compared to the other models) and later on that small errors induced by neglecting v_p, F and τ_i do not increase the error substantially. However, if one expects large influences from one of these parameters, effort should be put into increasing temporal resolution to enable the use of the more complex models. In clinical data however, the more complex models seem to have no real use as of yet, due to the large uncertainty in the extra variables the induce, so we stick with the standard Tofts model. We should take note however that these observations are based on the general behavior of the model. If we look at for example the error in K_{trans} we can see that it increases with increasing K_{trans} at low temporal resolution. Thus if it is known beforehand that we are likely to encounter low values of K_{trans} for example, then maybe less stringent demands on temporal resolution are allowed. In the future this kind of research can be expanded with extra models (St. Lawrence and Lee model, Shutter speed second generation) or with different data effects that occur, for example difference in bolus arrival time and temporal jitter. Also the contour plots can be made more accurately using more measurement points along the noise and sampling rate axes. Also emphasis should be put on estimating correct parameter ranges for tumors so simulations can be run more accurately.

The fitting algorithm we used might also be a point of discussion. We decided to use the Nelder Mead Global Minimization algorithm, which gave us a good balance between speed and accuracy. However, if one would be willing to give starting values, the same results might be achieved using a local minimization method, which likely will be faster. On the other end, if time is not an issue we can also use more advanced minimization techniques, or the method of random search, which is simply using the local minimization techniques at several starting values. Those methods might increase accuracy and thus reduce the requirements on the data. However it is our belief that if models are to be used in a clinical setting time is an important factor. A radiologist simply does not have the time to wait for the fitting procedure to be completed. That is why we choose to find a method that is somewhere in between. Future researchers could investigate other fitting methods.

In chapter 5 we investigated the measurement or calculation of the arterial input function, which is a field of research in itself. In general there are five methods, however the invasive drawing of blood and the direct measurement from large arteries using MRI both have severe problems and limitations. We investigated three alternative methods, the use of a population averaged or mathematical AIF, the use of a reference tissue or the use of multiple reference tissues. We quickly saw that the variability in the AIF between individuals and between measurements can be quite large and that these errors can easily propagate into the estimates of your pharmacokinetic parameters. The use of the population averaged AIF was thus considered a last resort, however, accuracy could probably be increased if we are able to fix the first pass peak height at a certain value, using measurements for cardiac output, for example heart rate and blood pressure. The second option was the use of a single reference tissue, which has the advantage of giving you a measurement specific input function. However, this means that noise will have a larger influence

on your data, as your AIF is estimated from noisy data, which we saw had an effect on the standard deviation of the error distribution of our parameters. An added risk is the possibility to introduce large errors by giving wrong values for reference tissue pharmacokinetic parameters. If this method is really useable depends greatly on those values and in the future researchers should try to find an answer to the question if there is a large variability. The last method we looked at was the multiple reference tissue method, which was able to give rather accurate AIFs, however, it requires much input. If it is possible in data sets to segment the tumor in multiple homogenous sections, then this is the method of choice, because it gives by far the best AIF estimate, thus limiting the error caused by wrong AIF estimation.

The last chapter, chapter 6, was the chapter where we had to put everything together. However, due to data limitations and just empty data sets our stock of 42 datasets went down to a smaller number. Thus, it is difficult to draw any real conclusion from the data, although it seems that there is an indication that benign tissues and malignant tissues might be separable by using pharmacokinetic parameters. The question wether or not this is really true or just a coincidental observation has to be looked at in the future. At that time, one may also be able to answer the question wether there is a possibility to separate different types of tumors using clustering based on pharmacokinetic parameters.

All in all we hope to have given you a thorough overview about the pharmacokinetic field in breast MRI and hopefully we helped to attribute to your insight in the matter.

Bibliography

[1] American Cancer Society. Breast Cancer Death Rates Continue to Decline. `http://www.cancer.org/docroot/NWS/content/NWS_1_1x_Breast_Cancer_Death_Rates_Continue_To_Decline.asp`, 2008.

[2] N. Boulant and D. Le Bihan. Strongly modulating pulses for counteracting RF inhomogeneity at high fields . *Magnetic Resonance in Medicine*, 60, 2008.

[3] G. Brix, M. Bahner, and U. Hoffman et al. Regional Blood Flow, Capillary Permeability, and Compartmental Volumes: Measurement with Dynamic CT—Initial Experience1. *Radiology*, 210, 1999.

[4] G. Brix, F. Kiessling, and R. Lucht. Microcirculation and Microvasculature in Breast Tumors: Pharmacokinetic Analysis of Dynamic MR Image Series. *Magnetic Resonance in Medicine*, 52, 2004.

[5] A. Buades and B. Coll. A review of image denoising algorithms. *Multiscale Modelling and Simulation*, 4, 2005.

[6] J. Bushberg, J. Seibert, and J. Boone. *The essential physics of medical imaging.* Lippincot, Williams and Wilkins, 2001.

[7] H. Daldrup and D. Shames et al. Quantification of the extraction fraction for gadopentetate across breast cancer capillaries. *Magnetic Resonance in Medicine*, 40, 2005.

[8] D.Balvay and Y. Ponnvainne et al. ArterialL Input Function: Relevance Of Eleven Analytical Models In DCE-MRI Studies. *Biomedical Imaging: From Nano to Macro, 5th IEEE International Symposium on*, 14, 2008.

[9] N. Dowell and P. Tofts. Fast, accurate, and precise mapping of the RF field in vivo using the 180 degree signal null. *Magnetic Resonance in Medicine*, 58, 2007.

[10] P. Eliat and V. Dedieu. Magnetic resonance imaging contrast-enhanced relaxometry of breast tumors: an MRI multicenter investigation concerning 100 patients. *Magnetic Resonance Imaging*, 22, 2004.

[11] X. Fan and M. Medved. Diagnosis of suspicious breast lesions using an empirical mathematical model for dynamic contrast-enhanced MRI. *Magnetic Resonance Imaging*, 25, 2007.

[12] M. Heisen. Considerations regarding pharmacokinetic analysis of dce-mr breast images. Master's thesis, Eindhoven University of Technology, 2007.

[13] J. Hornak. *The Basics of MRI.* `http://www.cis.rit.edu/htbooks/mri/`, 2008.

[14] C. Hulka and B.Smith et al. Benign and malignant breast lesions: Differentiation with echoplanar MR imaging. *Radiology*, 197, 1995.

[15] A. Iserless. *NA First Course in the Numerical Analysis of Differential Equations.* Cambridge University Press, 1996.

[16] C. Jaque and A. Bera. Efficient tests for normality, homoscedasticity and serial independence of regression residuals. *Economic Letters*, 6, 1980.

[17] S. Kety. The theory and applications of the exchange of inert gas at the lungs and in tissue. *Pharmacological review*, 3, 1951.

[18] D. Kovar and M. Lewis et al. A new method for imaging perfusion and contrast extraction fraction: input functions derived from reference tissues. *Journal of Magnetic Resonance Imaging*, 8, 1998.

[19] C. Kuhl. Dynamic breast mr imaging: are signal intensity time course data useful for differential diagnosis of enhancing lesions? *Radiology*, 211, 1999.

[20] C. Kuhl. The current status of breast mr imaging. *Radiology*, 244(2), August 2007.

[21] KWF Kankerbestrijding. Feiten en cijfers. `http://www.kwfkankerbestrijding.nl/index.jsp?objectid=17060`, 2008.

[22] H. Larsson and M. Stubgaard et al. Quantitation of blood-brain barrier defects using by magnetic resonance imaging and gadolinium-DTPA in patients with multiple sclerosis and brain tumors. *Magnetic Resonance in Medicine*, 16, 1990.

[23] R.B. Laufer. Paramagnetic metal complexes as water proton relaxation agents for NMR imaging: theory and design. *Chem. Rev.*, 87, 1987.

[24] K.S. St Lawrence and T.Y. Lee. An adiabatic approximation to the tissue homogeneity model for water exchange in the brain: I. Theoretical derivation. *Cerebral Bloodflow and Metabolism*, 18, 1998.

[25] D. Levitt. PKQuest: a general physiologically based pharmacokinetic model. Introduction and application to propranolol. *BMC Clinical Pharmacology*, 2, 2002.

[26] X. Li and W. Rooney et al. A Unified Magnetic Resonance Imaging Pharmacokinetic Theory: Intravascular and Extracellular Contrast Reagents. *Magnetic Resonance in Medicine*, 54, 2005.

[27] J. Manjón. MRI Denoising using Non-Local Means. *Medical Image Analysis*, 12, 2008.

[28] R. Mann and C. Kuhl. Breast MRI: guidelines from the European Society of Breast Imaging. *European Radiology*, 18, 2008.

[29] M. Medved, G. Karczmar, and C. Yang. Semiquantitative Analysis of Dynamic Contrast Enhanced MRI in Cancer Patients: Variability and Changes in Tumor Tissue Over Time. *Journal of Magnetic Resonance Imaging*, 20, 2004.

[30] M. Morales and R. Smith. On the theory of blood-tissue exchange of inert gases. VI. Validity of approximate uptake expressions. *Mathematical Biophysics*, 10, 1948.

[31] R. Murray, J. Dowdy, and E. Christensen. *Christensen's physics of diagnostic radiology.* Lippincot, Williams and Wilkins, 1990.

[32] National Electrical Manufacturers Association. The DICOM Standard. `http://medical.nema.org/`, 2008.

[33] National Institute of Health. Breast Cancer. `http://www.nlm.nih.gov/medlineplus/ency/article/000913.htm`, 2008.

[34] J. Nelder and R. Mead. A simplex method for function minimization. *Computer Journal*, 7, 1965.

[35] R. Nowak. Wavelet-Based Rician Noise Removal for Magnetic Resonance Imaging. *IEEE Transactions On Image Processing*, 8, 1999.

[36] L. Nystrøm and L.E. Rutqvist. Breast cancer screening with mammography. *The Lancet*, 360 (9329):338–339, 1993.

[37] M. Orton and J. D'Arcy et al. Computationally efficient vascular input function models for quantitative kinetic modelling using DCE-MRI. *Physics in Medicine and Biology*, 53, 2008.

[38] A. Padhani and C. Hayes et al. Computationally efficient vascular input function models for quantitative kinetic modelling using DCE-MRI. *NMR in Biomedicine*, 15, 2002.

[39] A. Papoulis. *Probability, Random Variables, and Stochastic Processes*. McGraw-Hill, 1991.

[40] G. Parker and C. Roberts et al. Experimentally-Derived Functional Form for a Population-Averaged High-Temporal-Resolution Arterial Input Function for Dynamic Contrast-Enhanced MRI. *Magnetic Resonance in Medicine*, 56, 2006.

[41] C. Patlak, J. Fenstermacher, and R. Blasberg. Graphical evaluation of blood-to-brain transfer constant from multiple-time-uptake data. *Cerebral Bloodflow and Metabolism*, 3, 1983.

[42] C. Planey and E.B. Welch. Temporal Sampling Requirements for Reference Region Modeling of DCE-MRI Data in Human Breast Cancer. *Journal of Magnetic Resonance Imaging*, 30, 2009.

[43] W. Press and B. Flannery et al. *Numerical Recipes in C*. Cambridge University Press, 1988.

[44] *Comparison of T1 measurements by means of TurboFLASH techniques performed on a conventional whole-body MR imager*, volume 12, 1993. Proceedings SMRM.

[45] P.Tofts and B. Shuter. Ni-DTPA doped agarose gel a phantom material for Gd-DTPA enhancement measurements. *Magnetic Resonance Imaging*, 11, 1993.

[46] R. Rakow-Penner and B. Daniel. Relaxation times of breast tissue at 1.5T and 3T measured using IDEAL. *Journal of Magnetic Resonance Imaging*, 23, 2005.

[47] J. Sijbers and A.J. den Dekker. Maximum Likelihood Estimation of Signal Amplitude and Noise Variance From MR Data. *Magnetic Resonance in Medicine*, 51, 2004.

[48] W. Smith. *Foundations of Materials Science and Engineering*. McGraw-Hill, 2004.

[49] F. Tavossoli and P. Devilee. World health organization classification of tumours. Pathology and genetics of tumours of the breast and female genital organs. *IARC Press*, 2003.

[50] P. Tofts. *Quantitative MRI of the Brain: Measuring Changes Caused by Disease*. John Wiley and Sons, 2003.

[51] P. Tofts and B. Berkowitz et al. Quantitative analysis of Dynamic Gd-DTPA Enhancement in Breast Tumors using a Permeability Model. *Magnetic Resonance in Medicine*, 33, 1995.

[52] P. Tofts and G. Brix et al. Estimating kinetic parameters from dynamic contrast-enhance t1-weighted mri of a diffusable tracer: Standardizing quantities and symbols. *Journal of Magnetic Resonance Imaging*, (10), 1999.

[53] B.F. Vianio. *IARC Handbooks of Cancer Prevention: Breast Cancer Screening*. IARC (Internatiol Agency of Research on Cancer), 2002.

[54] Wolfram. Wolfram mathematica. `http://www.wolfram.com`, 2008.

[55] World Health Organisation. Factsheet N297: Cancer. `http://www.who.int/mediacentre/factsheets/fs297/en/index.html`, 2008.

[56] C. Yang and G. Karczmar et al. Estimating the Arterial Input Function Using Two Reference Tissues in Dynamic Contrast-Enhanced MRI Studies: Fundamental Concepts and Simulations. *Magnetic Resonance in Medicine*, 52, 2004.

[57] C. Yang and G. Karczmar et al. Multiple Reference Tissue Method for Contrast Agent Arterial Input Function Estimation. *Magnetic Resonance in Medicine*, 58, 2007.

[58] C. Yang, G. Karczmar, and M. Medved. Reproducibility Assessment of a Multiple Reference Tissue Method for Quantitative Dynamic Contrast Enhanced–MRI Analysis. *Magnetic Resonance in Medicine*, 61, 2009.

[59] T. Yankeelov and J. Luci et al. Quantitative pharmacokinetic analysis of DCE-MRI data without an arterial input function: a reference region model. *Magnetic Resonance Imaging*, 23, 2005.

[60] T. Yankeelov, C. Springer, W. Rooney, and X. Li. Variation of the Relaxographic "Shutter-Speed" for Transcytolemmal Water Exchange Affects the CR Bolus-Tracking Curve Shape. *Magnetic Resonance in Medicine*, 50, 2003.

Appendix A

Patient Data

Patient Nr.	Age	TR (High/Low)	FA (High/Low)	Position	Enhancement	K_{trans}	v_e	AIF	Lesion type
0010	53	8.9/7.5	30/30	Left, 7 o'Clock	Rapid,Plateau	.34 ± .05	.55 ± .04	Pop	high grade DCIS
0032	46	8.9/7.7	30/30	Left, Central	Rapid,Washout	.65 ± .1	.54 ± .04	Ref (Muscle)	grade 3 IDC
0098	55	8.9/7.6	30/30	Left, 12 o'Clock	Medium,Persistent	.17 ± .03	.47 ± .05	Ref (Muscle)	Benign
0441	57	8.9/7.7	30/30	Right, 9 o'Clock	Rapid,Persistent	.24 ± .04	.51 ± .04	Pop	Low-grade DCIS
0557	48	8.9/7.6	30/30	Right, Central	Rapid,Persistent	.10 ± .02	.64 ± .05	Pop	Benign
0640	39	8.9/7.6	30/30	Right, 3 o'Clock	Rapid,Washout	.41 ± .06	.34 ± .02	Pop	grade 2 IDC
0793	43	8.9/7.7	30/30	Right, 1 o'Clock	Rapid,Washout	.22 ± .04	.57 ± .04	Ref (Liver)	grade 2 IDC
0822	47	8.9/7.6	30/30	Right	Rapid,Plateau	.27 ± .05	.75 ± .05	Pop	DCIS
1102	85	8.9/7.6	30/30	Left, 3 o'Clock	Rapid,Washout	.28 ± .06	.53 ± .04	Pop	Malignant
1121	36	8.9/7.6	30/30	Right, 1 o'Clock	Rapid,Washout	.51 ± .08	.29 ± .02	Pop	Malignant
1160	48	8.9/7.6	30/30	Left, 5 o'Clock	Rapid,Washout	.23 ± .04	.40 ± .03	Pop	grade 1 IDC
1185	67	8.9/7.7	30/30	Right, 12 o'Clock	Rapid,Washout	.26 ± .05	.33 ± .02	Pop	grade 2 IDC
1440	58	8.9/7.7	30/30	Right, 6 o'Clock	Rapid,Persistent	.12 ± .02	.34 ± .03	Pop	DCIS
1526	58	8.9/7.72	30/30	Left	Medium,Plateau	.06 ± .01	.18 ± .01	Pop	Benign

Table A.1: Patient data: Age, TR, Flip angle are obtained from DICOM tags. Position, enhancement and lesion type are from the radiological report. K_{trans} , v_e and AIF are determined in this report

Appendix B

Abstract RSNA

Authors

G Litjens, BS; M Heisen, MSC; J Buurman, PhD; A M Wood, BS; M Medved, PhD; G S Karczmar, PhD; B.M. Ter Haar - Romeny, PhD.

Purpose

For standardized interpretation of DCEMRI curves, calculation of contrast agent (CA) concentration from signal intensity over time is desired. Accurate measurement of tissue T1 before and after CA administration is thus necessary. Current T1 measurement methods are time-consuming. We propose the use of the 'reference tissue' method [Medved et al. JMRI 20(1):122, 2004] for fast T1 measurements concurrent with DCEMRI data acquisition, but with use of a reference phantom.

Method and materials

The 'reference tissue' method is based on the approximation that in T1-weighted gradient echo images, signal intensity is proportional to 1/T1 – thus signal intensity can be referenced to a tissue or a phantom with a known T1. We compared this method to the 'variable flip angle' method, most commonly used in clinical practice. We compared the 'reference tissue' method (TR/TE = 25/1.1 ms, a=40°) to the 'variable flip angle' method (TR/TE = 25/1.1 ms, a=3/5/10/15/20/25/30/35/40°), using the Eurospin T05 phantom, in which 10 out of 18 vials containing agar with varying concentrations of Gd-DTPA (T1 range: 281 – 1384 ms) were used.

Results

With the 'reference tissue' method, using 9 tubes successively as a reference for the remaining tube, the average error in the estimation of T1 was 8.5%, with a standard deviation of 6.1%, and was random. Using the 'variable flip angle' method, the average error was 5.7 % with a standard deviation of 3.8%. Using a two-sided Student's t-test we found no statistically significant differences in the performance of the two methods (p-value = 0.52).

Conclusion

As DCEMRI imaging is done in a heavily T1-weighted regime, the 'reference tissue' method can be used to concurrently measure T1, and quantify CA concentration. Use of an agar phantom will require a correction for lower proton density in biological tissue. Proton density can be measured prior to CA administration, or tabulated values can be used. We demonstrated the feasibility of fast T1 measurements using a reference phantom, providing T1 maps without additional scanning time. This will allow quantification of the CA concentration throughout the DCEMRI scan, which cannot be achieved using the current clinical method.

Clinical Relevance/Application

The use of a reference phantom for determining T1 can lead to a drastic reduction in scanning time and thus patient discomfort when compared to a regular clinical 'variable flip angle' scan.

Appendix C

Extended Mathematics

Full concentration uncertainty formulae

For σ_{C_t} we can write using equation 3.15 and 3.8 we can write out the complete formula, were we write $S_{t/0}$ as S:

$$\sigma_{C_t}^2 = \left(-\frac{\left(-1+e^{R_1[0]\mathrm{TR}}\right)^2 (-1+S) S \mathrm{Sin}[\theta]}{\mathrm{r1TR}\left(e^{R_1[0]\mathrm{TR}}(-1+S)-S+\mathrm{Cos}[\theta]\right)\left(-(-1+S)\mathrm{Cos}[\theta]+e^{R_1[0]\mathrm{TR}}(-1+S\mathrm{Cos}[\theta])\right)} \right)^2 \sigma_\theta^2 + \left(-\frac{\mathrm{Log}\left[\frac{e^{-R_1[0]\mathrm{TR}}\left(-(-1+S)\mathrm{Cos}[\theta]+e^{R_1[0]\mathrm{TR}}(-1+S\mathrm{Cos}[\theta])\right)}{e^{R_1[0]\mathrm{TR}}(-1+S)-S+\mathrm{Cos}[\theta]}\right]}{\mathrm{r1}^2\mathrm{TR}} \right)^2 \sigma_{r_1}^2 + \left(-\frac{(-1+S)\left(-e^{2R_1[0]\mathrm{TR}}+\left(-2e^{R_1[0]\mathrm{TR}}(-1+S)+S+e^{2R_1[0]\mathrm{TR}}S\right)\mathrm{Cos}[\theta]-\mathrm{Cos}[\theta]^2\right)}{\mathrm{r1}\left(e^{R_1[0]\mathrm{TR}}(-1+S)-S+\mathrm{Cos}[\theta]\right)\left(-e^{R_1[0]\mathrm{TR}}+\left(1+\left(-1+e^{R_1[0]\mathrm{TR}}\right)S\right)\mathrm{Cos}[\theta]\right)} \right)^2 \sigma_{R_1[0]}^2 + \left(\frac{1}{\mathrm{r1TR}\left(\frac{1}{-1+e^{R_1[0]\mathrm{TR}}}+\frac{S^2\mathrm{Cos}[\theta]}{-e^{R_1[0]\mathrm{TR}}+\mathrm{Cos}[\theta]}-\frac{(-1+S)(-1+S\mathrm{Cos}[\theta])}{-1+\mathrm{Cos}[\theta]}\right)} \right)^2 \sigma_S^2$$

For the standard deviation in $S_{t/0}$ we refer to equation 3.16. Now for the complete uncertainty formula for $\sigma_{R_1[0]}^2$ we can use the same procedure but now using 3.17 and 3.11 and S_{rel} is written

as S:

$$\sigma^2_{R_1[0]} =$$
$$\left(\left(\left(-1+e^{\frac{\mathrm{TR}}{\mathrm{T1Ref}}}\right)^2(-1+S)S\mathrm{TRSin}[\theta]\right)/\left(e^{\frac{\mathrm{TR}}{\mathrm{T1Ref}}}(-1+S)-S+\mathrm{Cos}[\theta]\right)\right.$$
$$\left.\left(-(-1+S)\mathrm{Cos}[\theta]+e^{\frac{\mathrm{TR}}{\mathrm{T1Ref}}}(-1+S\mathrm{Cos}[\theta])\right)\mathrm{Log}\left[\frac{-(-1+S)\mathrm{Cos}[\theta]+e^{\frac{\mathrm{TR}}{\mathrm{T1Ref}}}(-1+S\mathrm{Cos}[\theta])}{e^{\frac{\mathrm{TR}}{\mathrm{T1Ref}}}(-1+S)-S+\mathrm{Cos}[\theta]}\right]^2\right)^2$$
$$\sigma^2_\theta +$$
$$\left(\left(\left(-1+e^{\frac{\mathrm{TR}}{\mathrm{T1Ref}}}\right)^2(-1+S)S\mathrm{TRSin}[\theta]\right)/\left(e^{\frac{\mathrm{TR}}{\mathrm{T1Ref}}}(-1+S)-S+\mathrm{Cos}[\theta]\right)\right.$$
$$\left.\left(-(-1+S)\mathrm{Cos}[\theta]+e^{\frac{\mathrm{TR}}{\mathrm{T1Ref}}}(-1+S\mathrm{Cos}[\theta])\right)\mathrm{Log}\left[\frac{-(-1+S)\mathrm{Cos}[\theta]+e^{\frac{\mathrm{TR}}{\mathrm{T1Ref}}}(-1+S\mathrm{Cos}[\theta])}{e^{\frac{\mathrm{TR}}{\mathrm{T1Ref}}}(-1+S)-S+\mathrm{Cos}[\theta]}\right]^2\right)^2$$
$$\sigma^2_{\mathrm{T1Ref}} +$$
$$\left(\left(\left(-1+e^{\frac{\mathrm{TR}}{\mathrm{T1Ref}}}\right)\mathrm{TR}\left(e^{\frac{\mathrm{TR}}{\mathrm{T1Ref}}}-\mathrm{Cos}[\theta]\right)(-1+\mathrm{Cos}[\theta])\right)/\left(e^{\frac{\mathrm{TR}}{\mathrm{T1Ref}}}(-1+S)-S+\mathrm{Cos}[\theta]\right)\right.$$
$$\left.\left(-(-1+S)\mathrm{Cos}[\theta]+e^{\frac{\mathrm{TR}}{\mathrm{T1Ref}}}(-1+S\mathrm{Cos}[\theta])\right)\mathrm{Log}\left[\frac{-(-1+S)\mathrm{Cos}[\theta]+e^{\frac{\mathrm{TR}}{\mathrm{T1Ref}}}(-1+S\mathrm{Cos}[\theta])}{e^{\frac{\mathrm{TR}}{\mathrm{T1Ref}}}(-1+S)-S+\mathrm{Cos}[\theta]}\right]^2\right)^2\sigma^2_S \tag{C.1}$$

Solving the standard Tofts model differential equation

We start from equation 4.15 and then rewrite:

$$\frac{\delta C_e[t]}{\delta t} = k_{\mathrm{ep}}\left(C_p[t]-C_e[t]\right) \tag{C.2}$$
$$\frac{\delta C_e[t]}{\delta t} + k_{\mathrm{ep}}C_e[t] = k_{\mathrm{ep}}C_p[t] \tag{C.3}$$

Then we create an integrating factor $\sigma[t]$:

$$\sigma[t] = e^{\int k_{\mathrm{ep}}\,dt} \tag{C.4}$$
$$\sigma[t] = e^{k_{\mathrm{ep}}t} \tag{C.5}$$

Multiplying both sides of the equation with the integrating factor and using the product rule for differentiation we get:

$$e^{k_{\mathrm{ep}}t}\frac{\delta C_e[t]}{\delta t} + k_{\mathrm{ep}}e^{k_{\mathrm{ep}}t}C_e[t] = k_{\mathrm{ep}}e^{k_{\mathrm{ep}}t}C_p[t] \tag{C.6}$$
$$\frac{\delta}{\delta t}\left(C_e[t]e^{k_{\mathrm{ep}}t}\right) = k_{\mathrm{ep}}e^{k_{\mathrm{ep}}t}C_p[t] \tag{C.7}$$

Integrating both sides from 0 to a time t using $C_e[0]=0$ and the dummy variable s:

$$C_e[t]e^{k_{\mathrm{ep}}t} = k_{\mathrm{ep}}\int_0^t e^{k_{\mathrm{ep}}s}C_p[s]ds \tag{C.8}$$

This we can rewrite to:

$$C_e[t] = k_{\mathrm{ep}}e^{-k_{\mathrm{ep}}t}\int_0^t e^{k_{\mathrm{ep}}s}C_p[s]ds \tag{C.9}$$
$$C_e[t] = k_{\mathrm{ep}}\int_0^t e^{-k_{\mathrm{ep}}t}e^{k_{\mathrm{ep}}s}C_p[s]ds \tag{C.10}$$
$$C_e[t] = k_{\mathrm{ep}}\int_0^t e^{-k_{\mathrm{ep}}(t-s)}C_p[s]ds \tag{C.11}$$

And then, assuming that $C_e = \frac{C_t}{v_e}$:

$$C_t[t] = K_{\text{Trans}} \int_0^t e^{-k_{\text{ep}}(t-s)} C_p[s] ds \tag{C.12}$$

Which is our final equation

Derivation of the shutter speed model

We start from the modified Bloch equations for magnetization transfer where subscripts e and i stand for EES and intracellular space:

$$\frac{dM_{z_i}}{dt} = \frac{M_{0_i} - M_{z_i}}{T_{1_i}} - R_i M_{z_i} + R_e M_{z_e} \tag{C.13}$$

$$\frac{dM_{z_e}}{dt} = \frac{M_{0_e} - M_{z_e}}{T_{1_e}} + R_i M_{z_i} - R_e M_{z_e} \tag{C.14}$$

R_i	()	Reaction rate constant for exchange from intracellular space to the EES
R_e	()	Reaction rate constant for exchange from EES to the intracellular space

If we solve and sum these equations we get an expression for M_z in case of two site exchange:

$$1 - \frac{M_z}{M_0} = \left(ge^{-ct} + (1-g)e^{ct}\right) e^{-ft} \tag{C.15}$$

$$f = \frac{1}{2}\left(R_{1_i} + R_{1_e} + \frac{1}{\tau_i} + \frac{1}{\tau_e}\right) \tag{C.16}$$

$$g = \frac{1}{2} - \frac{1}{4}\frac{\left((p_e - p_i)\left(R_{1i} - R_{1e}\right) + \frac{1}{\tau_i} + \frac{1}{\tau_e}\right)}{c} \tag{C.17}$$

$$c = \frac{1}{2}\sqrt{\left(R_{1i} - R_{1e} + \frac{1}{\tau_i} - \frac{1}{\tau_e}\right)^2 + 4\frac{1}{\tau_i}\frac{1}{\tau_e}} \tag{C.18}$$

R_{1_i}	(s^{-1})	Relaxation rate in the intracellular space without exchange
R_{1_e}	(s^{-1})	Relaxation rate in the EES without exchange
τ_i	(s)	Average time a water proton stays in the intracellular space
τ_e	(s)	Average time a water proton stays in the EES
p_i	(s)	Population fraction of water in the intracellular space
p_e	(s)	Population fraction of water in the EES

If we then equate equation 4.22 and C.15 we get a relationship for the unknowns:

$$a_S e^{-tR_{1_S}} + a_L e^{-tR_{1_L}} = ge^{-(f+c)t} + (1-g)e^{-(f-c)t}$$

And thus for R_{1_L}, R_{1_S} and a_S:

$$R_{1_L} = \frac{1}{2}\left(R_{1_i} + R_{1_e} + \frac{1}{\tau_i} + \frac{1}{\tau_e}\right) - \frac{1}{2}\sqrt{\left(R_{1_i} - R_{1_e} + \frac{1}{\tau_i} - \frac{1}{\tau_e}\right)^2 + 4\frac{1}{\tau_i}\frac{1}{\tau_e}} \tag{C.19}$$

$$R1_S = \frac{1}{2}\left(R_{1_i} + R_{1_e} + \frac{1}{\tau_i} + \frac{1}{\tau_e}\right) + \frac{1}{2}\sqrt{\left(R_{1_i} - R_{1_e} + \frac{1}{\tau_i} - \frac{1}{\tau_e}\right)^2 + 4\frac{1}{\tau_i}\frac{1}{\tau_e}} \tag{C.20}$$

$$a_S = \frac{1}{2} - \frac{1}{4}\frac{\left((p_e - p_i)\left(R_{1_i} - R_{1_e}\right) + \frac{1}{\tau_i} + \frac{1}{\tau_e}\right)}{\frac{1}{2}\sqrt{\left(R_{1_i} - R_{1_e} + \frac{1}{\tau_i} - \frac{1}{\tau_e}\right)^2 + 4\frac{1}{\tau_i}\frac{1}{\tau_e}}} \tag{C.21}$$

In real clinical situation the concentration is usually to low to really move a_S away from 0, so we can neglect that term. If we then use for R_{1_e} the linear relationship with concentration and use the following equation to reduce the number of unknowns:

$$p_i = (1 - p_e) \tag{C.22}$$

$$\tau_e = \frac{p_e}{p_i}\tau_i \tag{C.23}$$

$$R_{1_e}[0] = (r_1 \mathrm{CR} + R_{1_e}[0]) \text{ and } R_{1_e}[0] = \frac{(R_1[0] - (1 - p_e)\, R_{1_i})}{p_e} \tag{C.24}$$

And this reduces the final equation to, using the substitution $\mathrm{CR} = C_t[t]$:

$$\begin{aligned} R_{1_L} =& \frac{1}{2}\left(C_t[t]r_1 + R_{1_i}[0] + \frac{R_1[0] - (1 - p_e)\, R_{1_i}[0]}{p_e} + \frac{1}{\tau_i} + \frac{1 - p_e}{p_e \tau_i}\right) - \\ & \frac{1}{2}\sqrt{\left(-C_t[t]r_1 + R_{1_i}[0] - \frac{R_1[0] - (1 - p_e)\, R_{1_i}[0]}{p_e} + \frac{1}{\tau_i} - \frac{1 - p_e}{p_e \tau_i}\right)^2 + \frac{4\,(1 - p_e)}{p_e \tau_i^2}} \end{aligned} \tag{C.25}$$

List of Figures

List of Tables